KINEMATIC MODELLING, TRAJECTORY PLANNING, AND MACHINE LEARNING FOR INTEGRATED C-ARM FLUOROSCOPY AND OPERATING TABLE SYSTEMS

FARIA JAHEEN

A thesis submitted to the University of Ottawa in partial fulfillment of the requirements for the Doctorate in Philosophy degree in Electrical Engineering & Computer Science (EECS)

School of Electrical Engineering & Computer Science (EECS)
Faculty of Engineering
University of Ottawa

Table of Contents

List of Tables:

List of Figures:

Legend

A. Acronyms

Acronym	Definition
UI	User Interface
2D / 3D	Two-Dimensional / Three-Dimensional
6D	Six-Dimensional
MIS	Minimally Invasive Surgery
OR	Operating Room
FPD	Flat-Panel Detector
CT	Computed Tomography
CBCT	Cone-Beam Computed Tomography
CTA	Computed Tomography Angiography
DICOM	Digital Imaging and Communications in Medicine
DRR	Digitally Reconstructed Radiograph
AP	Anterior–Posterior (Clinical imaging projection)
LAT	Lateral (Clinical imaging projection)
PA	Posterior–Anterior (Clinical imaging projection)
V1	Vascular 1 (Clinical imaging projection)
V2	Vascular 2 (Clinical imaging projection)
VER	Vertebroplasty (Clinical imaging projection)
C-Arm	Mobile or stationary X-ray imaging device with C-shaped gantry
EVAR	Endovascular Aneurysm Repair
DoF	Degrees of Freedom
D-H	Denavit–Hartenberg (kinematic parameterization)
FK	Forward Kinematics
IK	Inverse Kinematics
L-BFGS	Limited-memory Broyden–Fletcher–Goldfarb–Shanno (IK optimization method)
LUT	Lookup Table
AI	Artificial Intelligence
ML	Machine Learning
DNN	Deep Neural Network
MLP	Multilayer Perceptron

GBM	Gradient Boosting Machine
RF	Random Forest
KNN	K-nearest Neighbors
MAE	Mean Absolute Error
MSE	Mean Squared Error
RMSE	Root Mean Squared Error
SIFT	Scale-Invariant Feature Transform

B. Nomenclature of Symbols

Symbol	Definition
x, y, z	Cartesian translational coordinates of the end-effector
$R\ (\varphi, \theta, \psi)$	Rotation matrix defined by roll (φ), pitch (θ), and yaw (ψ)
T	Homogeneous transformation matrix (4×4) describing rigid-body motion
$\|\|.\|\|$	Euclidean norm
$\Delta \boldsymbol{x}$	Pose error vector between desired and measured end-effector positions
$\boldsymbol{q}$	Vector of joint variables (prismatic displacements or revolute angles)
$\dot{\boldsymbol{q}}$	Joint velocity vectors
$\ddot{\boldsymbol{q}}$	Joint acceleration vectors
τ	Vector of joint torques or actuator forces
$\boldsymbol{\omega}$	Angular velocity vector of the end-effector
$\boldsymbol{\xi}$	Twist vector combining linear and angular velocity

Abstract

This dissertation presents a unified methodological framework that synergistically integrates kinematic analysis, trajectory planning, and machine learning-enabled kinematic solvers to advance modular C-arm fluoroscopy systems coupled with multi-degree-of-freedom (DoF) operating tables. Conventional C-arm devices, though indispensable for intraoperative visualization, remain hampered by constrained maneuverability, operator-dependent variability, and radiation inefficiencies limitations exacerbated in minimally invasive surgery (MIS), where procedural precision and radiation stewardship are cardinal. To redress these deficiencies, the research unfolds in three interlinked contributions. First, rigorous forward and inverse kinematic formulations, augmented by voxelized collision-aware workspace mapping, are deployed across 6-DoF to 9-DoF C-arm with operating table configurations to quantify anatomical accessibility and collision-free pose feasibility across six clinically relevant projections. Second, multiple trajectory planning paradigms including polynomial interpolation, trapezoidal velocity profiles, and biologically inspired minimum-jerk and minimum-snap strategies are comparatively analyzed to ensure smooth, dynamically admissible, and singularity-robust transitions between imaging poses. To operationalize these strategies intraoperatively, lookup tables (LUTs) derived from precomputed trajectories and singularity analyses are introduced as pragmatic decision-support tools, enabling rapid recall of optimized motion plans tailored to patient-specific anatomy. Third, machine learning (ML) frameworks are harnessed to overcome the computational intractability of traditional numerical solvers for high-DoF systems. Leveraging expansive simulation-derived datasets, five supervised models including deep neural networks are trained and validated, achieving sub-millimetric positional accuracy and sub-degree angular precision while delivering real-time inference that surpasses conventional methods in scalability, robustness, and computational latency. Collectively, these contributions delineate a clinically translatable paradigm that unifies kinematic modelling, trajectory optimization, and ML-based inference, establishing the foundation for intelligent, precision-driven, and radiation-conscious intraoperative imaging within next-generation hybrid operating rooms.

Acknowledgements

This dissertation represents the culmination of several years of research, perseverance, and personal growth, and it would not have been possible without the guidance, encouragement, and support of many individuals and institutions.

First and foremost, I would like to express my deepest gratitude to my supervisor, **Prof. Pascal Fallavollita**, for his invaluable mentorship, steadfast support, and intellectual guidance throughout the course of my doctoral studies. His insights, constructive feedback, and ability to challenge my ideas with rigor have been instrumental in shaping this work.

I would also like to sincerely thank Prof. Sergio Ledesma, whose instruction in artificial intelligence from the very foundations provided me with the knowledge and confidence to pursue advanced work in machine learning.

I am grateful to the members of my thesis committee for their time, thoughtful critiques, and contributions that have strengthened this dissertation. I also acknowledge the contributions of my peers and collaborators in the Metrics Lab, whose camaraderie and shared expertise created a stimulating environment for research and discovery. Special thank goes to Vinod Gutta for his collaboration and insightful discussions.

I am also grateful to the administrative and technical staff at the University of Ottawa for their assistance in facilitating research resources and laboratory IT support.

I wish to thank my family for their adoration and trust.

Finally, I dedicate this dissertation to my late father whose unwavering belief in education and vision for my academic journey inspired me to pursue a doctoral degree, and to my mother whose resilience and persistent encouragement instilled in me the perseverance needed to equip this journey.

Author Contributions

Open Source

1. C-arm and operating table combined setup with higher degrees of freedom . Designed for numerical analysis. Link here.
2. Modular C-arm Trajectory Planning & Computed Torque Control. Link here.
3. Collision-free pose datasets for a modular 9-DoF C-arm system combining an enhanced 6-DoF OEC Elite and a 3-DoF STERIS CMAX surgical table. Designed for ML-based kinematics modelling. Link here.

Publications

1. Jaheen, Faria, Vinod Gutta, and Pascal Fallavollita. "C-Arm and Patient Table Integrated Kinematics and Surgical Workspace Analysis," in *IEEE Access*, vol. 13, pp. 180276-180290, 2025, doi: 10.1109/ACCESS.2025.3615843.
2. Jaheen, Faria, Vinod Gutta, and Pascal Fallavollita. "Trajectory Planning for Multiple Degrees of Freedom C-Arm Systems," in *IEEE Access*, vol. 13, pp. 181396-181415, 2025, doi: 10.1109/ACCESS.2025.3623567.
3. Jaheen, Faria, Vinod Gutta, and Pascal Fallavollita. “Modelling C-arm fluoroscopy and Operating table Kinematics via Machine Learning” in Front. Robot. AI. **Accepted:** 10 Nov 2025.

Chapter 1 : Foundations and Research Framework for Intelligent and modular C-arm and Operating Table Positioning

1.1 Synopsis of Thesis

Minimally invasive surgery (MIS) has significantly improved patient outcomes by reducing complication rates and hospital stays. Among the imaging technologies that support these procedures, X-ray-based C-arm fluoroscopy systems are widely adopted for their real-time, high- resolution imaging capabilities [1]. These systems facilitate intraoperative visualization of complex anatomical structures by enabling dynamic radiographic imaging from multiple angles. The C-arm consists of a C-shaped arm that houses the X-ray source and detector and is capable of rotating around the patient. When combined with a mobile operating table, these systems provide greater flexibility in pose alignment for target anatomy acquisition during image-guided procedures.

Despite their clinical value, conventional C-arm systems often suffer from limited maneuverability due to a restricted number of degrees of freedom (DoF), which constrains their operational workspace and imaging flexibility. Moreover, during a single procedure, the C-arm must often be repositioned multiple times to achieve the optimal imaging angle, requiring additional X-ray acquisitions. This leads to prolonged surgical durations and elevated radiation exposure for both the patient and the surgical team [1-3]. The problem becomes more pronounced when integrated with operating tables, whose movement capabilities introduce coupled kinematic dependencies. Thus, positioning accuracy and efficiency become critical factors influencing procedural success.

To overcome these limitations, there is a pressing need to model and extend the surgical workspace (i.e. the set of all feasible poses (positions and orientations) for X-ray imaging) by incorporating both the C-arm and operating table kinematics. Physical constraints such as joint limits, operating room layout, and the presence of the patient restrict this workspace. A comprehensive analysis of the combined workspace can provide clinicians with enhanced pre-operative planning tools, reduce intraoperative adjustments, and improve targeting of anatomical regions. Furthermore, enabling real-time positioning within this workspace requires a combination of forward kinematics (FK) and inverse kinematics (IK) models, optimized for high-DoF systems.

1.2 Evolution and Role of Medical Imaging in Minimally Invasive Surgery

Image-guided interventional procedures have fundamentally transformed surgical practice by enabling clinicians to operate with enhanced precision through indirect visualization. Rather than relying solely on

direct line-of-sight exposure of anatomical structures, modern interventions leverage preoperative and intraoperative imaging modalities to navigate complex internal anatomies. This paradigm shift has significantly reduced the invasiveness of procedures, thereby diminishing infection risk, preserving delicate tissues, and ultimately improving patient outcomes while curbing healthcare expenditures [4-5].

Since the introduction of X-ray imaging, the field of medical imaging has undergone tremendous technological evolution, culminating in a broad array of modalities tailored to specific clinical needs. These include computed tomography (CT), magnetic resonance imaging (MRI), ultrasound, and more recently, molecular imaging techniques that facilitate visualization at the cellular and metabolic levels [6-7]. Collectively, these modalities enable the execution of procedures with heightened accuracy and safety.

For example, in the context of orthopedic and trauma surgery, where precision in instrument placement and anatomical alignment is paramount, medical imaging serves not only as a diagnostic tool but also as an intraoperative guide. Surgeons benefit from real-time feedback through tracked instruments and dynamic anatomical visualization, often enhanced through image fusion techniques that overlay multimodal data [8-9]. Such capabilities extend the visual perception of the clinician beyond the physical constraints of the surgical field, enabling minimally invasive access to critical anatomical targets.

Comprehensive reviews by Wolbarst and Hendee [7], along with others [10]–[13], have outlined the physical principles, technological advancements, and clinical applications of contemporary imaging systems. These insights underscore the pivotal role of image-guided systems in the transition from traditional open surgeries to minimally invasive and robot-assisted procedures. The integration of imaging with intelligent surgical planning and navigation frameworks forms the backbone of next-generation interventional systems; an integration this thesis seeks to advance through intelligent C-arm and operating table coordination.

1.3 Principles and Clinical Role of X-ray Imaging

X-ray imaging remains one of the most pervasive and indispensable modalities in image-guided surgery (IGS) due to its capacity for real-time visualization and its superior contrast for bony structures. The fundamental principle underpinning X-ray imaging is the measurement of photon attenuation as X-rays traverse anatomical regions of varying densities. Because osseous structures attenuate X-rays significantly more than surrounding soft tissues, X-ray imaging is especially effective for skeletal visualization and guidance during orthopedic, trauma, and endovascular procedures [14]. Figure 1.1 illustrates representative projection radiographs alongside anatomical renderings, underscoring the inherent clinical trade-off while X-rays provide exceptional delineation of bony structures, their capacity to resolve soft tissues is limited.

This fundamental constraint motivates the complementary use of advanced modalities such as CT and cone-beam CT for volumetric anatomical assessment.

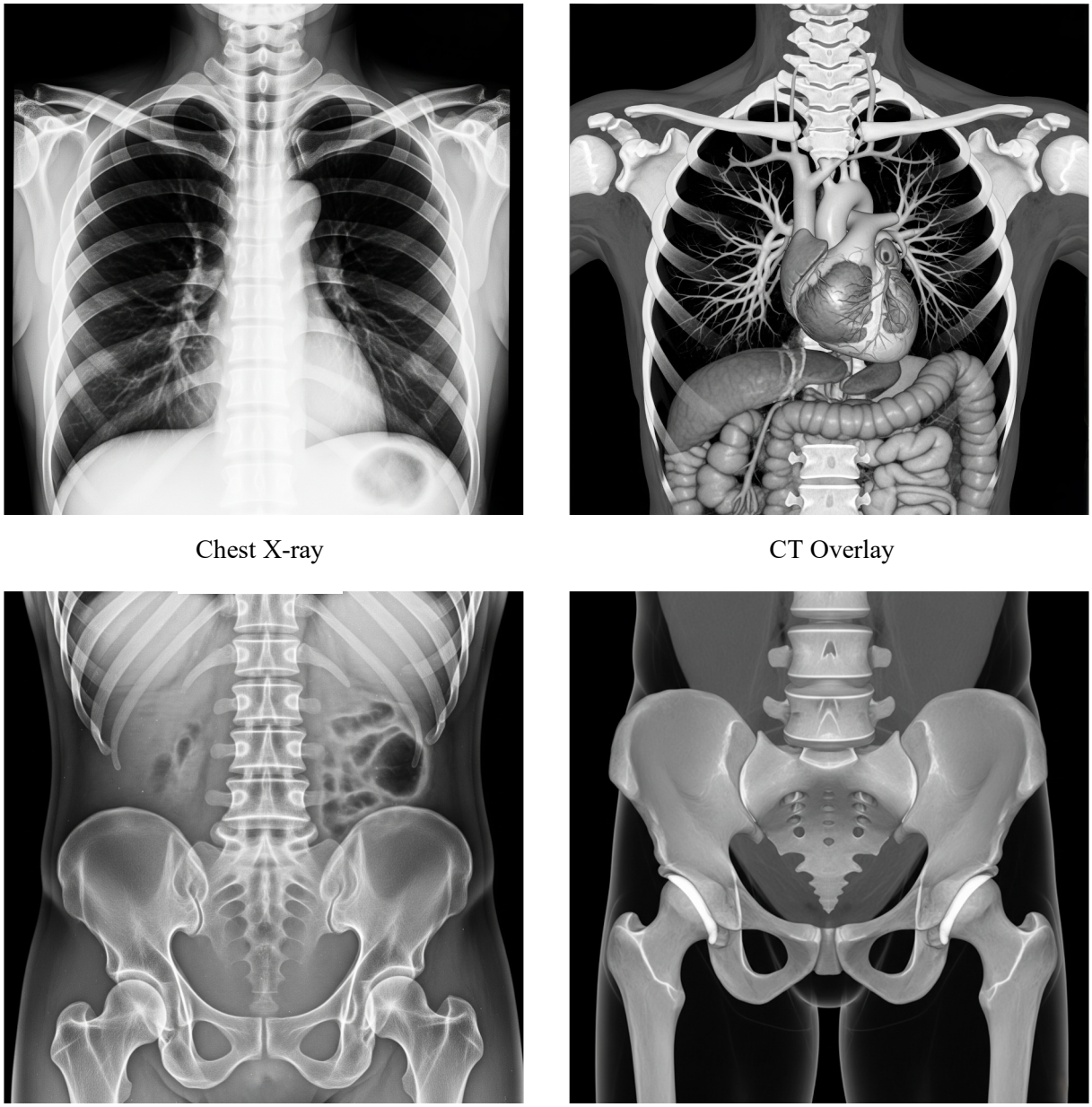

Figure 1.1: Comparative illustration of projection radiographs (left panels) and anatomical renderings (right panels). While X-ray imaging excels in visualizing osseous structures, its restricted soft-tissue contrast necessitates complementary modalities such as CT for volumetric anatomical guidance in surgical contexts.

X-ray imaging systems are generally categorized into two main classes: (i) projection-based methods such as conventional radiography and fluoroscopy, and (ii) tomographic methods such as computed tomography (CT) [14]. Fluoroscopy, often facilitated via C-arm configurations, enables dynamic intraoperative imaging and is thus central to minimally invasive workflows. However, a principal drawback of X-ray modalities is the use of ionizing radiation, which if not properly mitigated has been associated with elevated risks of malignancy [15, 16] and heritable genetic damage [17].

C-arm fluoroscopic systems serve as the standard apparatus for intraoperative X-ray projection. These devices consist of an X-ray tube and a flat-panel detector mounted on opposing ends of a C-shaped gantry, enabling rotational imaging around the patient. C-arms are broadly classified into stationary systems, primarily employed for vascular interventions, and mobile systems, favored in orthopedic and trauma surgeries due to their portability and real-time imaging capabilities [14].

Despite their utility, mobile C-arms face notable limitations. Geometric distortions often arise due to gantry flexion and detector curvature, affecting image fidelity. Furthermore, traditional C-arm fluoroscopy inherently yields 2D projections of 3D anatomy, resulting in a loss of depth information along the beam path. Advances such as cone-beam computed tomography (CBCT) now permit 3D reconstructions from multiple 2D views, enabling more accurate intraoperative visualization. Comparative studies have assessed the efficacy of 3D C-arm systems, such as the Siemens Iso-C 3D and Ziehm Vario 3D, for orthopedic procedures [18]. The clinical utility of 3D imaging in fracture reconstruction and implant placement has also been demonstrated in [19], [20].

By contrast, conventional CT scanners employ a rotating X-ray source and detector array to generate high-resolution volumetric reconstructions. Although CT provides exceptional geometric accuracy [21], it is susceptible to metal-induced artifacts and necessitates higher radiation doses. Mitigation strategies have included the use of high-energy beams [22] and interpolation-based correction algorithms [23-27]. In the case of cone-beam CT, tracking the metal object's position has also been explored as a correction strategy [28].

However, due to cost, bulk, and radiation concerns, CT imaging is typically restricted to preoperative diagnostics and planning, rather than real-time intraoperative guidance.

1.4 Systemic Challenges in Intraoperative C-arm Repositioning

C-arm positioning during intraoperative imaging presents a multitude of pragmatic challenges for interventionalists. These operational hurdles have been corroborated through extensive consultation with clinical collaborators and include the following:

Miscommunication: In the typical operating room (OR) workflow, interventionalists do not directly control the C-arm fluoroscope but instead relay positioning instructions to a nurse or radiologic technician. This indirect mode of operation introduces a high potential for misinterpretation, whereby the conveyed C-arm configuration may be inaccurately executed, leading to suboptimal imaging angles and procedural inefficiencies.

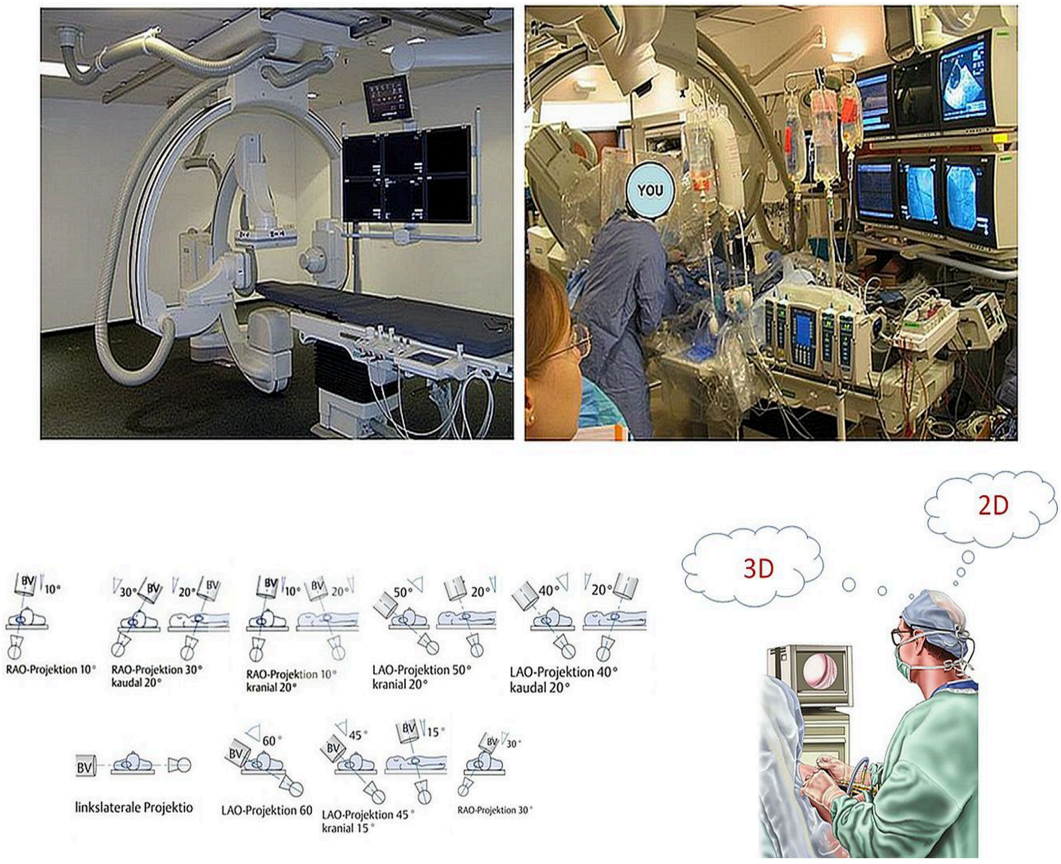

Figure 1.2: (Top) Intraoperative complexity within interventional suites, highlighting the spatial and operational constraints encountered during procedures. (Bottom) The nine canonical 'textbook' C-arm

positions frequently referenced by interventionalists, illustrating the cognitive burden associated with mentally reconstructing 3D anatomy from 2D fluoroscopic images.

Unattainability: Although the theoretical kinematic model of modern C-arm systems suggests near-continuous maneuverability relative to the operating table, real-world constraints frequently render certain desired poses inaccessible. This can be attributed to accumulated mechanical offsets, initial configuration limitations, or physical barriers within the OR. Consequently, realizing a target view often necessitates full reconfiguration of multiple C-arm axes, a process that is both time-intensive and disruptive to surgical flow (see Figure 1.2).

Complex User Interfaces: Contemporary angiographic C-arm systems are still equipped with antiquated user interface (UI) modalities, such as joysticks, rotary dials, and keypads populated with a profusion of buttons. These controls govern critical imaging parameters including angulation, focal length, kilovoltage, and current intensity. However, such interfaces are neither intuitive nor conducive to specifying high-level clinical imaging intents such as the interventionalist's mental conception of a 'Desired-view.' The lack of semantic mapping between UI controls and clinical objectives hinders efficient navigation and increases cognitive workload during surgery.

Collectively, these challenges underscore the necessity for an intelligent, user-centric interface paradigm that empowers interventionalists to define target views directly thus enabling the system to autonomously compute the requisite C-arm and operating table kinematics.

1.5 Limitations of Conventional Systems

Over the past three decades, various strategies have been introduced to enhance the positioning capabilities of C-arm systems. Early innovations included camera-augmented mobile C-arm platforms (CamC) that used visual servo to estimate pose via external calibration setups [31], [33], and optical tracking-based navigation systems requiring additional hardware installations in the operating room [30]. Although these methods improved accuracy, they introduced complexity and required non-integrated infrastructure. Further advances involved robotic C-arms with closed-form IK for positioning automation, though these solutions were generally constrained to 5 or 6 DoF systems [32], [47].

While some recent studies have explored machine learning (ML) for motion estimation, including convolutional neural networks for 5-DoF positioning tasks [48-50], many of these efforts remain limited in scope and scale. Notably, they focus primarily on the C-arm itself without comprehensive consideration of the operating table. Moreover, most do not incorporate full surgical workspace analysis or account for clinical constraints such as patient safety zones, tool clearances, or collision detection. The absence of scalable, unified models that handle the full C-arm and operating table integrated system with more than 5 or 6 DoF represents a significant gap in current literature.

Additionally, motion planning strategies particularly those used in surgical robotics have largely been optimized for manipulators and wearable devices [51]–[58]. These include joint space trajectory planners designed to handle redundancy and avoid singularities. However, such methods are seldom applied to imaging systems like C-arms, which require ultra-smooth trajectories in tightly constrained environments. In high-DoF systems, classical kinematic solvers [59] often fail to converge efficiently or generalize poorly due to nonlinear coupling and dynamic constraints.

1.6 Limitations in User Interfaces and Motivation for 'Desired views' Paradigm

Fong et al. introduced a comprehensive treatise entitled *Imaging and Visualization in the Modern Operating Room: A Comprehensive Guide for Physicians* [29], in which they critically examine the evolution of user interfaces within the surgical environment. One of the most salient innovations highlighted is gesture-based control; however, its practical viability in intraoperative scenarios remains largely unsubstantiated. More importantly, even with gesture control, interventionalists are still compelled to physically reposition the imaging apparatus, often with no guarantee of achieving the optimal anatomical view.

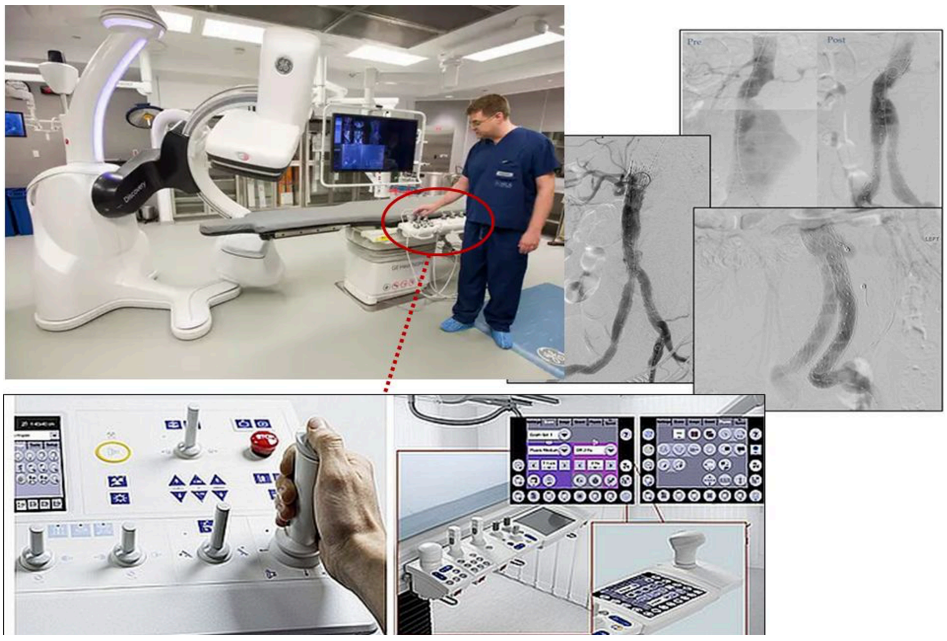

Figure 1.3: (Top) The GE Discovery suite located in the Division of Vascular Surgery at The Ottawa Hospital, routinely used for endovascular procedures such as EVAR. (Bottom) Conventional user interfaces employed to control C-arm fluoroscopy systems; the control workflow is often cumbersome requiring manual adjustment of numerous parameters.

Despite advancements in digital health technologies, joysticks and hardware-based toggles remain prevalent in operating rooms, largely due to the ergonomic inefficacy of mouse-based control systems. Figure 1.3 illustrates a prototypical UI used for C-arm manipulation designs that, in many respects are derived from the user interface paradigms of the 1980s. Fong et al. prognosticate that future surgical UIs will amalgamate gestural, tactile, visual, and speech-based modalities. Crucially, they assert that next-generation interfaces must extend mere responsiveness and incorporate anticipatory intelligence capable of forecasting procedural workflows.

Figure 1.4: Non-robotic, manually operated C-arm fluoroscopy system in a resource-limited hospital setting. Both the C-arm and the operating table are positioned manually by staff, highlighting the operational challenges addressed by the proposed intelligent 'Desired-views' paradigm.

A critical reality particularly in low-to-middle-income countries (LMICs) and underfunded healthcare systems is that many operating rooms are equipped with non-robotic C-arm fluoroscopy systems (Figure 1.4). In these setups, both the C-arm and the operating table must be positioned manually by technologists or nursing staff under verbal guidance from the interventionalist. This manual approach introduces several inefficiencies, including prolonged setup time, increased communication errors, and limited reproducibility of precise imaging angles. The absence of automated kinematic assistance further compounds procedural delays and may elevate radiation exposure due to repeated imaging.

Addressing this technological disparity is central to the motivation of this thesis. The proposed retrofit-capable intelligent positioning framework is designed to function in both ends of the technological spectrum serving as a fully autonomous control layer for robotic systems while also guiding manual operators in real time through visual or auditory prompts. A desired-view user interface signifies that interventionalists no longer directly manipulate the device. Instead, they articulate the requisite intraoperative imaging views specific to the patient's anatomy and the surgical objectives. The user interface capable of intelligent planning algorithms, autonomously computes the requisite kinematic transformations spanning both the C-arm and the operating table required to realize the 'Desired-views.' These views are then correlated with the physical system via the manufacturer's computational infrastructure.

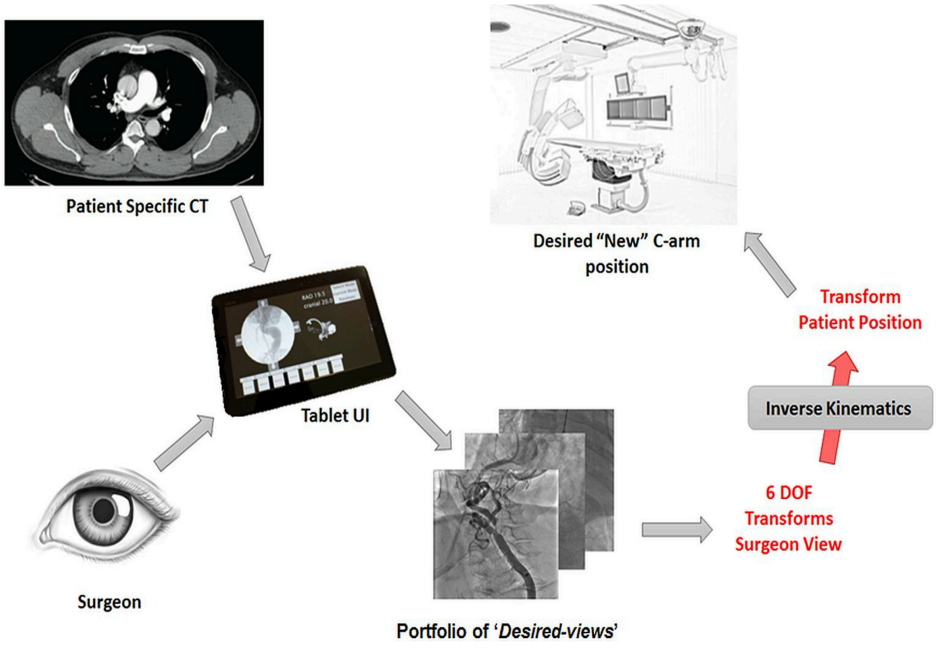

Figure 1.5: Loading the patient-specific CTA data prior to interventional angiography surgery, the interventionist will use the 'Desired-views' UI to create a portfolio of desired views UI to create a portfolio of desired-views. Each desired-view has the associated C-arm gantry positions. The picture shows an example for 5DoF when moving the C-arm device only.

A subsidiary advantage of this approach is its facilitation of offline preoperative interaction, enabling clinicians to engage with the interface during planning sessions (e.g., in a pre-surgical conference or

informal review). Desired anatomical views can be defined on patient-specific datasets in advance, significantly reducing intraoperative guesswork and exposure to ionizing radiation.

Computed Tomography Angiography (CTA) serves as a critical modality for both diagnostic assessment and surgical planning in interventional angiography surgery. While contrast agents are used during imaging to enhance vessel visibility, intraoperative usage of CTA is constrained by spatial limitations, particularly as patients are situated within confined imaging systems. Nevertheless, CTA confers the advantage of yielding volumetric 3D reconstructions, in contrast to conventional C-arm fluoroscopy, which is inherently two-dimensional. As such, CTA is extensively leveraged in preoperative planning, but its real-time integration with C-arm positioning remains underdeveloped. The 'Desired-views' concept aims to bridge this gap by synergizing CTA-derived views with real-time, intelligent C-arm trajectory planning (Figure 1.5).

1.7 Literature and Intellectual Property Landscape

Many techniques have been developed to support, but not directly obtain, the acquisition of the optimal interventionalist viewpoint (i.e. Desired-views), e.g. optical tracking based navigation systems [30], visual servoing based C-arm positioning [31], robotized C-arm systems [32], artificial fluoroscopy [33], the inverse C-arm positioning using real-time body part detection [34], intensity-based registration [35], and radiographic fiducials [36-37]. Further, there is substantial interaction to acquire and subsequently browse and manipulate images when C-arm devices are positioned. Several authors have pointed out restrictions this imposes [38-39]. Graetzel et al. [38] describes a 7-minute communication as the interventionalist instructs the assistant to click on the exact and appropriate place of the C-arm interface. While this is an extreme example, it illustrates the potential communication difficulties associated with image manipulation by proxy, when the proxy does not share the same level of visual expertise. Wachs et al. [39] discuss that the requirement to interact with touch-based technology means that interventionalists are required to move away from the patient to where the technology is located to browse or manipulate images. In response to these limitations, researchers have developed new experimental systems, such as Gestix, where interaction with images in surgical settings is achieved through gesture recognition techniques based on camera input [40]. At the same time, new technologies such as Kinect signals a new enthusiasm for expanding the ways in which gestural input might be used [41].

Although touchless interaction modalities for the operating room have been investigated extensively, clinical uptake has been modest. Empirical reports point to recurring impediments: ambiguous authority during control delegation (surgeon vs. technologist), variable user engagement over long cases, insufficient granularity for fine manipulations, ergonomic and line-of-sight constraints in cluttered suites, and limited

multiuser collaboration without contention for control [42]. Collectively, these factors inhibit reliability and workflow trust, which are prerequisites for adoption in safety-critical settings.

A frequently cited alternative is the centroid-based planning method described in the patent literature [43]. In brief, the approach (i) defines a reference plane in preoperative CTA intersecting the anatomy of interest, (ii) assumes an available segmentation of the anatomy (manual or automated), (iii) selects the centroid (X,Y,Z) of that segmentation on the plane, (iv) computes the plane's normal and a tangential basis, and (v) prescribes C-arm orientation by aligning the source–target vector with the normal (operationalized via a positive dot product with the focal-length vector). The procedure is algorithmically parsimonious and, under idealized conditions, yields a reproducible viewing angle.

Notwithstanding its elegance, the method exhibits material limitations relative to the proposed Desired-views paradigm:

- Target specificity: Clinical "optimal views" are rarely centroid-seeking. They depend on lesion morphology, device landing zones, vascular tortuosity, and subsegmental landmarks, rendering a centroid proxy too coarse for many interventions.
- Model rigidity: A fixed alignment rule cannot accommodate multi-objective trade-offs (e.g., avoiding collisions, honoring table/patient constraints, minimizing dose, preserving tool clearance) that routinely govern intraoperative decision-making.
- Data dependencies and brittleness: The pipeline presumes accurate, stable segmentation and static preoperative geometry; yet intraoperative motion, deformation, and table repositioning perturb the anatomy–device relationship, degrading view optimality.
- Kinematic incompleteness: The formulation prescribes an angle but does not solve the full kinematic realization (coupled C-arm and operating table DoFs) or guarantee path feasibility between poses.
- Lack of interactivity and uncertainty handling: The approach affords no interactive exploration of alternatives, what-if analyses, or uncertainty quantification to guide operator confidence when data are noisy or ambiguous.

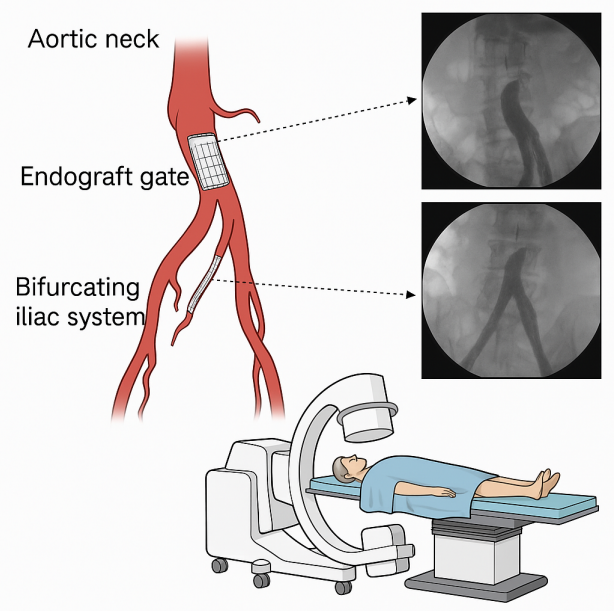

Figure 1.6: Schematic representation of Endovascular Aneurysm Repair (EVAR) highlighting the three primary anatomical targets—(1) aortic neck, (2) endograft gate, and (3) bifurcating iliac system—and the proposed 'Desired-views' workflow for automated C-arm and operating table positioning.

By contrast, the proposed Desired-views framework enables direct specification of clinically meaningful views (multiple targets, constraints, and priorities), performs joint optimization over C-arm and operating table kinematics with explicit collision models, adapts to intraoperative updates via registration, and provides an interactive UI for rapid exploration and operator oversight. This combination addresses the practical determinants of adoption fidelity, flexibility, and explainability that are indispensable for routine use in the operating room. To anchor the above critique and proposed approach in a representative clinical scenario, Figure 1.6 illustrates the schematic representation of Endovascular Aneurysm Repair (EVAR), highlighting three primary targets. These targets are mapped to the 'Desired-views' workflow, which enables automated, constraint-aware C-arm and operating table positioning. This example illustrates why target-centric, multi- objective planning is required beyond centroid alignment.

1.8 Problem Statement

The central objective of this thesis is to develop and validate a unified framework for intelligent motion modelling, trajectory planning, and kinematic control of modular C-arm fluoroscopy systems integrated with operating tables. The research aspires to directly confront and ameliorate the principal limitations delineated in Sections 1.4 and 1.5 through three pivotal contributions:

1. Modelling and analyzing the collision-free surgical workspace for multi-DoF C-arm and table systems across clinically relevant imaging views.

2. Developing joint space trajectory planning techniques optimized for high-DoF systems, considering clinical constraints and patient-specific characteristics.
3. Implementing and evaluating machine learning-based forward and inverse kinematic models to replace classical symbolic solvers, enabling real-time prediction and generalization across configurations.

These objectives collectively address the limitations of conventional systems and pave the way for fully integrated, intelligent intraoperative imaging solutions facilitating the 'Desired-views' of interventionalists and surgeons.

1.9 Overview of Thesis Objectives

The aim of this dissertation is to conceptualize, implement, and clinically contextualize a unified framework for intelligent motion modelling and automated positioning of modular C-arm fluoroscopy systems when integrated with multi-DoF operating tables. To achieve this vision, the research is structured around three interdependent objectives:

Objective 1: Modelling and Expansion of the Surgical Workspace

The first objective is to construct comprehensive forward and inverse kinematic models of modular C-arm and operating table systems and to generate large-scale, collision-free datasets encompassing clinically relevant imaging poses. The objective endeavours to rigorously quantify how incremental degrees of freedom expand anatomical reachability, enhance accessibility to surgical targets, and improve volumetric coverage within the constrained operative milieu.

Objective 2: Design and Optimization of Trajectory Planning Paradigms

The second objective is to devise and evaluate trajectory planning methodologies that yield smooth, dynamically feasible, and collision-free transitions between predefined clinical imaging poses. Emphasis will particularly be placed on embedding patient-specific anatomical and procedural constraints, mitigating singularity-induced discontinuities, and optimizing spatiotemporal efficiency. To foster clinical translatability, the proposed trajectories will be operationalized into lookup tables (LUTs) that equip interventionalists with rapid, procedure- tailored recommendations for trajectory profiles and joint parameterization, thereby bridging the gap between algorithmic rigor and pragmatic utility.

Objective 3: Machine Learning–Enabled Kinematic Solvers

The third objective is to design, train, and validate machine learning frameworks for solving forward and inverse kinematics that can generate real-time, clinically admissible predictions of joint configurations and end-effector poses. These models aspire to surpass conventional analytical and numerical solvers in both generalization across diverse system configurations and computational efficiency, thus enabling seamless deployment within high-dimensional intraoperative workspaces without latency bottlenecks.

Collectively, these objectives address the fundamental limitations of existing C-arm positioning systems by integrating principled kinematic modelling, trajectory optimization, and data-driven inference. They establish the theoretical and methodological foundation upon which the subsequent research hypotheses (Section 1.11) will be formulated and empirically tested. Importantly, the framework is envisioned to be adaptable not only for advanced robotic C-arm platforms but also for manually operated systems prevalent in low-to-middle-income countries (LMICs) and underfunded healthcare settings, thereby ensuring both technological innovation and global clinical relevance. For enhanced clarity and rapid apprehension, the research objectives are succinctly encapsulated in Table 1.

Table 1.1: Synoptic articulation of the thesis objectives underpinning the development of intelligent modular C-arm systems.

Objective	Expected Outcome	Clinical Value
Modelling and Expansion of the Surgical Workspace	Development of forward and inverse kinematic models; generation of large-scale collision-free datasets mapping feasible poses across imaging projections.	Expanded anatomical reachability and improved access to critical surgical targets within constrained operative environments.
Design and Optimization of Trajectory Planning Paradigms	Implementation of smooth, dynamically feasible, collision-free trajectories between clinical imaging poses; operationalization into lookup tables for rapid clinical use.	Reduced intraoperative setup time, mitigation of singularities, optimized motion efficiency, and provision of procedure-tailored decision support to interventionalists.
Machine Learning–Enabled Kinematic Solvers	Creation and validation of ML-based forward and inverse kinematic models capable of real-time inference with clinically admissible accuracy.	Elimination of computational bottlenecks, enhanced adaptability across diverse system configurations, and reliable intraoperative deployment in high-DoF workspaces.

1.10 Overview of Thesis Hypotheses

This dissertation advances three hypotheses that together interrogate how added kinematic redundancy, principled trajectory synthesis, and data-driven solvers can yield clinically actionable C-arm positioning in heterogeneous operating environments.

Research Hypothesis 1: Surgical Workspace Augmentation via Additional Degrees of Freedom

We hypothesize that augmenting conventional C-arm architectures with supplementary, integrated degrees of freedom particularly through the incorporation of multi-DoF operating tables will markedly amplify the collision-free surgical workspace. This expansion is anticipated to enhance anatomical reachability and facilitate access to clinically critical poses across a spectrum of imaging projections, thereby broadening intraoperative versatility.

Research Hypothesis 2: Clinically Feasible Trajectory Optimization Between Imaging Poses

We hypothesize that it is clinically tenable to engineer a trajectory planning paradigm capable of producing smooth, dynamically feasible, and collision-free kinematic transitions between pre- specified clinical imaging poses. This paradigm will embed patient-specific anatomical and procedural constraints, optimizing both spatiotemporal motion efficiency and operative safety, thus enabling reproducible and reliable intraoperative navigation across targeted anatomical landmarks. Furthermore, we posit that the implementation of lookup tables derived from precomputed trajectory simulations and singularity analyses can serve as a pragmatic decision- support tool. Such LUTs will allow interventionalists to rapidly select optimal trajectory profiles and joint parameter settings for diverse patient anatomies and procedural contexts. By operationalizing the framework through LUTs, the hypothesis extends beyond theoretical feasibility to practical clinical applicability, ensuring that trajectory planning can be seamlessly integrated into routine intraoperative workflows.

Research Hypothesis 3: Machine Learning–Driven Forward and Inverse Kinematics

We hypothesize that data-driven machine learning frameworks for resolving forward and inverse kinematics can attain positional and angular accuracies within clinically admissible thresholds, matching or surpassing those of conventional numerical solvers. Furthermore, such models are expected to preserve performance fidelity across expanded workspaces while enabling real-time inference and cross-configuration generalization, thereby obviating the computational latency inherent to traditional algorithmic approaches.

The interrelationship between the defined research objectives, their associated hypotheses, and the methodological strategies is illustrated in Figure 1.7, providing a consolidated overview of the dissertation's conceptual framework.

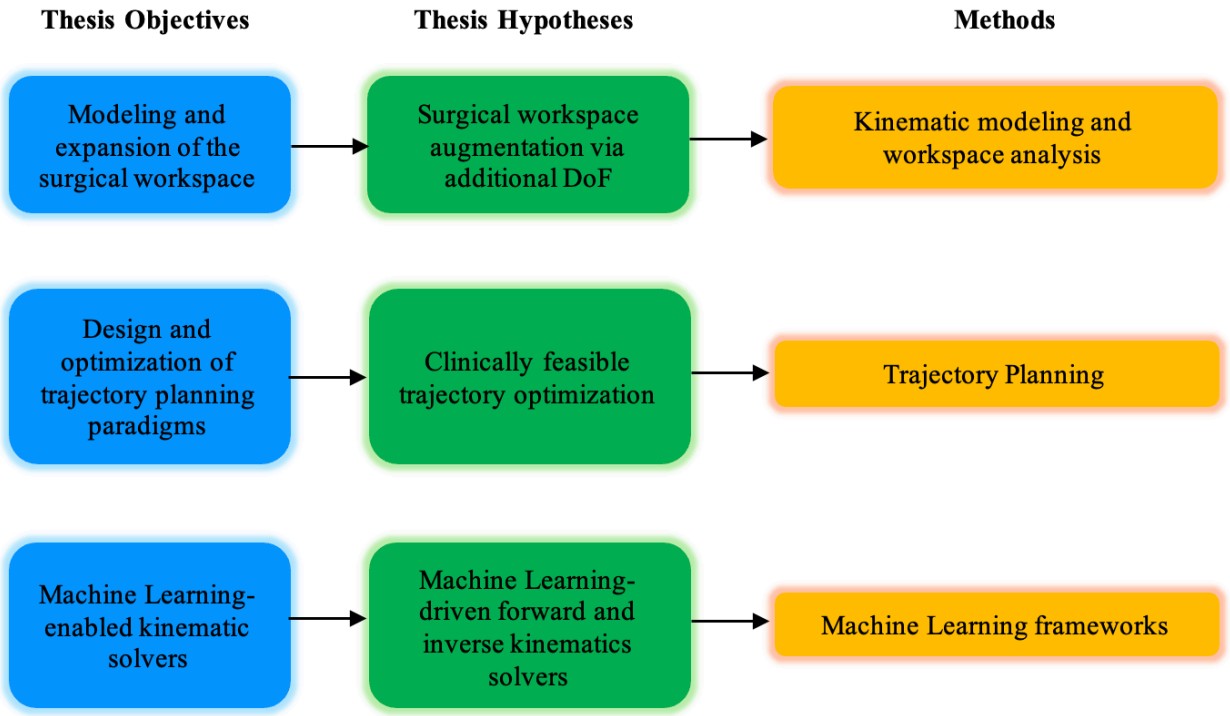

Figure 1.7: Conceptual schematic linking research objectives, hypotheses, and methodological framework.

1.11 Workflow Overview

Figure 1.8 illustrates the methodological framework unifying the three contributions. Contribution 1 establishes the foundational collision-free workspace and data. Contribution 2 builds on this by designing kinematic and trajectory optimization strategies while Contribution 3 leverages the data and planning pipeline to train ML models capable of performing FK and IK in real-time clinical scenarios. This figure highlights how each study builds upon the previous one to form a unified framework for intelligent and safe intraoperative motion planning.

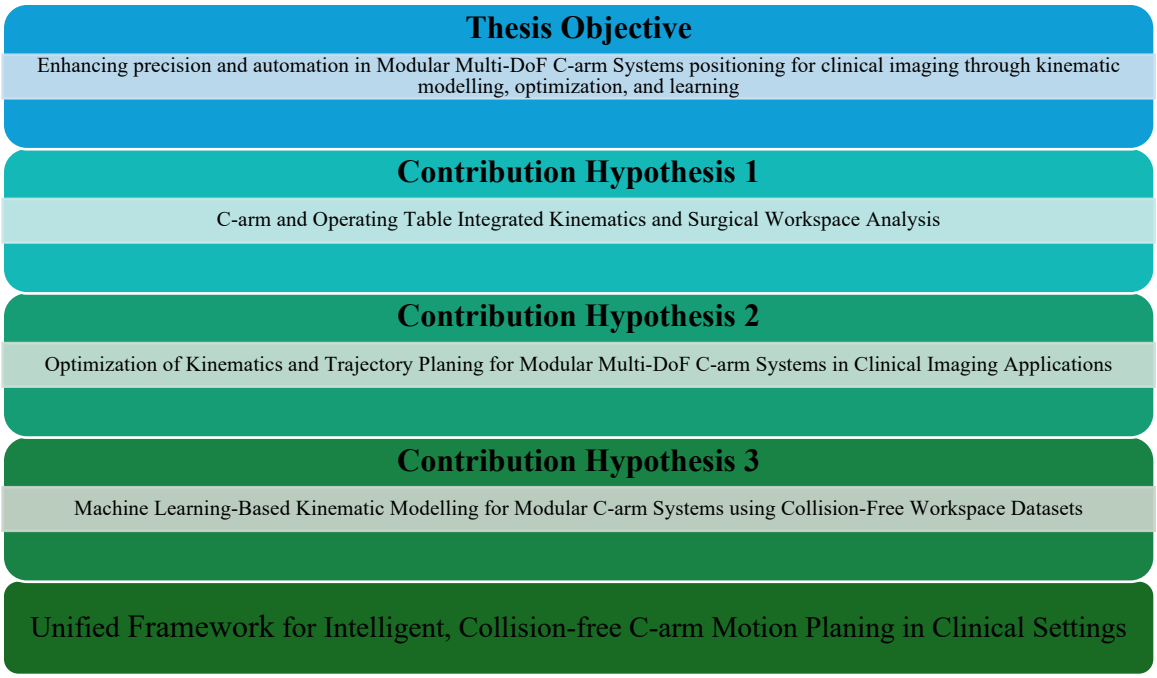

Figure 1.8: Methodological Framework Linking Workspace Analysis, Trajectory Planning, and ML-Based Kinematics.

1.12 Thesis Structure

The remainder of this thesis is organized into five chapters as indicated below:

Chapter 2 provides a structured literature review derived from the background sections of Contributions 1, 2, and 3.

Chapter 3 presents the complete methodology and experiments related to three contributions.

Chapter 4 outlines results across the three studies

Chapter 5 concludes the thesis with reflections on key findings and discusses future directions including real-time reinforcement learning for surgical navigation.

Chapter 2 : Literature Review

2.1 Introduction

The purpose of this chapter is to present a comprehensive overview of the research landscape underpinning the development of modular C-arm fluoroscopy systems integrated with multi-degree-of-freedom operating tables. While Chapter 1 established the motivation and objectives of this thesis, the present chapter situates the proposed research within the broader context of existing technological innovations, theoretical frameworks, and clinical practices. This review emphasizes historical advancements, theoretical foundations in kinematics, trajectory planning strategies, and the emerging role of artificial intelligence (AI) in surgical imaging and positioning.

Over the past three decades, surgical imaging has transitioned from static, manually operated systems to dynamic, computer-controlled platforms capable of real-time, multi-dimensional visualization. C-arm fluoroscopy systems, traditionally deployed for intraoperative imaging, have evolved from simple two-dimensional radiography to three-dimensional and cone-beam computed tomography -capable devices. Parallel advancements in operating tables, ranging from fixed to multi-DoF robotic variants, have enabled greater procedural flexibility, particularly for complex orthopaedic, cardiovascular, and spinal surgeries. The integration of these two systems not only enhances clinical workflow efficiency but also presents unique kinematic and control challenges.

This chapter is structured into five thematic areas:

- **Evolution of C-arm fluoroscopy and integrated table systems**: Presenting a historical perspective and highlighting technological transitions from manual to robotic systems.
- **Kinematic modelling and surgical workspace analysis**: Summarizing foundational methods for modelling robotic systems and evaluating their spatial and dexterity performance.
- **Motion planning and trajectory optimization**: Reviewing conventional trajectory planning algorithms and their application to constrained surgical environments.
- **Machine learning-driven kinematic modelling frameworks**: Focusing on data-driven pose prediction, inverse kinematics (IK) approximation, and algorithmic enhancements using AI.
- **Summary of research gaps**: Identifying unresolved challenges and motivating the unified modelling, trajectory planning, and AI integration proposed in this thesis.

By synthesizing contributions from these diverse research streams, this chapter provides the foundation for the novel methodologies and experimental analyses developed in Chapters 3 and 4. Emphasis is particularly placed on identifying knowledge gaps, including the limited focus on combined C-arm with table kinematics, insufficient integration of trajectory planning with ML-driven inverse kinematics, and the lack of robust, data-driven approaches for collision-free pose prediction in clinical settings.

2.2 Evolution of C-arm Fluoroscopy and Integrated Table Systems

2.2.1 Minimally Invasive Surgery: A Paradigm Shift

The concept of Minimally Invasive Surgery emerged in the late 20th century as a transformative shift from traditional open surgery to approaches designed to reduce tissue trauma, accelerate recovery, and minimize postoperative complications. MIS techniques such as laparoscopic cholecystectomy, arthroscopy, and endovascular interventions were enabled by two fundamental advancements: (1) the refinement and miniaturization of surgical tools, a process that began nearly 5000 years ago with early civilizations using primitive instruments such as copper knives, hollow tubes, catheters, and specula [60–66], and (2) the genesis of sophisticated visualization techniques enabling surgeons to meticulously inspect internal anatomy without resorting to extensive incisions was precipitated by transformative shifts in surgical philosophy regarding incision dimensions [67]. Although expansive abdominal incisions were once revered as emblematic of surgical prowess and professional audacity throughout the late nineteenth and early twentieth centuries, they were concurrently recognized for their invasiveness, morbidity, and patient discomfort [68, 69]. Consequently, evolving surgical paradigms driven by an increasing predilection for conservative, tissue-preserving interventions catalyzed a renaissance in minimally invasive approaches, ultimately giving rise to contemporary MIS procedures emblematic of modern surgical innovation.

Table 2.1: Historical Timeline of Early Minimally Invasive Surgery (MIS) Techniques (3000 BC–1850 AD).

Period	Historical Contributor (Region)	Key Innovations and Contributions
~3000 BC	Sumerians	Copper knives for surgery, gold malleable catheters [70]
~2400 BC	Egyptians	Bronze surgical instruments (scalpels, needles) [71]
3100–539 BC	Mesopotamian Empire	Hollow reeds, bronze, lead, and copper tubes for minimally invasive medication delivery [72]
~1300 BC	Babylonian Talmud	Early description of speculum use [73, 74]
800–600 BC	India (Susruta Samhita)	Rectal specula, nasal and oral specula, foreign body extraction instruments [75-78]
~460 BC	Greece (Hippocratic corpus)	Rectal speculum, catheters, minimally invasive vaginal instruments [79, 80]

~310–250 BC	Greece (Erasistratus, Oreibasis)	Curved urethral catheter designs, urethral dilation [65, 70]
1st century BC	Archigenes (Rome)	Cervical mirrors for internal inspection [65]
79 AD	Pompeii	Vaginal mirrors, rectal specula
936–1009 AD	Al Zahrawi (Arab)	Screw-operated glass speculum [66]
1587	Giulio Cesare Aranzi (Italy)	Early nasal endoscope with artificial water-based lighting [80]
~1750	George Arnaud de Ronsil (France)	Covered lantern and convex lens system for vaginal inspection [81]
1806–1807	Philipp Bozzini (Germany)	"Der Lichtleiter"—First organized endoscopic illumination system (candles, mirrors) [82]
1826	Pierre Ségalas (France)	Speculum urethra-cystique with candles and reflective mirrors [83]
1827	John Fisher (USA)	Z-shaped hollow tube instrument for examining vagina, bladder, and urethra [84]
Early 1800s	Jean Civiale (France)	Endoscopic transurethral lithotripsy, irrigation systems, retractable scalpels [85]
1834	Jean Pierre Bonnafont (France)	Otoscope with lens and reflective mirrors [86]
1843	Antonin Jean Desormeaux (France)	Portable cystoscope with gasogene lamp for endoscopic urological interventions [85, 87]
Mid-1800s	John Avery (UK)	Early cystoscope and laryngoscope using Palmer's lamp [88]

The introduction of high-quality imaging systems was pivotal in accelerating MIS adoption. C-arm fluoroscopy particularly provided real-time visualization during orthopedic [89], vascular [90], and spinal procedures [91], while endoscopic systems offered magnified views for abdominal and thoracic surgeries [92]. These innovations not only reduced surgical morbidity but also changed the workflow in operating rooms, demanding greater integration of imaging, patient positioning, and navigation technologies.

2.2.2 Historical Background of Fluoroscopy and the Emergence of C-arm Imaging

The trajectory of fluoroscopy spans more than a century, beginning with Wilhelm Roentgen's seminal discovery of X-rays in 1895, when he first observed their ability to elicit phosphorescence in a barium platinocyanide screen [93]. Early implementations of fluoroscopy were rudimentary and perilous: unstable X-ray tubes, unshielded high-voltage wiring, and ozone emissions exposed operators to grave hazards, resulting in radiation burns, amputations, and, in some cases, mortality among pioneering radiologists [94]. Nevertheless, by the dawn of the twentieth century, fluoroscopy had already become entrenched as a routine diagnostic modality, offering dynamic visualization capabilities that static radiographs could not provide due to protracted exposure times and cumbersome photographic processing requirements [93].

By the 1940s, fluoroscopic technology had matured to a stage where equipment demanded minimal operator intervention, enabling radiologists to focus more fully on diagnostic interpretation [93]. Scholarly discourse of that era addressed image degradation from quantum noise, the perceptual consequences of dark adaptation on visual analysis, and the need to balance image brightness against radiation burden [93]. A transformative leap occurred in the 1950s with the advent of the X-ray image intensifier (II), which dramatically increased image luminance, thereby facilitating both real-time visual interpretation and cine-recording of vascular and gastrointestinal studies [95]. Further refinements followed in the mid-1970s, when cesium iodide (CsI) input screens supplanted earlier phosphors, yielding approximately a twofold gain in quantum efficiency [93]. Parallel advances in closed-circuit video technologies permitted indirect electronic viewing, obviating the need for direct optical coupling and enabling the proliferation of digital angiography [93].

The late 1970s and 1980s marked a decisive juncture with the clinical adoption of digital and analog subtraction angiography, techniques that substantially enhanced vascular visualization while simultaneously reducing radiation exposure by enabling spectral shaping of X-ray beams to optimize iodine contrast absorption [94]. These innovations catalyzed the rapid expansion of interventional radiology, where real-time image guidance became indispensable for minimally invasive procedures [96]. By the early 2000s, flat-panel (FP) solid-state detectors began to supplant traditional image intensifiers, retaining the CsI input architecture but offering improved spatial resolution, reduced geometric distortion, and more favorable dosimetric performance [94]. Concurrent developments in digital image processing including real-time noise suppression, motion compensation, and contrast enhancement further reduced patient dose while improving interpretability [94]. By the end of the 2000s, fluoroscopic imaging hardware had reached relative technological stability, with subsequent improvements emphasizing computational enhancements rather than radical hardware redesign [94].

It was within this evolutionary continuum that C-arm fluoroscopy systems emerged in the 1950s as a disruptive innovation in intraoperative imaging [94]. The distinctive design consisting of an X-ray source

and detector affixed to opposite ends of a semi-circular gantry enabled orbital motion around the patient without necessitating physical repositioning. Although early C-arms were analog and mechanically constrained, they endowed surgeons with unprecedented capacity to verify bone alignment and fixation in real time, a capability revolutionary for trauma and orthopedic surgery [94].

The clinical expansion of minimally invasive surgery in the 1980s and 1990s heightened demand for imaging systems that could deliver dynamic multi-angle visualization within spatially constrained operating rooms. Surgeons increasingly required platforms capable of adapting to diverse anatomical access corridors while preserving sterile workflow integrity. The maneuverability and orbital freedom of the C-arm design directly addressed these exigencies, facilitating its widespread integration into orthopedic, cardiovascular, and spinal procedures [97]. The subsequent transition from analog to digital flat-panel detectors, the integration of cone-beam computed tomography and most recently, the advent of robotic C-arms with automated trajectory planning represents the natural culmination of this technological lineage each iteration systematically ameliorating limitations in resolution, radiation efficiency, and ergonomic usability [98].

2.2.3 Digital Imaging and the MIS Revolution

The transition from analog to digital imaging during the 1990s constituted a decisive technological inflection point in intraoperative visualization. The advent of flat-panel detectors (FPDs) supplanted traditional image intensifiers, conferring substantial advantages in spatial resolution, radiation efficiency, and digital archiving. This paradigm shifts not only enhanced the fidelity of intraoperative visualization but also markedly attenuated patient and operator radiation burden, thereby strengthening the clinical rationale for image-guided interventions [93].

Concurrently, the global proliferation of minimally invasive surgery accelerated the clinical demand for precise, ergonomic, and radiation-conscious imaging systems. Landmark procedures such as laparoscopic cholecystectomy, percutaneous spinal fixation, and catheter-based vascular interventions became emblematic of the MIS revolution, necessitating imaging platforms that could provide dynamic, multi-angle guidance within constrained operative environments. The mobile digital C-arm emerged as an indispensable adjunct in this era, particularly for guiding complex interventions such as percutaneous nephrolithotomy, spinal instrumentation, and orthopedic fracture reconstruction. Its adaptability and image quality rendered it a cornerstone technology, effectively bridging the gap between surgical precision and minimally invasive access corridors [95].

2.2.4 Introduction of 3D Imaging and Hybrid Operating Rooms

The early 2000s heralded the advent of hybrid operating rooms, which strategically integrated state-of-the-art C-arm systems with computed tomography or cone-beam computed tomography modalities. This convergence empowered surgeons to acquire high-fidelity three-dimensional volumetric reconstructions

intraoperatively, thereby enhancing procedural accuracy for technically demanding interventions such as spinal deformity correction, transcatheter aortic valve implantation, and complex neurovascular embolization [95].

These hybrid environments embodied the ethos of minimally invasive surgery , coupling reduced access trauma with uncompromised visual precision. By enabling image-guided navigation through diminutive incisions, hybrid imaging minimized surgical morbidity while safeguarding device accuracy. Notably, intraoperative CBCT demonstrated the capacity to facilitate percutaneous pedicle screw placement with sub-millimetric precision, thereby obviating dependence on postoperative CT verification and substantially diminishing the incidence of revision surgeries [96].

2.2.5 Evolution of Operating Tables and Integration with Imaging

The evolution of operating tables has paralleled, and in many respects enabled, the broader transformation of image-guided and minimally invasive surgery. Early operating tables were essentially static platforms, offering only rudimentary adjustments such as elevation, tilt, and Trendelenburg positioning. While adequate for conventional open procedures, these limited degrees of freedom proved insufficient as surgical paradigms shifted toward minimally invasive surgery , where complex anatomical access and precise intraoperative imaging became indispensable.

To meet these escalating clinical demands, modern operating tables have been engineered with multi-DoF capabilities, incorporating longitudinal, lateral, and vertical translations in addition to refined pitch and roll adjustments. This expanded mobility allows surgeons to achieve anatomically optimized orientations, thereby enhancing procedural accuracy and reducing the ergonomic burden associated with constrained operating room geometries.

The integration of advanced operating tables with C-arm fluoroscopy systems has marked a decisive inflection point in intraoperative imaging. Through mechanical and electronic coupling, these platforms achieve coordinated, collision-free movements that minimize manual repositioning while preserving sterility and workflow efficiency. Such synergy not only facilitates access to anatomically challenging regions but also supports seamless image acquisition across diverse procedural contexts, from orthopedics to cardiovascular interventions.

Importantly, this integration has converged with the emergence of hybrid operating rooms, where state-of-the-art C-arm platforms and multi-DoF operating tables coalesce to provide an adaptable surgical environment. Evidence from systematic reviews has underscored the value of these hybrid ORs in improving readiness for emergency procedures, while cardiovascular medicine has embraced their potential to streamline complex interventions such as transcatheter valve repair and aortic stent-graft deployment

[99]. Collectively, these advances demonstrate that the co-evolution of operating tables and imaging systems is not merely incremental but rather foundational to the contemporary surgical ecosystem.

2.2.6 Robotic and Automated C-arm Systems

The contemporary evolution of C-arm fluoroscopy has been characterized by the incorporation of robotic motion control, trajectory automation, and sophisticated collision-avoidance algorithms. Unlike the manually operated systems, these robotic platforms often synergistically integrated with motorized operating tables can execute pre-programmed orbital sweeps and sustain consistent anatomical views with minimal operator intervention. Such automation is particularly advantageous in the milieu of minimally invasive surgery , where procedural precision, sterility preservation, and radiation safety are paramount. By standardizing imaging trajectories, robotic C-arms reduce operator variability, mitigate radiation exposure for surgical staff, and streamline intraoperative workflows.

Recent developments have further advanced this paradigm by embedding robotic C-arms within comprehensive navigation ecosystems for spinal and orthopedic surgery. For instance, the CUVIS-spine system has demonstrated the ability to couple intraoperative C-arm imaging with robotic guidance, performing real-time calibration, registration, and trajectory planning for pedicle screw placement with sub-millimetric fidelity, as validated in cadaveric experiments [100]. Whereas such orthopedic-focused platforms emphasize trajectory fidelity and intraoperative safety in MIS workflows, robotic CBCT systems in radiotherapy prioritize isocentric precision and volumetric guidance. A ceiling-mounted robotic CBCT system designed for integration with proton therapy demonstrated sub-millimetric positional repeatability (<0.5 mm), isocentric rotational accuracy within 0.7 mm, and volumetric guidance accuracy within 1 mm and 1° when tested on anthropomorphic phantoms [101]. Such systems illustrate that robotic C-arms can not only sustain intraoperative navigation accuracy but also align imaging and therapeutic isocentres with unprecedented precision, thereby underscoring their translational value beyond conventional operating rooms.

In broader clinical practice, these robotic C-arm systems now serve as pivotal components of hybrid operating rooms, where they facilitate automated cone-beam CT acquisition, dynamic repositioning, and compatibility with optical navigation frameworks. Collectively, these advances position robotic C-arms and their integration with intelligent operating tables as foundational pillars of next-generation image-guided interventions, advancing the trajectory toward fully automated, precision-driven surgical ecosystems.

2.2.7 Summary

This section has shown how the MIS revolution catalyzed continuous innovation in C-arm fluoroscopy and surgical table systems. The progression from rudimentary analog devices to contemporary robotic and table-integrated platforms illustrates how clinical demands for minimal invasiveness, precision, and

radiation efficiency directly shaped engineering advancements. Each technological milestone from image intensifiers and flat-panel detectors to hybrid operating rooms and robotic C-arms systematically addressed prior limitations in resolution, usability, and workflow integration. Parallel advancements in multi-DoF operating tables further enabled coordinated patient positioning and collision-free imaging, cementing their role as indispensable tools in modern minimally invasive surgery. The historical and technological synthesis in this section provides the foundation for the next section, which examines forward and inverse kinematics as the analytical framework for modelling and optimizing these integrated systems in intraoperative contexts.

2.3 Kinematic Modelling and Surgical Workspace Analysis

Kinematic modelling provides the mathematical framework for correlating joint variables with the pose of robotic manipulators, and its role in surgical robotics has been extensively examined across tool manipulators, navigation arms, and imaging systems. In the context of C-arm fluoroscopy integrated with multi-degree-of-freedom (DoF) operating tables, forward and inverse kinematics underpin the mapping between mechanical actuation and clinical workspace accessibility. This section surveys prior literature on forward/inverse kinematics, singularity analysis, and workspace characterization, highlighting gaps that motivate integrated modelling of C-arm and table systems.

2.3.1 Forward and Inverse Kinematics

Forward kinematics in surgical robotics is typically formulated using homogeneous transformation matrices or Denavit–Hartenberg (DH) parameters, which allow the mapping of joint variables to end-effector poses. This formulation has been successfully applied in rigid-link manipulators for orthopedic navigation and endoscopic procedures. However, inverse kinematics remains substantially more challenging due to the nonlinearities, redundancies, and anatomical constraints inherent in surgical environments. Closed-form IK solutions exist for specific serial structures, such as 6R manipulators, yet most surgical robots including tendon-driven or continuum designs necessitate iterative solvers. Methods such as the Jacobian pseudo-inverse, Newton–Raphson iterations, and BFGS gradient projection have demonstrated sub-millimetric accuracy in controlled settings, though their convergence is highly sensitive to initial guesses and they become unstable in the vicinity of kinematic singularities.

Recent research has extended IK analysis beyond rigid-link systems toward continuum robots, which offer enhanced dexterity and anatomical compatibility but exhibit complex elastic deformations under external loading. Traditional FK approaches using DH models are often sufficient to describe static configurations; however, IK solutions become ill-conditioned due to the coupling of segment position and orientation. To address this, a variable curvature model was proposed in tendon-driven continuum robots, which

incorporates load-induced deformation into the kinematic formulation. Building on this model, an enhanced inverse solver termed *FABRIKv* was developed, adapting the Forward and Backward Reaching Inverse Kinematics (FABRIK) algorithm to preserve real-time computation while compensating for deformation effects. Experimental validation confirmed that this approach maintained accuracy and stability even under load, extending the applicability of continuum robots to robot-assisted minimally invasive surgery (RMIS) where trajectory fidelity is critical. [102].

Parallel advancements in robotic surgical instrumentation have emphasized the integration of compact, highly articulated wrists at the distal end of instruments to overcome the limited degrees of freedom associated with rigid laparoscopic tools. A novel superelastic wire-driven design incorporating snake-like joints and universal joints has demonstrated the capacity to execute multi-DoF deflections and distal rotation. The FK and IK of this wrist mechanism were analytically derived, and experimental evaluation revealed an average motion deviation as low as 0.15 ± 0.08 mm with a maximum payload of 10 N. These results underscore the potential of hybrid cable-driven architectures to combine structural stiffness with dexterity, thereby enhancing suture performance and overall task execution in RMIS [103].

Collectively, these contributions highlight that while rigid-link FK/IK frameworks remain foundational, emerging continuum and cable-driven mechanisms necessitate novel modelling paradigms that account for compliance, load interactions, and real-time performance. Addressing these challenges is essential for enabling precise, safe, and ergonomically efficient image-guided interventions.

2.3.2 Surgical Workspace Characterization

Workspace analysis represents a fundamental evaluative tool in surgical robotics, as it delineates the set of attainable poses for an end-effector or imaging device subject to joint limits, anatomical boundaries, and collision constraints. In essence, workspace modelling enables the quantification of spatial reachability, procedural ergonomics, and safety margins within the highly constrained environment of the operating room. While originally formulated in the context of industrial manipulators, its application to surgical systems has expanded significantly, ranging from tool manipulators to navigation platforms.

Early methodologies for workspace determination emphasized geometric and numerical strategies, including discretized point-cloud mapping, volumetric sampling, and analytical boundary construction. For instance, Dumitru et al. developed a systematic design framework for polyarticulated robotic arms compatible with minimally invasive surgery , where workspace analysis was performed using numerical interpolation of vertebral joint configurations in modular snake-like robots [104]. Their findings underscored that effective MIS instruments require not only compactness and lightweight design but also maximized workspace efficiency within clinically constrained angular corridors. Such analyses emphasized

the importance of defining “effective workspace cones,” thereby linking kinematic feasibility with surgical usability.

Further refinement of workspace evaluation has been demonstrated in hybrid robotic systems that integrate camera manipulators with active surgical instruments. Pisla et al. presented a hybrid robot architecture where workspace generation was accomplished using an inverse geometric model constrained by a fixed remote center of motion (RCM) a critical feature for abdominal MIS[105]. Their numerical simulations revealed that patient-specific positioning and trocar access angles dramatically influence the attainable workspace volume, highlighting that improper robot–patient alignment can create unreachable cavities within the workspace. Importantly, they demonstrated how workspace analysis can guide optimal system placement in the operating theater, ensuring that anatomical targets remain accessible while preserving procedural safety.

Within the domain of imaging devices, workspace characterization plays an equally pivotal role. For C-arm fluoroscopy, volumetric workspace analysis is indispensable for quantifying anatomical coverage, avoiding collisions with the operating table, and ensuring ergonomic maneuverability in spatially constrained operating rooms. Yet, most published work has emphasized manipulators that interact directly with tissue, with far fewer contributions addressing imaging systems as active robotic participants. Bridging this gap requires adapting methodologies from manipulator workspace analysis such as voxelized volumetric mapping and collision-aware trajectory sampling to the integrated C-arm and table context. By doing so, one can generate precise collision-free workspaces that simultaneously respect kinematic constraints of both imaging and patient-support platforms.

Collectively, these contributions illustrate that workspace analysis in surgical robotics is not merely an academic exercise but rather a clinical imperative. For MIS-compatible manipulators, it defines ergonomic and safe zones of action; for hybrid surgical robots, it informs optimal system positioning relative to the patient; and for C-arm fluoroscopy, it establishes the foundation for collision-free imaging trajectories that enhance intraoperative efficiency. This underscores the need for dedicated frameworks that explicitly integrate imaging devices into workspace analyses an omission this dissertation directly addresses.

2.4 Motion Planning and Trajectory Optimization

Motion planning in surgical robotics refers to the generation of feasible, collision-free, and dynamically admissible paths that enable the robotic system to transition between desired poses while satisfying anatomical and procedural constraints. In the context of C-arm fluoroscopy integrated with multi-DoF operating tables, trajectory optimization is particularly critical: unlike conventional manipulators, imaging devices must preserve radiation efficiency, avoid collisions with the patient and surrounding equipment, and maintain ergonomic operability within constrained operative spaces.

2.4.1 Fundamentals of Trajectory Planning

Trajectory generation can be broadly categorized into task-space approaches, where Cartesian end-effector trajectories (e.g., source–detector axis paths) are specified and subsequently mapped into joint space via inverse kinematics, and joint-space approaches, where joint profiles are directly parameterized. The choice of domain depends on the clinical context: task-space planning aligns with imaging requirements (e.g., maintaining a projection angle), whereas joint-space planning is often more efficient for real-time control. Both approaches must enforce joint limits, velocity/acceleration bounds, and collision-avoidance constraints.

- **Task Space** – defining Cartesian paths of the imaging plane or X-ray source-detector axis and then mapping to joint space via IK.
- **Joint Space** – directly parameterizing joint angles and displacements, often used for real-time implementations.

2.4.2 Trajectory Profiles for Surgical Applications

Trajectory planning in surgical robotics requires generating smooth, safe, and dynamically feasible paths that respect anatomical, ergonomic, and mechanical constraints. Several canonical trajectory families such as trapezoidal velocity, polynomial, spline-based, and biologically inspired profiles have been adapted from industrial robotics into the surgical domain. Recent scholarship, however, has broadened this space by incorporating optimization frameworks, spline interpolation techniques, and clinical case specific algorithms that address the unique constraints of image-guided and minimally invasive procedures.

Polynomial-Based Trajectories:

Polynomial interpolation, particularly cubic and quintic formulations, remains one of the most widely adopted strategies for surgical manipulators because of its guaranteed continuity of position, velocity, and acceleration. Fifth-order polynomials have particularly been shown to balance computational efficiency with motion smoothness, yielding torque profiles comparable to those obtained via optimized techniques such as genetic algorithms or particle swarm optimization. Comparative studies on multi-DoF surgical microrobots suggest that polynomial profiles can achieve near-optimal energy efficiency while maintaining low computational overhead, making them suitable for real-time intraoperative deployment [106].

Spline and NURBS-Based Trajectories:

Spline methods, including B-splines and Non-Uniform Rational B-Splines (NURBS), extend polynomial interpolation by enabling local curve adjustments without perturbing the entire trajectory. This property is

particularly advantageous in surgical contexts where intraoperative adjustments are often required to account for anatomical variability or unexpected events. Recent work on dual-arm surgical robots has demonstrated that NURBS-based interpolators can generate smooth trajectories with controlled chord error, uniform feed rates, and high geometric fidelity, while also integrating collision detection algorithms to preserve safety in dynamic surgical environments [107].

Optimization-Driven Profiles:

Optimization-based methods, such as genetic algorithms, pattern search, and particle swarm optimization, have increasingly been applied to refine surgical trajectories. Notably, time-optimal planning frameworks that incorporate jerk continuity through segmented polynomials (e.g., 4-7-4 interpolations) and locally chaotic particle swarm optimization (LCPSO) have achieved reductions of more than 40% in execution time compared with traditional approaches, without compromising smoothness or stability. Such results underscore the potential of hybrid methods that combine classical trajectory families with metaheuristic optimization to meet both temporal and safety constraints of intraoperative workflows [108].

Application-Specific Trajectory Planning:

Beyond general interpolation and optimization, clinical application–specific trajectory planning has emerged as a major research focus. In the context of percutaneous ablation, for instance, needle trajectory planning algorithms must satisfy hard constraints such as avoidance of critical structures and maintenance of adequate insertion angles, while also optimizing soft constraints like minimizing healthy tissue traversal. Studies of computer-assisted radiofrequency and microwave ablation planning have demonstrated that optimization strategies ranging from simplex search to Pareto optimality can significantly reduce inter-operator variability and improve procedural outcomes [109]. These insights are transferable to imaging trajectory design, where analogous trade-offs exist between anatomical accessibility, radiation exposure, and system dexterity.

2.4.3 Lookup Table and Workflow Integration

Although optimization-based and adaptive trajectory planners are mathematically elegant, their intraoperative deployment is often constrained by computational latency and surgeon workflow demands. As a pragmatic alternative, many surgical robotics platforms employ lookup tables precomputed libraries of feasible trajectories and joint configurations that can be rapidly queried during a procedure. In image-guided interventions, LUTs function as decision-support mechanisms, providing interventionalists with immediate access to validated motion strategies while minimizing cognitive overhead [110].

Early fluoroscopy-guided surgical robots already relied on LUT-like paradigms to encode canonical device poses for specific tasks, demonstrating that precomputed strategies could expedite intraoperative positioning without requiring extensive computation [110]. Building on these foundations, contemporary research has emphasized LUTs as a mechanism to enhance stability and safety in anatomically constrained environments. For instance, respiration-induced motion variability during spinal laminectomy has been mitigated through LUT-based motion controllers that ensure trajectory robustness despite dynamic perturbations [111].

At the same time, LUT frameworks align with broader efforts toward autonomous or semi-autonomous surgical control, where reducing reliance on continuous human input improves reproducibility and safety [112]. Beyond classical joint–pose mappings, recent studies have demonstrated data-driven LUTs that embed learned inverse models, enabling soft robotic actuators to achieve real-time, patient-specific inverse control by interpolating across a dense grid of pre-validated trajectories [113]. This paradigm illustrates how LUTs can evolve from static pose libraries into intelligent, adaptive repositories that seamlessly integrate physics-based simulation, experimental validation, and machine learning.

From a workflow perspective, LUTs confer three primary advantages: (i) efficiency, by allowing rapid recall of validated C-arm poses for standard projections; (ii) robustness, by encoding trajectories with pre-analyzed singularity and collision margins; and (iii) clinical adaptability, by permitting procedure-tailored parameterization based on patient-specific preoperative data [114]. These attributes collectively reduce operator variability and facilitate safer intraoperative execution.

Thus, LUTs should not be viewed as static repositories but rather as dynamic, clinically adaptive frameworks the bridge between computationally intensive preoperative planning and real-time surgical execution. By embedding both conventional optimization results and learned kinematic mappings, LUTs can transform trajectory planning from a purely theoretical construct into a reliable, surgeon-accessible tool for daily clinical workflows [113].

2.5 Machine Learning for Kinematics Modelling

Kinematic modelling constitutes a foundational element of robotic motion planning and control [115], particularly in surgical robotics where millimetric precision, operational safety, and real-time adaptability are paramount. Classical approaches to forward and inverse kinematics (FK and IK) have traditionally relied on analytical solvers derived from geometric or algebraic formulations [116]. While tractable for low-degree-of-freedom manipulators, these methods exhibit critical limitations when applied to high-DoF systems such as modular C-arm fluoroscopy devices. Nonlinear coupling, redundancy, and scalability bottlenecks often impede the stability of closed-form or iterative solutions, motivating the transition toward data-driven alternatives.

Recent research has demonstrated that supervised machine learning (ML) techniques can approximate inverse kinematics with clinically admissible fidelity. Deep neural networks (DNNs) and ensemble-based regressors have proven effective in capturing the nonlinear, multivariate relationships between end-effector poses and joint variables [117–121]. For example, Xiao et al. [117] introduced a Long Short-Term Memory (LSTM) framework for tendon-driven continuum robots, effectively compensating for cable slack and hysteresis while preserving temporal consistency. Relaño et al. [118] extended Gaussian Process (GP) regression and its approximate variants to soft robotic arms, illustrating superior uncertainty modelling and generalization compared to shallow neural baselines. In a complementary direction, Kinoshita et al. [119] proposed a Newton-inspired IK solver combining ridge regression with adaptive regularization, accelerating convergence without sacrificing accuracy. In the domain of rehabilitation robotics, Shah et al. [120] demonstrated that DNN-based solvers can achieve higher joint angle precision than analytic IK formulations. Hsieh and Hou [121] further advanced the field with a model-free, end-to-end control framework for multi-input multi-output (MIMO) robots, underscoring the potential of deep learning to bypass computationally intensive symbolic modelling.

Although forward kinematics is analytically less burdensome, ML approaches have also been applied to improve accuracy in redundant or hybrid systems, particularly when auxiliary DoFs such as operating tables are introduced. Cho et al. [122] developed a deep decoder network capable of reconstructing the full configuration of tendon-driven continuum robots from sparse point-cloud data, effectively mitigating hysteresis effects. Singh et al. [123] compared analytical, geometric, numerical, and AI-based FK strategies for a 6-axis humanoid manipulator, concluding that deep learning approaches offered superior adaptability under nonlinear and dynamically evolving conditions.

Dimensionality reduction techniques have further enriched ML-based kinematic modelling by enhancing efficiency and interpretability. Shimizu et al. [124] utilized Functional Principal Component Analysis (FPCA) to synthesize humanoid full-body motions in low-dimensional latent spaces while preserving biomechanical plausibility. Carreira et al. [125] applied PCA to a vision-based robotic localization system, achieving real-time inference without explicit feature engineering. Extending this paradigm, Tamimi and Zell [126] incorporated Kernel PCA with fractional polynomial kernels to bolster robustness against noise in robotic visual localization. Ra et al. [127] hybridized PCA with evolutionary computation, designing a genetic operator that optimized humanoid motions for energy efficiency while satisfying dynamic constraints.

Taken together, these advances underscore a broader paradigm shift from purely symbolic to intelligent, data-driven kinematic modelling. ML frameworks especially those leveraging deep networks and dimensionality reduction offer flexible mappings between Cartesian and joint spaces, effectively addressing nonlinearities, redundancy, and high-dimensional motion planning challenges. Yet, despite their promise,

no study has articulated a unified ML framework that simultaneously addresses both FK and IK in the context of intraoperative imaging systems, particularly modular C-arms integrated with multi-DoF operating tables.

2.6 Summary and Research Gaps

This chapter has surveyed the evolution of intraoperative imaging and motion planning, beginning with the historical development of C-arm fluoroscopy and operating tables, progressing through the mathematical foundations of forward and inverse kinematics, and culminating in contemporary advances in trajectory optimization and machine learning. The literature demonstrates that while C-arm fluoroscopy has evolved from rudimentary analog systems to robotic, cone-beam CT–enabled platforms, research into its kinematic integration with multi-DoF operating tables remains sparse. Similarly, although trajectory planning algorithms ranging from polynomial interpolations to optimization-based profiles and lookup tables have been successfully applied to industrial and surgical manipulators, their translation to image-guided surgical ecosystems is constrained by computational latency, anatomical variability, and static workflow assumptions. Finally, while machine learning has shown promise in approximating complex forward and inverse kinematics with real-time inference, few studies have systematically validated these models against the unique requirements of high-DoF C-arm–table architectures in constrained clinical environments.

To address these gaps, this dissertation proposes a unified methodological framework articulated across three contributions. First, collision-free workspace analysis of integrated C-arm–table configurations is undertaken to quantify how additional DoFs expand anatomical reachability while avoiding collisions. Second, trajectory planning paradigms embedding patient-specific constraints and operationalized via lookup tables are designed to enable smooth, dynamically feasible, and clinically translatable transitions between imaging poses. Third, data-driven machine learning models are developed and validated to approximate forward and inverse kinematics, offering real-time inference capabilities that surpass the computational bottlenecks of classical solvers. Collectively, these contributions aim to bridge the divide between theoretical modelling and practical intraoperative deployment, establishing the groundwork for intelligent, adaptive, and clinically viable motion planning in modular C-arm fluoroscopy systems. We conclude by emphasizing here that robotic C-arms are costly (i.e. >>$1M-$2M) and are typically found in luminary hospitals worldwide. We remind the reader that our aim is to provide solutions for manually operated systems prevalent in low-to-middle-income countries and underfunded healthcare settings.

Chapter 3 : Methodology

3.1 Kinematic Model of Integrated C-arm fluoroscope and operating table

3.1.1 Description of OEC 3D C-arm and CMAX^{TM} X-RAY Operating table

The imaging system analyzed in this thesis consists of the GE OEC 3D C-arm integrated with the Steris CMAX™ X-ray Operating table, combining translational and rotational mobility to enhance intraoperative imaging flexibility. We note here that any other C-arm device and operating table model can be used for the proposed methodology as well as their respective range of motion specifications determined by the manufacturers. The GE OEC 3D C-arm system is a mobile fluoroscopic imaging platform characterized by six degrees of freedom comprising both translational and rotational movements as shown in Fig. 3.1.

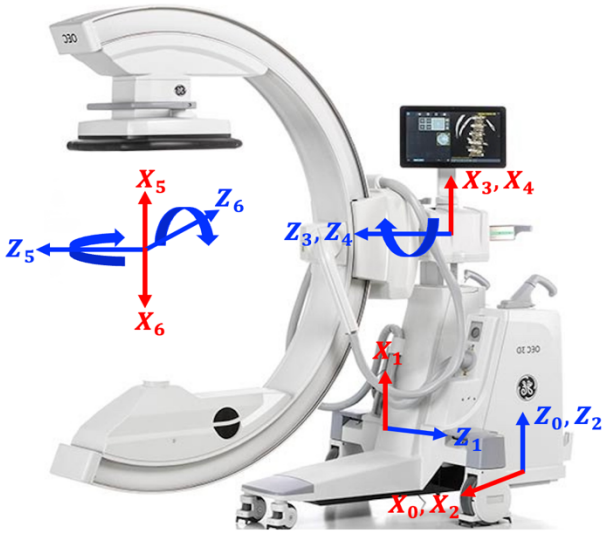

Figure 3.1: Joints of GE OEC 3D C-arm [128].

The C-arm architecture integrates three prismatic joints and three revolute joints, enabling precise manipulation of the imaging source and detector around the patient. The prismatic joints include the C-arm Lateral translation, with a symmetric range of ±0.5 meters; the C-arm Vertical translation, permitting vertical displacement between 0 and 0.46 meters; and the C-arm Horizontal translation, allowing forward motion up to 0.15 meters. Rotational mobility is achieved through the revolute joints: the C-arm Wigwag rotation provides yaw adjustments within ±10°, the C-arm Tilt rotation supports extensive pitch articulation from –90° to 270°, and the C-arm Orbital rotation enables roll motion from –100° to 100°.

The CMAX™ X-ray Operating table [129] augments the operational flexibility of the C-arm imaging system by providing three additional prismatic degrees of freedom for patient positioning, as illustrated in Fig. 3.2. The Table Vertical joint provides vertical elevation from 0 to 0.36 meters, the Table Longitudinal

joint allows translation along the head-to-foot axis with a range of 0 to 0.7 meters, and the Table Transverse joint supports lateral motion from -0.13 to 0.13 meters. Although the CMAX™ table is mechanically equipped with rotational capabilities (table roll and yaw), these two rotational degrees of freedom are deliberately excluded from the system model to preserve patient stability and ensure procedural safety. Rotational adjustments during surgery may increase the risk of inadvertent patient movement, and potentially disrupt the precise alignment required for image-guided interventions or delicate anatomical access.

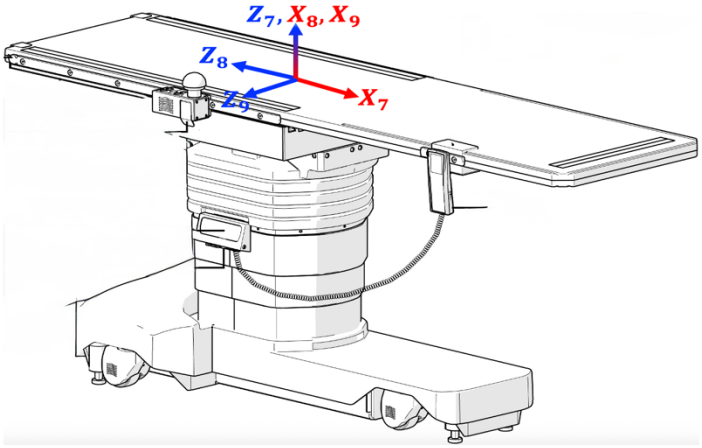

Figure 3.2: Joints of Steris CMAX™ X-ray Operating table [129].

The joint limits of the GE OEC 3D C-arm and CMAX™ X-ray Operating table define the operational workspace and mechanical boundaries of the integrated system. These constraints were rigorously embedded within the kinematic modelling, workspace analysis, and inverse kinematics computations to ensure that all predicted and simulated configurations remained within the physically realizable domain. By strictly enforcing these limits, the analysis guarantees mechanical feasibility across all modular C-arm configurations, supporting reliable and clinically deployable motion planning strategies. The integration of the C-arm's combined translational and rotational degrees of freedom with the operating table's prismatic motions substantially enlarges the effective surgical workspace enabling adaptive positioning across diverse anatomical targets. This expanded mobility supports efficient intraoperative imaging across complex trajectories, optimizing access and visualization while upholding procedural safety and spatial precision. The Denavit–Hartenberg parameters defining the kinematic structure of the combined GE OEC 3D C-arm and CMAX™ X-ray Operating table are presented in Table 3.1. These parameters serve as the foundational representation for the system's forward and inverse kinematics formulations, capturing the joints of the C-arm and the operating table within a unified kinematic model.

Table 3.1: DH Parameterization of the GE OEC 3D C-arm and CMAX™ X-ray Operating table.

Joint	Link Length, a_i (m)	Link Twist, α_i (rad)	Link Offset, d_i (m)	Joint Angle, θ_i (rad)	Range
C-arm Lateral	0	0	d_1	0	$-0.5\ \text{m} \sim 0.5\ \text{m}$
C-arm Vertical	0	$-\pi/2$	d_2	0	$0 \sim 0.46\ \text{m}$
C-arm Wigwag	0	$\pi/2$	0	θ_3	$-10° \sim 10°$
C-arm Horizontal	0	0	d_4	0	$0 \sim 0.15\ \text{m}$
C-arm Tilt	0	$-\pi/2$	0	θ_5	$-90° \sim 270°$
C-arm Orbital	0	$\pi/2$	0	θ_6	$-100° \sim 100°$
Table Vertical	0	0	d_7	0	$0 \sim 0.36\ \text{m}$
Table Longitudinal	0	$-\pi/2$	d_8	0	$0 \sim 0.7\ \text{m}$
Table Transverse	0	$\pi/2$	d_9	0	$-0.13\ \text{m} \sim 0.13\ \text{m}$

3.1.2 Joint Annotation and System Configuration

To standardize kinematic modelling, Table 3.2 summarizes the abbreviations, joint types, and functional descriptions of all joints used in the C-arm and integrated operating table system. Six degrees of freedom are attributed to the C-arm itself, comprising four prismatic joints (lateral, vertical, horizontal) and two revolute joints (wigwag, tilt, orbital). The integrated operating table contributes up to three additional prismatic joints: vertical lift, longitudinal slide, and transverse slide. This nomenclature facilitates consistent formulation of workspace analysis and inverse kinematics across configurations ranging from 5DoF to 9DoF.

From an actuation standpoint, all joints are assumed to be motor-driven with mechanical transmission elements, reflecting the architecture commonly adopted in clinical C-arm and surgical table systems. Revolute joints are actuated through geared rotary drives, enabling precise angular positioning while accommodating the high torque demands associated with the mass and inertia of the imaging gantry. Prismatic joints are realized through rotary-to-linear motion conversion mechanisms, such as ball-screw,

leadscrew, or belt-driven assemblies whereby rotational motion generated by an electric motor is transformed into translational displacement of the joint.

In the present work, the kinematic model abstracts these actuation and transmission details and represents each joint according to its resulting degree of freedom revolute or prismatic without explicitly modeling internal gear ratios, screw leads, or transmission compliance. This abstraction is consistent with standard practice in robot kinematics, where the focus lies on the geometric relationship between joint variables and end-effector pose rather than on low-level actuator dynamics. Nevertheless, the computed-torque framework has been discussed in Section 3.3.3. This modeling choice enables accurate workspace analysis and inverse kinematics formulation while maintaining generality across different C-arm and operating table design whose internal actuation mechanisms may vary between manufacturers but result in equivalent kinematic behavior at the joint level.

Table 3.2: Summary of joint abbreviations, joint types, and functional descriptions for the C-arm and integrated operating table.

Joint Name	Abbreviation	Joint Type	Description
C-arm Lateral	CL	Prismatic (P)	Lateral translation along X-axis
C-arm Vertical	CV	Prismatic (P)	Vertical translation along Z-axis
C-arm Wigwag	CW	Revolute (R)	Axial rotation around patient (yaw rotation)
C-arm Horizontal	CH	Prismatic (P)	Depth translation along Y-axis
C-arm Tilt	CT	Revolute (R)	Tilt up/down (pitch rotation)
C-arm Orbital	CO	Revolute (R)	Orbital rotation around patient longitudinal axis (roll rotation)
Table Vertical	TV	Prismatic (P)	Elevation of the operating table (vertical lift)
Table Longitudinal	TL	Prismatic (P)	Translation along patient head-foot direction (longitudinal axis)
Table Transverse	TT	Prismatic (P)	Lateral translation of table (sideways motion)

3.2 Methodology for Contribution 1: Numerical FK/IK and Workspace Analysis

3.2.1 Forward Kinematics

The forward kinematics of the integrated C-arm and operating table system was modelled using the Denavit–Hartenberg convention, enabling systematic computation of the end-effector pose from joint variables. Separate FK models were first developed for the GE OEC-3D isocentric C-arm and the Steris

CMAX operating table. These models were subsequently combined into a unified n-DoF kinematic chain, representing configurations ranging from 5-DoF to 9-DoF depending on the active joint subset.

The DH-based kinematic models were validated using a MATLAB Simscape (R2023a) environment. Simplified solid models of the C-arm and table (boxes, cylinders, and extrusions) were created, and "transform sensor" blocks were used to measure the end-effector pose. For each subsystem (C-arm and table), 1000 random joint configurations were generated. The end-effector position and orientation obtained via DH transformations were compared against Simscape measurements. Orientation errors were quantified by quaternion differences, while translational discrepancies were measured using the Euclidean norm. In all cases, zero errors were observed, confirming equivalence between the DH and Simscape implementations.

I. Forward Kinematics of C-arm

The end-effector pose i.e., C-shaped joint pose w.r.t its base was obtained using DH parameters (Table 3.1). As a second approach, a Simscape environment was built using boxes, cylinder and other solid blocks (Figure 3.3), and the "transform sensor" [130] block was used to measure the end-effector's pose. The functioning of the Simscape C-arm model was visually inspected to ensure that the joint movements were according to the input joint values.

Table 3.3: DH Parameters of an Isocentric 5 DoF C-arm.

Frame	θ	d	a	α
1	0	$0.99 + l_1$	0	0
2	θ_2	0	0	$-\frac{\pi}{2}$
3	0	$0.5 + l_3$	0	0
4	$-\frac{\pi}{2} + \theta_4$	1	0	$\frac{\pi}{2}$
5	θ_5	0	0	0

Table 3.4: Joint Limits of 5DoF C-arm.

Joint Name	Joint Variable	Joint Limits
Vertical	l_1	$[0.0, 0.46]\ m$
WigWag	θ_2	$[-10°, 10°]$

Horizontal	l_3	$[0.0, 0.15]\ m$
Tilt	θ_4	$[-90°, 270°]$
Orbital	θ_5	$[-100°, 100°]$

In Table 3.3, C-arm joint values were represented as variables ($l_1, \theta_2, l_3, \theta_4, \theta_5$) for 5 DoF. Joint names and limits of these variables are presented in Table 3.4. The coordinate system axes for each frame is shown in Figure 4. The end-effector pose (transformation matrix) w.r.t C-arm base was calculated using equations (3.1) and (3.2).

$$T_n^{n-1} = \begin{bmatrix} cos\,\theta_n & -sin\,\theta_n\,cos\,\alpha_n & sin\,\theta_n\,sin\,\alpha_n & a_n cos\,\theta_n \\ sin\,\theta_n & cos\,\theta_n\,cos\,\alpha_n & -cos\,\theta_n\,sin\,\alpha_n & a_n sin\,\theta_n \\ 0 & sin\,\alpha_n & cos\,\alpha_n & d_n \\ 0 & 0 & 0 & 1 \end{bmatrix} \quad (3.1)$$

$$T_{end-effector} = \prod_n T_n^{n-1}\,;\, n\ is\ DH\ joints\ count \quad (3.2)$$

The coordinate system axes for the base and end-effector are shown in Figure 3.3. A random 1000 input joint values were generated, and the output poses were calculated using these two methods. The rotation and translation of output poses were compared separately. Rotation parameters were converted into quaternions (q_w, q_x, q_y, q_z), and then error between these two approaches was calculated using equation (3.3) [131].

$$R^{err} = \frac{\sum_n min\{\|q^{DH} - q^{Simscape}\|, \|q^{DH} + q^{Simscape}\|\}}{n} \quad (3.3)$$

The absolute mean error in each axis was calculated for the translation parameters in equations (3.4) - (3.6).

$$t_x^{err} = \frac{\sum_n \left|t_x^{DH} - t_x^{Simscape}\right|}{n} \quad (3.4)$$

$$t_y^{err} = \frac{\sum_n \left|t_y^{DH} - t_y^{Simscape}\right|}{n} \quad (3.5)$$

$$t_z^{err} = \frac{\sum_n \left|t_z^{DH} - t_z^{Simscape}\right|}{n} \quad (3.6)$$

In these equations, $\|\,.\,\|$ represents the Euclidean norm and $|\,.\,|$ represents the absolute value. The output poses obtained from these methods were matched exactly with zero errors. This shows that the poses obtained from DH-parameters matched with the Simscape model and both methods generate the exact same FK outputs.

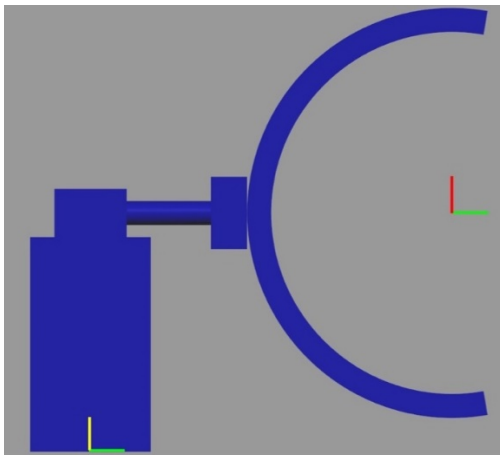

Figure 3.3: Isocentric C-arm Simscape model (side view). Bottom coloured axes are base coordinate axes and the axes on the right are C-arm end-effector coordinate axes. (Red: x-axis; Green: y-axis; Yellow: z-axis; follows right hand coordinate system order).

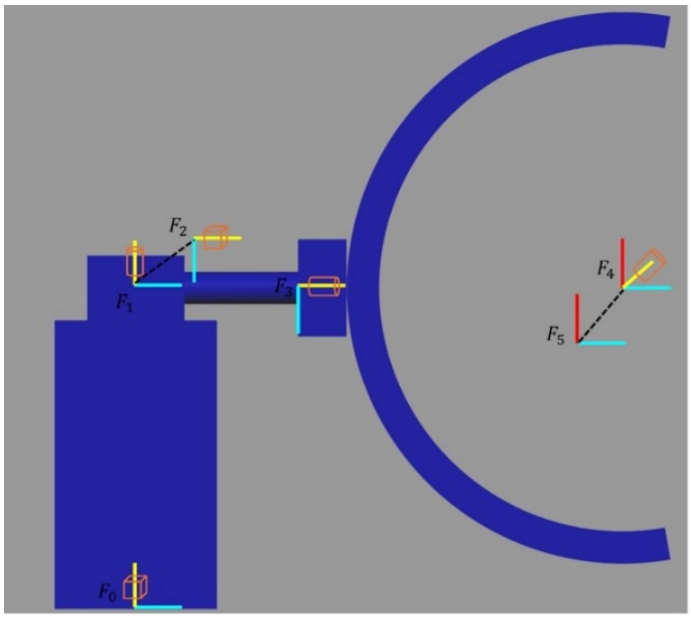

Figure 3.4: DH frames of an isocentric C-arm model with 5 DOF. translational and rotational movements represented with box and cylinder shapes respectively. (Red: x-axis; Cyan: y-axis; Yellow: z-axis; follows right hand coordinate system order; dashed line indicate both frames are at the same location.

II. Forward Kinematics of operating table

The center of the operating table's top surface was considered as the end-effector. Similar to section 3.2.1-I the pose of operating table end-effector w.r.t its base ($T_{table\_base}^{table\_ee}$) was achieved using two approaches: 1) DH parameters; 2) Simscape transform sensor. Again, both methods were compared by generating 1000

random input joint values and obtained zero errors proving table DH parameters kinematic model matched with the Simscape model. The operating table's DH parameters, joint names, variables, and limits are provided in Table 3.5 and Table 3.6.

Table 3.5: DH Parameters of 5 Dof Operating Table.

Frame	θ	d	a	α
1	0	$0.58 + l_1^t$	0	$-\frac{\pi}{2}$
2	$-\frac{\pi}{2} + \theta_2^t$	0	0	$\frac{\pi}{2}$
3	θ_3^t	0.05	0.025	0
4	0	l_4^t	0	$\frac{\pi}{2}$
5	0	l_5^t	0.075	$-\frac{\pi}{2}$

Table 3.6: Joint Limits of 5DoF Operating Table.

Joint Name	Joint Variable	Joint Limits
Vertical	l_1^t	$[0.0, 0.36]\ m$
Trend	θ_2^t	$[-30°, 30°]$
Tilt	θ_3^t	$[-20°, 20°]$
Longitudinal	l_4^t	$[0.0, 0.7]\ m$
Transverse	l_5^t	$[-0.13, 0.13]\ m$

The Simscape table model is shown in Figure 3.5 and each frame's coordinate system axes for DH approach are presented in Figure 3.6.

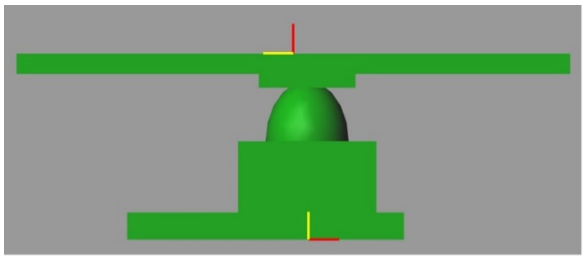

Figure 3.5: Operating table Simscape model (side view). Bottom coloured axes are base coordinate axes and the axes on the top are end-effector coordinate axes. (Red: x-axis; Green: y-axis; Yellow: z-axis; follows right hand coordinate system order).

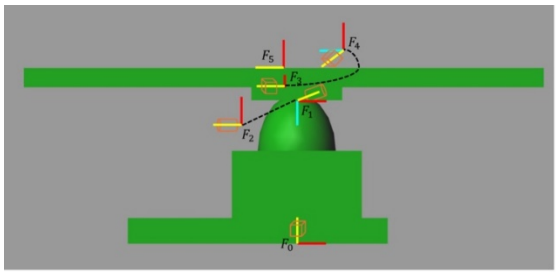

Figure 3.6: DH frames of a operating table with 5 DOF. Translational and rotational movements represented with box and cylinder shapes respectively. (Red: x-axis; Cyan: y-axis; Yellow: z-axis; follows right hand coordinate system.

A. Intial pose

The initial pose of the C-arm device and operating table was assumed such that when C-arm horizontal joint and table longitudinal joint values were configured to their center values i.e., 0.075 m and 0.35 m, and all other joint values were set to zeros, a vertical line (x-axis of C-arm end-effector) passes through the origin of both the C-arm device and table end-effector coordinate systems (Figure 3.7).

The two prismatic joints are configured to their center values so that they could move in both directions from their initial pose. With the ability to move joints in both directions, this setup could reach regions on both directions without repositioning both devices. At this assumed initial pose, except vertical joints all other joints have capability to move in both directions. Since both C-arm and table are located on the floor, the initial pose does not have impact on the vertical joints range as they move orthogonal to the floor plane.

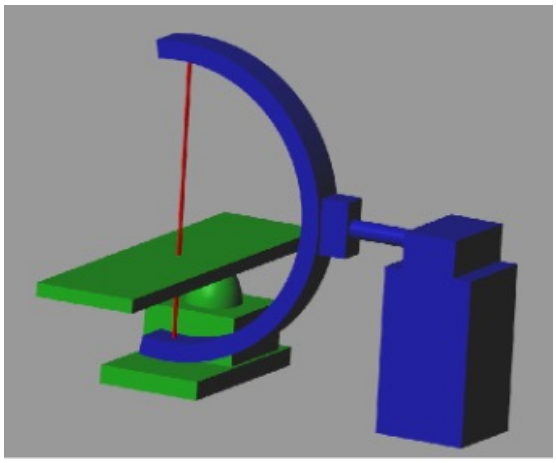

Figure 3.7: Initial pose assumption: C-arm and table end-effectors are aligned in a vertical straight line (red coloured line).

B. C-Arm with 6-DoF

The lateral movement of the C-arm device on the floor was designed as an additional DoF with joint limits from -0.5 m to 0.5 m. These limits were chosen based on the operating table length (2 m) such that from the initial pose by adjusting the lateral joint value, the C-arm could reach table quarter position on either side. In this thesis, apart from this lateral movement, both C-arm and table were assumed to be stationary (only joints could move but not the entire device or base of the device).

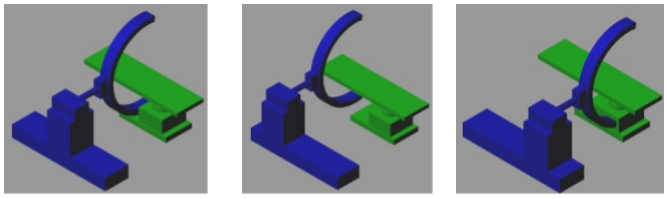

Figure 3.8: C-arm lateral movement on the floor. C-arm lateral joint value (a) 0 m; (b) -0.5 m; (c) 0.5 m.

Figure 3.8 shows C-arm and operating table setups with lateral joint values of 0 m, -0.5 m, and 0.5 m where other joints were configured to their initial pose values. Collision between the C-arm and operating table is discussed in the following section.

Forward kinematics for this C-arm with 6 DoFs was obtained using DH parameters and the Simscape model. Results from two methods were compared by generating 1000 random input joint values and obtained zero comparison error values using equations (3.3) – (3.6).

Table 3.7: DH Parameters of 6DoF C-arm Model.

Frame	θ	d	a	α
1	$\frac{\pi}{2}$	0	0	$\frac{\pi}{2}$
2	0	l_1^c	0	$-\frac{\pi}{2}$
3	$-\frac{\pi}{2}$	0	0	0
4	0	$0.99 + l_2^c$	0	0
5	θ_3^c	0	0	$-\frac{\pi}{2}$
6	0	$0.5 + l_4^c$	0	0
7	$-\frac{\pi}{2} + \theta_5^c$	1	0	$\frac{\pi}{2}$
8	θ_6^c	0	0	0

DH parameters are provided in Table 3.7, coordinate axes of DH frames are shown in Figure 9, and joint limits are presented in Table 3.8. The pose of 6 DoF C-arm's end-effector w.r.t its base ($T_{c-arm\_base}^{c-arm\_ee}$) was calculated using parameters presented in Table 3.7 and equations (3.1) – (3.2).

Table 3.8: Joint Limits of 6DoF C-arm.

Joint Name	Joint Variable	Joint Limits
Lateral	l_1^c	$[-0.5, 0.5]m$
Vertical	l_2^c	$[0.0, 0.46]\ m$
WigWag	θ_3^c	$[-10°, 10°]$
Horizontal	l_4^c	$[0.0, 0.15]\ m$
Tilt	θ_5^c	$[-90°, 270°]$
Orbital	θ_6^c	$[-100°, 100°]$

C. C-arm with operating table

In the initial pose setup, the relationship between C-arm and operating table was purely translational ($t_x = 0.4;\ t_y = 1.575;\ t_z = 0$). This translational transformation matrix is presented in (3.7). C-arm and operating table kinematic models were combined to find the pose of the C-arm w.r.t patient i.e., pose of C-arm's end-effector w.r.t operating table's end-effector ($T_{table\_ee}^{c-arm\_ee}$), which was obtained using (3.8) and (3.9).

$$T_{c-arm\_base}^{table\_base} = \begin{bmatrix} 1 & 0 & 0 & 0.4 \\ 0 & 1 & 0 & 1.575 \\ 0 & 0 & 1 & 0 \\ 0 & 0 & 0 & 1 \end{bmatrix} \quad (3.7)$$

$$T_{c-arm\_base}^{table\_ee} = T_{c-arm\_base}^{table\_base}\, T_{table\_base}^{table\_ee} \quad (3.8)$$

$$T_{table\_ee}^{c-arm\_ee} = {T_{c-arm\_base}^{table\_ee}}^{-1}\, T_{c-arm\_base}^{c-arm\_ee} \quad (3.9)$$

To validate $T_{table\_ee}^{c-arm\_ee}$ pose calculated using DH parameters, 1000 random samples of input joint configurations were generated. For these random samples, $T_{table\_ee}^{c-arm\_ee}$ was calculated using DH approach and "transform sensor" from the Simscape model. The "transform sensor" refers specifically to the Transform Sensor block which is used to measure the relative pose between two reference frames in a rigid-body system. The block computes the relative homogeneous transformation providing translational position and rotational orientation of the operating table end-effector frame with respect to its base frame. The output quantities include Cartesian position components and orientation expressed as rotation matrices or equivalent parameterizations, consistent with rigid-body kinematics. The output poses from these approaches matched exactly with zero rotation and translation errors (error calculation equations: (3.3) – (3.6)).

The reported zero numerical error between the DH-based forward kinematics model and the Simscape transform sensor output should be interpreted within the context and limitations of simulation-based validation. Both approaches operate on identical mathematical representations of rigid-body transformations and share the same numerical precision, coordinate conventions, and idealized assumptions. As a result, agreement between the two methods confirms the internal consistency and correctness of the kinematic formulation rather than representing a validation against physical hardware behavior. It is important to note that this comparison does not account for real-world effects such as mechanical tolerances, joint backlash, structural compliance, sensor noise, or calibration errors which would be present in a physical system. Consequently, the zero-error result should be understood as verification of the analytical kinematic model under idealized conditions rather than as empirical validation of the physical system. Nevertheless, such simulation-based cross-verification is a standard and necessary

step in robotic modeling to ensure correctness of the forward kinematics prior to incorporating dynamics, control, or experimental uncertainties. Future validation using hardware-in-the-loop experiments or measurements from physical table encoders and external tracking systems would be required to quantify the impact of non-idealities and to assess absolute accuracy in a clinical environment. However, for the purposes of this work namely workspace analysis, inverse kinematics, and control design the simulation-based verification provides sufficient confidence in the correctness of the operating table kinematic model.

3.2.2 Collision Detection

We acknowledge that the C-arm and operating table could result in collision for some joint configurations. Even though the FK model outputs a collision pose, this is not achievable in the real clinical setting during minimally invasive surgery.

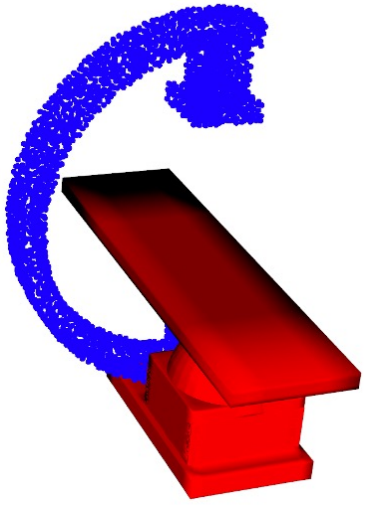

Figure 3.9: Collision detection setup.

To detect collision between C-arm and operating table, 3D objects (mesh and point cloud) were generated using Blender software (Blender 3.5.1) [132], and transformations obtained from DH parameters were applied to these 3D objects to move them in 3D space according to the input joint values. In our setup, only the C-shaped joint has reachability to collide with the operating table. For this reason, in the 3D objects the C-arm device is represented with only a C-shaped joint for collision detection purposes (Figure 3.9).
The operating table was designed using 3D watertight meshes and the C-shaped joint with point cloud (group of 3D points). For the input joint values, if any 3D points (C-arm) are present inside or on the surface of these watertight meshes (table), that pose was considered as collision [133]. A few collision poses are presented as examples in Figure 3.10.

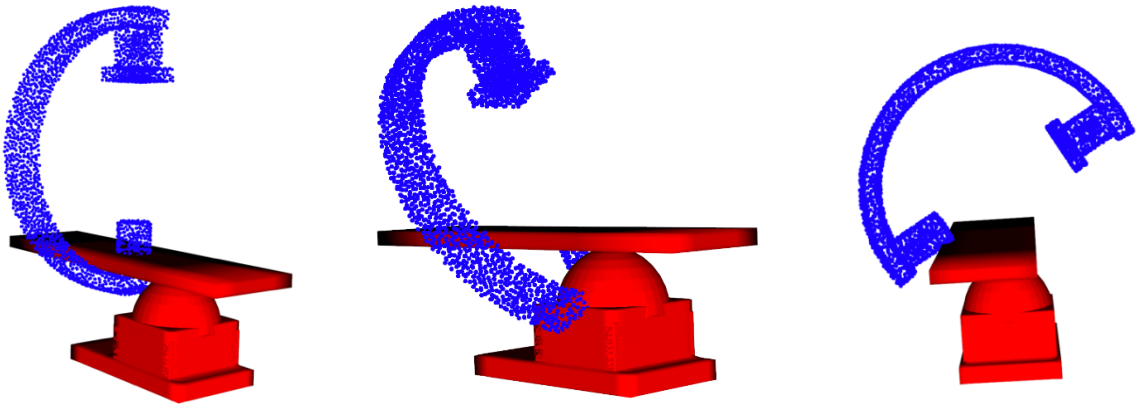

(a) (b) (c)

Figure 3.10: Sample collision poses. (a) C-arm vertical joint = 0.3 m, while the other joints were at their initial pose values; (b) C-arm tilt joint = -30°, while the other joints were at their initial pose values; (c) C-arm orbital joint = 60° and table transverse joint =0.1 m, while the other joints were at their initial pose values.

3.2.3 Surgical Workspace Analysis

The C-arm's pose w.r.t operating table ($T_{table\_ee}^{c-arm\_ee}$) was calculated using DH parameters for randomly generated joint configurations. Based on the collision detection and pose information, the combined workspace of C-arm and operating table for varying DoF setups were calculated.

The algorithm developed (using python 3.10) to calculate workspace volume of an n DoF C-arm and table is as follows:

- Generate 100,000 random joint values for n joints and the pose ($T_{table\_ee}^{c-arm\_ee}$) for these samples using DH parameters.
- Set a joint's value to its left extreme value, then generate 10,000 samples of joint values and poses ($T_{table\_ee}^{c-arm\_ee}$) by randomly selecting values for other joint values.
- Repeat step 2 for remaining joints.
- Repeat step 2 and step 3 by using right extreme joint values (10,000 samples per joint). In total, $100{,}000 + (2 \times n \times 10{,}000)$ poses were generated.
- Find collision occurrence for each sample and categorize them into "collision" or "collision-free" categories.
- Find minimum and maximum values of pose translations for each coordinate axis ($t_x^{min}, t_y^{min}, t_z^{min}, t_x^{max}, t_y^{max}, t_z^{max}$).
- Divide poses in 3D space into $5cm \times 5cm \times 5cm$ boxes using minimum and maximum values from step 6.

- Assign each box from the above step to a category. Categories: a) collision-free: all poses are without collision; (b) mixed collision: contains both "collision" and "collision-free" poses; (c) collision: all poses are "collision"; (d) empty: no samples in the box.
- Calculate total possible number of boxes, number of collision free, mixed collision, empty, and collision boxes.

The C-arm and operating table workspace was calculated for typical clinical interventional imaging configurations [134]. In this study, table rotational joints were not used and configured to zero value (i.e. patient would roll off the table). C-arm joint values to achieve these clinical interventional angles are presented in Table 3.9.

Table 3.9: Typical clinical Interventional Imaging Configurations [18]. Left Anterior Oblique (LAO), Right anterior oblique (RAO), Cranial (CRA), Caudal (CAU)

Projection	LAO/RAO	CAU/CRA	Our Setup (with no table rotation)	
			C-arm Orbital	C-arm Tilt
Posterior-Anterior (PA)	$LAO = 0°$	$CRA = 0°$	0°	0°
Anterior-Posterior (AP)	$RAO = 180°$	$CRA = 0°$	0°	180°
Vascular 1 (V1)	$RAO = 30°$	$CRA = 30°$	−30°	−30°
Vascular 2 (V2)	$LAO = 45°$	$CAU = 25°$	45°	25°
Vertebroplasty (Ver)	$RAO = 35°$	$CRA = 0°$	−35°	0°
Lateral (Lat)	$RAO = 90°$	$CRA = 0°$	−90°	0°

For each clinical interventional configuration, surgical workspace was calculated for different setups by varying DOF (Table 3.10). Random poses were generated based on number of movable joints. For example, setup 1 has six C-arm joints (6 DOF), and for each clinical interventional configuration C-arm tilt and orbital are constant and has four movable joints. For each setup, a) 100,000 random input movable joints configurations were generated; b) each movable joint configured to its left extreme value and 10,000 random joint configurations were generated for other movable joints; c) each movable joint configured to its right extreme value and 10,000 random joint configurations were generated for other movable joints. Therefore, for setup 1 with four movable joints, a total of $100{,}000 + (2 \times n \times 10{,}000)$ i.e., 180,000 (here $n = 4$) poses were generated.

Table 3.10: C-arm and operating table Setups with Varying DOF.

Setup	DoF	Joints (C-arm orbital and tilt joints are fixed)	No. of randomly generated poses for each interventional configuration
1	3	C-arm 5DOF joints (Lateral joint excluded)	160,000
2	4	C-arm joints	180,000
3	5	C-arm joints, table transverse joint	200,000
4	6	C-arm joints, table transverse and vertical joints	220,000
5	7	C-arm joints, table transverse, vertical and horizontal joints	240,000
6	3	Table transverse, vertical and horizontal joints	160,000

Table 4.2 of Chapter 4 shows workspace range and volume results obtained using the above algorithm for typical clinical interventional configurations, and multiple setups (varying DOF) for each interventional configuration. Reachability volume (i.e., collision-free and mixed-collison boxes) for a setup $'s'$ w.r.t its workspace, setup#5's workspace, and setup#5's reachable volume were calculated using equations (3.10), (3.11), and (3.12) respectively. Each setup's reachable volume was compared with setup#5's workspace as it has the largest workspace volume. In these calculations, empty boxes were ignored because no poses present in those workspace boxes. $Reachability^{s}_{ws}$ shows percentage of workspace reachable without joint collision, $Reachability^{s}_{setup\#5\_ws}$ is reachable workspace compared to the setup#5's workspace, and $Reachability^{s}_{setup\#5\_reachability}$ is setup's reachability compared to setup#5's reachability volume. Reachability for different clinical interventional configurations are presented in Table 4.1 of Chapter 4.

$$Reachability^{s}_{ws} = \frac{collision\_free^{s} + mixed\_collision^{s}}{collision\_free^{s} + mixed\_collision^{s} + collision^{s}} \times 100 \quad (3.10)$$

$$Reachability^{s}_{setup\#5\_ws} = \frac{collision\_free^{s} + mixed\_collision^{s}}{collision\_free^{setup\#5} + mixed\_collision^{setup\#5} + collision^{setup\#5}} \times 100 \quad (3.11)$$

$$Reachability^{s}_{setup\#5\_reachability} = \frac{collision\_free^{s} + mixed\_collision^{s}}{collision\_free^{setup\#5} + mixed\_collision^{setup\#5}} \times 100 \quad (3.12)$$

3.2.4 Inverse Kinematics

Inverse Kinematics methods are used to find the joint values for an input target end-effector pose. The same target pose could be achieved for different joint configurations. Therefore, IK could have multiple correct

outputs, it is one-too-many solutions. In this thesis, first random collision-free target poses were generated by sampling across the C-arm and operating table combined workspace (setup 5 with 7 DOF). Second, L-BFGS-B [135], a numerical iterative minimization algorithm was used to calculate the joint values to achieve the target poses. Position and rotation errors compared to the target poses, and the amount of collision-free output configurations were analyzed.

I. Target Poses Generation

The highest DOF setup #5 presented in section 3.2.3 has the largest workspace. This setup was used as a reference for generating the target poses. Then the reachability of target poses was evaluated for varying DOF setups. From the setup #5's workspace, a maximum of 10 random collision-free poses were selected from each collision-free and mixed-collision $5\ cm\ \times 5\ cm\ \times 5\ cm$ boxes. The total number of target poses selected for different interventional configurations is presented in Table 4.3 Chapter 4.

II. Numerical Iterative Ik

To solve IK using a numerical iterative approach, an error equation with joint values as variables was created. This equation minimized w.r.t joint values using L-BFGS-B iterative method within the joint limits. For given joint values, end-effector pose transformation matrix was calculated using equation (3.9). This transformation matrix was converted to translations $\widehat{t_x}, \widehat{t_y}, \widehat{t_z}$ and Euler rotations $\widehat{r_x}, \widehat{r_y}, \widehat{r_z}$ along each axis. An error equation ($\mathrm{Err}_{\mathrm{minimize}}$) with sum of translation and rotation Euclidean norm errors was minimized to calculate the joint values to reach the target pose (translations: t_x, t_y, t_z; rotations: r_x, r_y, r_z).

A numerical iteration algorithm requires a starting point and stopping criteria. These details are presented in the below steps.

- Select random initial values for optimizing joints and configure remaining joints to their initial pose (section 3.2.1-II-A).
- Minimize error equation ($\mathrm{Err}_{\mathrm{minimize}}$, see equations (3.13) – (3.15) iteratively using L-BFGS-B algorithm with random joint values from step 1 as initial guess. Iterations stopping criteria: maximum iterations = 1000 or error tolerance = 1e-9.

$$Trans_{err} = \sqrt[2]{\begin{matrix}(\widehat{t_x} - t_x)^2 + \\ \left(\widehat{t_y} - t_y\right)^2 + \\ (\widehat{t_z} - t_z)^2\end{matrix}} \qquad (3.13)$$

$$Rot_{err} = \sqrt[2]{\begin{matrix}min(|\widehat{r_x} - r_x|,\ 360 - |\widehat{r_x} - r_x|)^2 + \\ min(|\widehat{r_y} - r_y|,\ 360 - |\widehat{r_y} - r_y|)^2 + \\ min(|\widehat{r_z} - r_z|,\ 360 - |\widehat{r_z} - r_z|)^2\end{matrix}} \qquad (3.14)$$

$$Err_{minimize} = \|Trans_{err}\|^2 + \lambda \|Rot_{err}\|^2 \qquad (3.15)$$

where λ is scaling coefficient and unit is $m^2/degree^2$.

- Check whether there is collision for the output joint configuration using forward kinematics (section 3.2.2).
- If output configuration has collision, repeat process by going back to step 1. Stopping criteria: maximum of 100 rounds with random initial guesses.

The collision-free results with absolute translation errors (3.16) less than millimeter and absolute Euler rotation errors less than degree (3.17) are provided in Table 4.4 of Chapter 4. Where $\widehat{t_i}$ is output and $\mathrm{t_i}$ is target translation value along the i^{th} axis. $\widehat{r_x}$ represents the output rotation along x-axis and $\mathrm{r_x}$ is target rotation. In Table 4.4 of Chapter 4., rotation errors around x-axis alone were presented because in our setups two out of three rotational joints were fixed based on clinical interventional configurations. Therefore, there are no rotational errors along y-axis and z-axis. In our setup, the C-arm's rotational wigwag joint contributed to rotations around the x-axis.

$$\left|T^{err}_{i\in\{x,y,z\}}\right| = |\widehat{t_i} - t_i| \quad (3.16)$$

$$|R^{err}_x| = min(|\widehat{r_x} - r_x|, 360 - |\widehat{r_x} - r_x|) \quad (3.17)$$

3.3 Methodology for Contribution 2: Motion Model

3.3.1 Trajectory Planning

The motion trajectory of the Multi-DoF C-arm system was implemented within a collision-free workspace to determine optimal motion paths that ensure smooth transitions, precise positioning, and adherence to kinematic constraints. To achieve this, four advanced trajectory planning methods - Trapezoidal Velocity Profile, Polynomial (Cubic), Minimum Jerk Polynomial, and Minimum Snap Polynomial Trajectories - were employed and evaluated for their impact on positional accuracy, trajectory smoothness, and system adaptability. Each trajectory was generated by defining the starting point or initial time instances (t_0), intermediate waypoints, and the endpoint or final time instances (t_f)for clinically relevant imaging paths associated with the six trials.

The Trapezoidal Velocity Profile [136] trajectory generates a motion profile consisting of three distinct phases: acceleration, constant velocity, and deceleration. It is designed to balance simplicity with smooth motion, particularly for applications requiring fast and efficient movements. The trajectory is mathematically defined as (3.18),

$$q_t = \begin{cases} q_0 + \frac{v_v}{2T_a}(t - t_0)^2, & t_0 \le t < t_0 + T_a (Acceleration\ Phase) \\ q_0 + v_v\left(t - t_0 - \frac{T_a}{2}\right), & t_0 + T_a \le t < t_f - T_a (Constant\ Velocity\ Phase) \\ q_f - \frac{v_v}{2T_a}\left(t_f - t\right)^2, & t_f - T_a \le t \le t_f (Decleration\ Phase) \end{cases} \quad (3.18)$$

where v_v is the constant velocity and T_a is the duration of acceleration phase.

The Polynomial (Cubic) trajectory ensures smooth transitions by defining position and velocity at the initial and final times (i.e. q_0, q_f, v_0 and $v_f$respectively), satisfying four conditions. To meet these requirements, the Polynomial trajectory employs a cubic or third-degree polynomial [136]. The cubic polynomial trajectory can be mathematically stated as in (3.19),

$$q(t) = a_0 + a_1(t - t_0) + a_2(t - t_0)^2 + a_3(t - t_0)^3, \ t_0 \le t \le t_f \quad (3.19)$$

The coefficients are computed by satisfying boundary conditions for position, velocity, and acceleration at the start and end times.

The Minimum Jerk Polynomial trajectory further enhances smoothness by considering continuous acceleration beside position and velocity and satisfying six conditions [136]. As there are six boundary conditions, therefore this trajectory applies fifth degree polynomial as expressed in (3.20),

$$q(t) = a_0 + a_1(t - t_0) + a_2(t - t_0)^2 + a_3(t - t_0)^3 + a_4(t - t_0)^4 + a_5(t - t_0)^5 \quad (3.20)$$

The Minimum Snap Polynomial trajectory [136] further enhances smoothness by minimizing snap that is the fourth derivative of position. As there are eight boundary conditions, therefore this trajectory uses seventh degree polynomial as in (3.21),

$$q(t) = a_0 + a_1(t - t_0) + a_2(t - t_0)^2 + a_3(t - t_0)^3 + a_4(t - t_0)^4 + a_5(t - t_0)^5 + a_6(t - t_0)^6 + a_7(t - t_0)^7 \quad (3.21)$$

3.3.2 Joint Space Motion Model

The Lagrangian method is employed in this study to derive the dynamic equations of motion for the Multi-DoF C-arm System. This method is based on the system's energy properties and provides a systematic framework for modelling complex multi-degree-of-freedom systems. The Lagrange formulation is particularly advantageous for systems with coupled motions and non-linear dynamics, as it reduces the need to directly analyze individual forces and torques. Using the Lagrange formulation, the equations of motion can be systematically derived without being dependent on a specific reference coordinate frame. By selecting a set of variables λ_i, i=1,2,….,n known as generalized coordinates, the configuration of an n-degree-of-mobility manipulator can be effectively described. These generalized coordinates define the positions of the system's links. The Lagrangian of the mechanical system [137] is then expressed as a

function of these coordinates, incorporating both the kinetic and potential energy of the system as expressed in (3.22) as follows:

$$\mathcal{L} = \mathcal{T} - \mathcal{U} \qquad (3.22)$$

where $\mathcal{T}$and $\mathcal{U}$ are the total kinetic energy and potential energy of the system correspondingly. The Lagrange's equations are expressed in (3.23) as follows:

$$\frac{d}{dt}\frac{\partial \mathcal{L}}{\partial \dot{\lambda}_i} - \frac{\partial \mathcal{L}}{\partial \lambda_i} = \xi_i \quad i = 1, 2, \ldots, n \qquad (3.23)$$

where ξ_i is the generalized force associated with the generalized coordinate λ_i. For a manipulator with an open kinematic chain, the generalized coordinates are simply the vector of joint variables as illustrated in (3.24) below:

$$\begin{bmatrix} \lambda_1 \\ \lambda_2 \\ \vdots \\ \lambda_n \end{bmatrix} = q \qquad (3.24)$$

The equations in define the relationship between the generalized forces acting on the manipulator and its joint positions, velocities, and accelerations. The derivative of Lagrange's equations in the compact matrix [137] represents the joint space dynamic model as depicted in (3.25) as follows:

$$M(q)a_q + C(q, \dot{q})\dot{q} + G(q) = \tau \qquad (3.25)$$

where $M(q)$ = a joint-space mass matrix based on the current robot configuration, $C(q, \dot{q})$ = Coriolis terms, a_q = desired joint acceleration, $G(q)$ = torques and forces required for all joints to maintain their positions due to gravitational weights & forces acting on the system, given the specified gravity, τ = torques applied at each joint as input variables of the dynamic model, q = joint configuration, and $\dot{q}$ = joint velocity. For a system consisting of *N* rigid-body subsystems (i.e. ranging from 5DoF to 9DoF), where each subsystem *i* is governed by its equation of motion and subject to a generalized force input *Q*, the equation can be reformulated as shown in (3.26):

$$M_i(q_i)a_{q_i} + C_i(q_i, \dot{q}_i)\dot{q}_i + G_i(q_i) = Q_i \qquad (3.26)$$

Therefore, the dynamic model of Multi-DoF C-arm system can be written as in (3.27):

$$M_i(q_i)\begin{bmatrix} a_{q_1} \\ a_{q_2} \\ \vdots \\ a_{q_N} \end{bmatrix} + C_i(q_i, \dot{q}_i)\begin{bmatrix} \dot{q}_1 \\ \dot{q}_2 \\ \vdots \\ \dot{q}_N \end{bmatrix} + G_i(q_i) = \begin{bmatrix} Q_1 \\ Q_2 \\ \vdots \\ Q_N \end{bmatrix} \qquad (3.27)$$

Fig.3.11 illustrates the Joint-Space Motion Model, which combines the standard rigid-body dynamics of the robotic system with a control law specifically designed to regulate closed-loop error dynamics. The

Joint-Space Motion Model integrates standard rigid body robot dynamics with a control law designed to enforce closed-loop error dynamics through the application of the generalized force input Q as depicted in (3.28) and (3.29):

$$\frac{d}{dt}\begin{bmatrix} q \\ \dot{q} \end{bmatrix} = f_{dyn}(q, \dot{q}, Q, F_{ext}) \qquad (3.28)$$

$$Q = g_{CTC}(\tilde{q}, \dot{\tilde{q}}, \ddot{q}_{ref}, \omega_n, \zeta) \qquad (3.29)$$

This model ensures precise tracking of desired trajectories by compensating for nonlinearities and disturbances, enabling robust and accurate control of the Multi-DoF C-arm system in joint space.

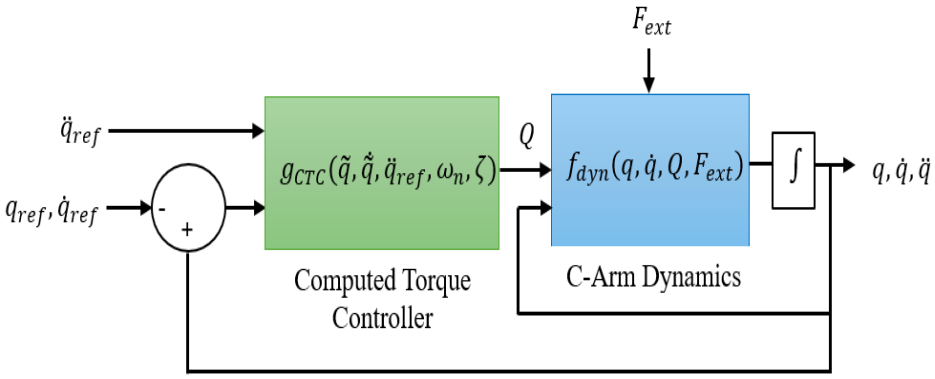

Figure 3.11: Joint-Space Motion Model.

3.3.3 Control system for Multi-DoF C-arms

The Multi-DoF C-arm system, comprising a robotic manipulator integrated with an *N*-DoF operating table, is inherently nonlinear and exhibits significant complexity due to the interactions between its multiple degrees of freedom. Accurate forecasting of dynamic parameters is particularly arduous in the context of medical applications, where variations in payloads, patient positioning, and external disturbances are common. To address these challenges, this research employs a Computed Torque Control (CTC) strategy, offering advantages over conventional Proportional-Derivative (PD) or Proportional-Integral-Derivative (PID) controllers. The CTC approach is specifically chosen to ensure overall system stability, enhance disturbance rejection capabilities and minimize or eliminate tracking errors [138], ensuring that the actual trajectory closely follows the desired trajectory. Conventional PD or PID controllers, while simple and widely used, struggle to maintain performance under varying payload conditions or uncertainties. This limitation is particularly pronounced in medical facilities, where precise and adaptive control is essential for safety and efficacy. In contrast, CTC explicitly accounts for the nonlinear dynamics of the Multi-DoF C-arm system and ensures robust performance under these challenging conditions.

The Computed Torque Control (CTC) framework integrates: (i) a feedforward compensation loop and (ii) a feedback tracking loop to achieve robust trajectory tracking. The feedforward loop linearizes and

decouples the system dynamics by compensating for the nonlinear terms in the equations of motion. It is model-based and computes the required control forces or torques to cancel the effects of inertia, Coriolis, and gravity. The feedback loop corrects deviations between the actual and desired trajectories. The primary objective of the CTC framework is to achieve a desired error dynamics and second-order error dynamics response for the i-th joint, characterized by following (3.30) and (3.31) respectively,

$$\ddot{\tilde{q}}_i = -\omega_n^2 \tilde{q}_i - 2\zeta\omega_n \dot{\tilde{q}}_i \qquad (3.30)$$

$$\tilde{q}_i = q_i - q_{i.ref} \qquad (3.31)$$

where ω_n is natural frequency in Hz and ζ is the damping ratio (unitless). This response ensures that the system exhibits stable, predictable behavior with minimal tracking error, even in the presence of uncertainties or disturbances.

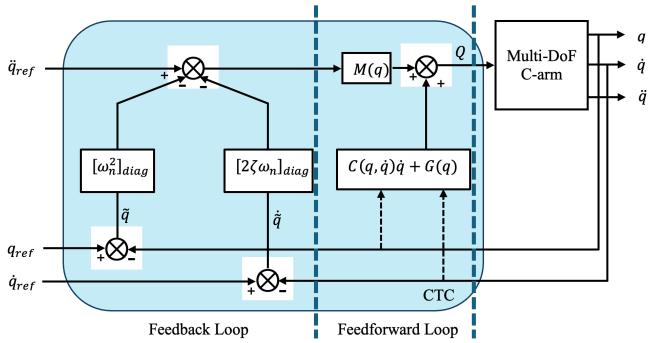

Figure 3.12: Multi-DoF C-arm control block diagram using CTC.

Figure 3.12 illustrates the joint-space control architecture of the multi-degree-of-freedom (DoF) C-arm system based on a computed-torque controller. The objective of the controller is to ensure accurate tracking of a desired joint trajectory by shaping the closed-loop dynamics of the system in joint space. To this end, a second-order reference model is employed to generate the desired joint acceleration input to the controller. Within this framework, the desired joint-space acceleration is defined as (3.32):

$$a_q = \ddot{q}_{ref} - [\omega_n^2]_{diag}\tilde{q} - [2\zeta\omega_n]_{diag}\dot{\tilde{q}} \qquad (3.32)$$

where $\ddot{q}_{ref}$ be the reference joint acceleration. Thus, the error dynamics can be calculated by (3.33):

$$\tilde{q} = q - q_{ref} \qquad (3.33)$$

where q and q_{ref} denoting the actual and reference joint position vectors.

The joint-space second-order reference acceleration law that is represented in equation (3.32) is widely used in computed-torque and impedance-based control frameworks to impose desired closed-loop dynamics. The structure of this equation enforces a critically damped or overdamped response, depending on parameter selection, and ensures asymptotic convergence of the tracking error under ideal model

compensation. Although the natural frequency ω_n and damping ratio ζ are commonly introduced as scalar parameters in single-degree-of-freedom systems, the C-arm mechanism comprises multiple joints with heterogeneous mechanical characteristics, including differences in mass, inertia, transmission mechanisms, and actuation capabilities. Consequently, each joint is modeled as an independent second-order subsystem, and both the natural frequency and damping ratio are defined on a per-joint basis. Specifically, $\omega_n \in \mathbb{R}^N$ and $\zeta \in \mathbb{R}^N$ denote vectors whose elements correspond to the natural frequency and damping ratio of each joint, respectively. The operators $[\omega_n^2]_{diag}$ and $[2\zeta\omega_n]_{diag}$ therefore represent diagonal matrices constructed from these joint-specific parameters.

This diagonal formulation enables independent tuning of the dynamic response of each joint, allowing faster convergence for joints with lower inertia and more conservative behavior for joints subject to higher loads or tighter mechanical constraints. Such flexibility is particularly important for integrated C-arm and surgical table systems, where prismatic and revolute joints exhibit substantially different dynamic properties. By embedding this joint-wise second-order behavior within the computed-torque framework, the controller achieves accurate trajectory tracking while maintaining stable and predictable closed-loop performance across the full multi-DoF system.

3.3.4 Evaluation

This section describes a comprehensive evaluation of the Multi-DoF C-arm system's performance across varying degrees of freedom (i.e. 5DoF to 9DoF), trajectory profiles, and loading conditions (normal and overweight patients). To further assess its capabilities under diverse clinical scenarios, two phases were conducted. In the first phase, three trials (Trials 1,2,3) were conducted considering two patient weight categories: normal weight and overweight. This approach allowed for an in-depth analysis of the system's adaptability and robustness under varying gravitational and inertial loads, reflecting the challenges encountered in diverse clinical scenarios. In the second phase, a final three trials (Trials 4,5,6) were conducted exclusively for the normal weight patient to focus on detailed kinematic optimization, trajectory planning, and computational efficiency under nominal conditions. This stepwise approach ensured that the evaluation not only validated the system's performance under dynamic conditions but also facilitated the fine-tuning of trajectory profiles and control algorithms for typical clinical applications. By adopting this dual-pattern methodology, the study balances the need for robustness under extreme cases with optimization for routine use, aligning the evaluation process with real-world clinical requirements.

Trials 1 to 3 featured initial points at Anterior-Posterior (AP), Lateral (LAT), and Posterior-Anterior (PA), respectively, culminating at Vertebroplasty (VER), Anterior-Posterior (AP), and Lateral (LAT). These trajectories traversed intermediate waypoints as outlined in Table 3.11. We note here that for the 5-DoF

and 6-DoF configurations, the absence of Vascular 1 (V1) as a waypoint underscored the workspace constraints inherent to these configurations, which restricted the availability of collision-free poses.

Trials 4 to 6 were intended to explore more complex trajectories, with starting points at Vascular 1 (V1), Vascular 2 (V2), and Vertebroplasty (VER), showcasing the enhanced adaptability and flexibility of higher DoF configurations.

These advanced 7DoF-9DoF configurations demonstrated superior capability in accommodating intricate imaging paths by leveraging their expanded operational workspaces and kinematic versatility. Conversely, the 5DoF and 6DoF configurations struggled to complete certain trajectories due to their constrained kinematic capabilities and limited range of motion, which impeded the system's ability to navigate more demanding paths. We conclude here by stating that for the six trials, starting points, waypoints, and endpoint trajectories were randomly assigned.

Table 3.11: Clinically Significant Trajectory Descriptions for Six Trials of the Multi-DoF C-arm System.

Trial	DoF	Starting Point	Ending Point	Waypoints
1	7,8,9	AP	VER	LAT, PA, V1, V2
	5,6	AP	VER	LAT, PA, V2
2	7,8,9	LAT	AP	PA, V1, V2, VER
	5,6	LAT	AP	PA, V2, VER
3	7,8,9	PA	LAT	V1, V2, VER, AP
	5,6	PA	LAT	V2, VER, AP
4	7,8,9	V1	PA	V2, VER, AP, LAT
5	7,8,9	V2	V1	VER, AP, LAT, PA
	5,6	V2	PA	VER, AP, LAT
6	7,8,9	VER	V2	AP, LAT, PA, V1
	5,6	VER	V2	AP, LAT, PA

3.3.5 Software & Parameter Descriptions

Evaluations were conducted in MATLAB Simulink using the Joint Spaces Motion Model, incorporating collision-free configurations derived from workspace analysis and clinically relevant imaging projections. Trapezoidal Velocity Profile, Polynomial (cubic), Minimum Jerk Polynomial, and Minimum Snap Polynomial trajecotries were applied using the *trapveltraj, cubicpolytraj, minjerkpolytraj, and*

minsnappolytraj functions from the Robotics System Toolbox™. The calculations were performed on a computer equipped with a 13th Gen Intel(R) Core (TM) i7-13700KF 3400 MHz processor and 16 GB of memory. The dataset provided joint variables corresponding to collision-free positions within the workspace, which were used to generate reference joint-space values. These joint variables represent the precise configurations required to achieve valid positions within the operational workspace, forming the foundation for trajectory planning and control. By mapping these joint variables to their corresponding positions, a dataset of reference configurations was created, which serves as the foundation for trajectory planning and control. This approach ensures that the reference trajectories derived for joint-space motion are both kinematically feasible and collision-free, aligning with the physical and operational constraints of the system. The four trajectory profiles were used to define reference joint variables, with the desired trajectories for each joint obtained using closed-loop joint-space position control.

CTC is evaluated through simulation using the dynamic model of the Multi-DoF C-arm system. For joint-space control, the vector of reference joint angles or positions or configurations, q_{ref} are specified via trajectory; the controller tracks the reference joint configuration q_{ref} and returns the actual configuration q. The performances of the controller are evaluated via a function. The function is calculated using the error between the desired reference trajectory and the obtained angle or position at each joint. The optimized parameters of the controllers that characterize the desired response defined for each joint, are summarized in Table 3.12.

Table 3.12: The optimized parameters of the controllers.

Parameter	**Symbol**	**Value**
Natural frequency	ω_n	0.6366 (kHz)
damping ratio	ζ	1 (unitless)

The natural frequency of the Multi-DoF C-arm system was chosen to be 0.6366 kHz, considering the system's dynamic characteristics and the requirements for precise and stable operation during clinical applications. The selection of this value aligns with principles outlined in [139], where Blind-Kriging surrogate modelling was applied to analyze and predict the natural frequencies of industrial robots. The research demonstrates the importance of modal analysis in optimizing robotic systems to ensure structural stability and vibration minimization under operational conditions. By leveraging insights from [139], the chosen natural frequency for the Multi DoF C-arm system reflects a balance between maintaining dynamic response efficiency and avoiding resonance effects during operation. The value of 0.6366 kHz was specifically selected to ensure minimization of oscillatory behaviors during high-precision movements in clinical intervention and alignment with typical natural frequencies of comparable robotic systems analyzed

in [139]. This reference provides a robust rationale for the systematic consideration of natural frequencies in robotic system design, further validating the selection of 0.6366 kHz as a suitable natural frequency for the C-arm. While the damping ratio, $\zeta = 1$ corresponds to the theoretical condition of critical damping for an ideal second-order system, it is well understood that achieving exact critical damping in physical systems is practically infeasible. Real C-arm hardware exhibits unmodeled dynamics, actuator saturation, friction nonlinearities, structural compliance, sensor noise, and time delays all of which prevent the closed-loop system from matching the idealized reference dynamics exactly. Consequently, the value $\zeta = 1$ should be interpreted not as a precise physical realization, but as a design target for the desired closed-loop behavior. In practical applications, specifying $\zeta = 1$ within a computed-torque or impedance-based control framework defines a nominal critically damped reference model that the controller attempts to track. The actual system response typically exhibits behavior that is near critically damped, often slightly underdamped or overdamped depending on joint-specific dynamics and operating conditions. This approach is common in robotic control, where reference models are intentionally chosen to represent ideal performance envelopes rather than exact realizable dynamics. To account for real-world uncertainties, several practical measures should be adopted. First, the natural frequency ω_n should be conservatively selected to ensure that commanded accelerations remain within actuator limits, thereby preventing excitation of unmodeled high-frequency dynamics. Second, joint-specific damping ratios are required to tuned experimentally around the nominal critically damped value to achieve smooth, monotonic convergence without oscillations or excessive settling time. In practice, this results in effective damping ratios in a neighborhood of unity rather than a single exact value.

The external force applied to the controller based on weight thresholds of 95 kg for normal weight patients and 120 kg for overweight patients. These thresholds are adopted from the weight classifications discussed in [140], which analyzed the impact of obesity on outcomes surgeries and provides clinically relevant weight benchmarks for categorizing patients into normal weight and overweight groups, making it a suitable basis for determining external forces in this contribution. The external force F_{ext} was modelled as the product of the patient's effective mass m_p and gravitational acceleration, g. This force was integrated into the Computed Torque Control ensuring precise compensation for increased gravitational and inertial loads. By explicitly accounting for patient mass, the controller adapts joint torques and reference accelerations to maintain stable and accurate motion under varying load conditions, thereby improving robustness and safety during imaging procedures. While patient body shape and size also influence the spatial relationship between the C-arm and table, the patient weight was prioritized in this contribution because it directly affects global system loading, actuator effort, and joint dynamics. In contrast, body shape and anatomical variability primarily influence collision geometry, clearance margins, and reachable workspace, rather than the dominant gravitational forces acting on the system. Incorporating such geometric information represents

a natural extension of the present framework and is identified as an important direction for future work, where patient-specific anatomy could be integrated to further refine collision avoidance and workspace feasibility analysis. Two lookup table were created for the two phases of evaluation to guide clinicians in selecting appropriate trajectories and tuning joint parameters for specific clinical tasks. The table provides: i) optimal trajectory profiles for different clinical projections and configurations, ii) joint-specific positional errors for varying DoF and patient conditions, and iii) simplified decision-making for achieving precise alignment during clinical X-ray imaging. The evaluation framework developed in this contribution provides a robust method for generating LUT that can significantly enhance pre-surgical planning and intraoperative efficiency. By simulating the motion of the C-arm system across varying configurations, trajectory profiles, and clinical projections, the system produces a comprehensive database of joint configurations and positional errors for each trajectory type. These LUT consider critical parameters such as patient weight (normal and overweight) and clinical imaging requirements to ensure realistic and clinically relevant outcomes.

In addition to increased gravitational and inertial loading, variations in patient weight also influence frictional effects within the C-arm joints and transmission elements, including bearings, gears, and linear guides. Higher patient mass increases normal forces transmitted through the patient table and supporting joints, which in turn can elevate Coulomb and viscous friction components in both revolute and prismatic joints. These effects are particularly relevant for table-mounted prismatic joints and load-bearing C-arm axes, where increased contact forces within mechanical transmissions may lead to higher resistive torques. In the present framework, friction is not modeled explicitly as a separate nonlinear term. Instead, its influence is implicitly accommodated through the computed-torque control structure and conservative parameter selection. The dynamic model used for control captures the dominant inertial and gravitational effects while residual unmodeled dynamics including friction variations, backlash, and transmission compliance are treated as bounded disturbances. By explicitly accounting for patient weight in the external force term F_{ext}, the controller compensates for the primary load-dependent effects, thereby reducing the sensitivity of the closed-loop system to secondary frictional variations.

From a control perspective, increased friction due to higher patient weight manifests primarily as a reduction in tracking performance or slower transient response rather than instability. This is mitigated using a critically damped reference model, conservative natural frequency selection, and joint-wise tuning of control gains. These measures ensure robust performance even when friction levels vary across patient conditions. In practice, the resulting behavior corresponds to near-critical damping with slightly increased steady-state control effort for overweight patient scenarios which is consistent with clinical safety requirements. Explicit friction modeling such as LuGre or Stribeck-based formulations would require joint-specific identification procedures under varying load conditions and is therefore identified as a natural

extension of this work. Incorporating load-dependent friction models represents a valuable direction for future research, particularly for further improving low-speed precision and force transparency during delicate imaging maneuvers.

Algorithm: The pseudo code for the framework

BEGIN

// STEP 1: SYSTEM MODELLING

1. Initialize the Multi-DoF C-arm system:
   - Define configurations: 5-DoF to 9-DoF
   - Include C-arm joints and surgical table joints with their respective limits.
   - Calculate DH parameters for each configuration.
2. Perform Workspace Analysis:
   - Generate 100,000 random joint values for each configuration.
   - Compute poses using DH parameters.
   - Create collision-free 3D workspace using Blender models.
   - Classify workspace into:
     a. Collision-free
     b. Mixed collision
     c. Collision
     d. Empty regions
3. Select clinically relevant projections for trajectories:
   - Define clinical projections: AP, LAT, PA, V1, V2, VER.
   - Identify collision-free projections for each configuration.

// STEP 2: TRAJECTORY PLANNING

4. Choose trajectory planning methods:
   - Trapezoidal Velocity Profile
   - Polynomial Trajectory (Cubic)
   - Minimum Jerk Polynomial Trajectory
   - Minimum Snap Polynomial Trajectory
5. Generate reference trajectories:
   - For each clinical projection (trials 1 to 6), define:
     a. Start point
     b. Waypoints
     c. End point
   - Compute joint configurations q_{ref} for each trajectory.

// STEP 3: CONTROL STRATEGY

6. Implement Computed Torque Control (CTC):
   - Define control law:
   - Set natural frequency and damping ratio.
   - Apply external force based on:
     a. Normal weight (95 kg)
     b. Overweight (120 kg)

// STEP 4: SIMULATION SETUP

7. Define simulation environment:
   - Use MATLAB Simulink for the Joint Space Motion Model.
   - Incorporate the following:
     a. Collision-free poses as input
     b. Reference trajectories for q_{ref}
     c. CTC for tracking q_{ref}
8. Simulate for each trial:
   - Trial 1–3: Normal and overweight conditions
   - Trial 4–6: Normal weight condition only
   - For each configuration (5-DoF to 9-DoF):
     a. Simulate trajectories
     b. Record joint responses and positional errors

// STEP 5: ANALYSIS

9. Analyze simulation results:
   - Evaluate positional errors (mean and standard deviation).
   - Compare trajectory smoothness for each method.
   - Assess computational efficiency.
10. Identify configuration-specific trends:
    - Highlight the effect of DoF on accuracy and adaptability.
    - Analyze performance across normal and overweight conditions.

// STEP 6: VALIDATION AND CLINICAL RELEVANCE

11. Validate findings:
    - Compare Positional errors for all trials and configurations
    - Highlight optimal configurations and trajectory methods.
    - Create Lookup table (LUT) for clinicians with recommendations for pre-surgical planning

END

3.4 Methodology for Contribution 3: Machine Learning Approach to Forward and Inverse Kinematics

3.4.1 Machine Learning Approach to Forward and Inverse Kinematics

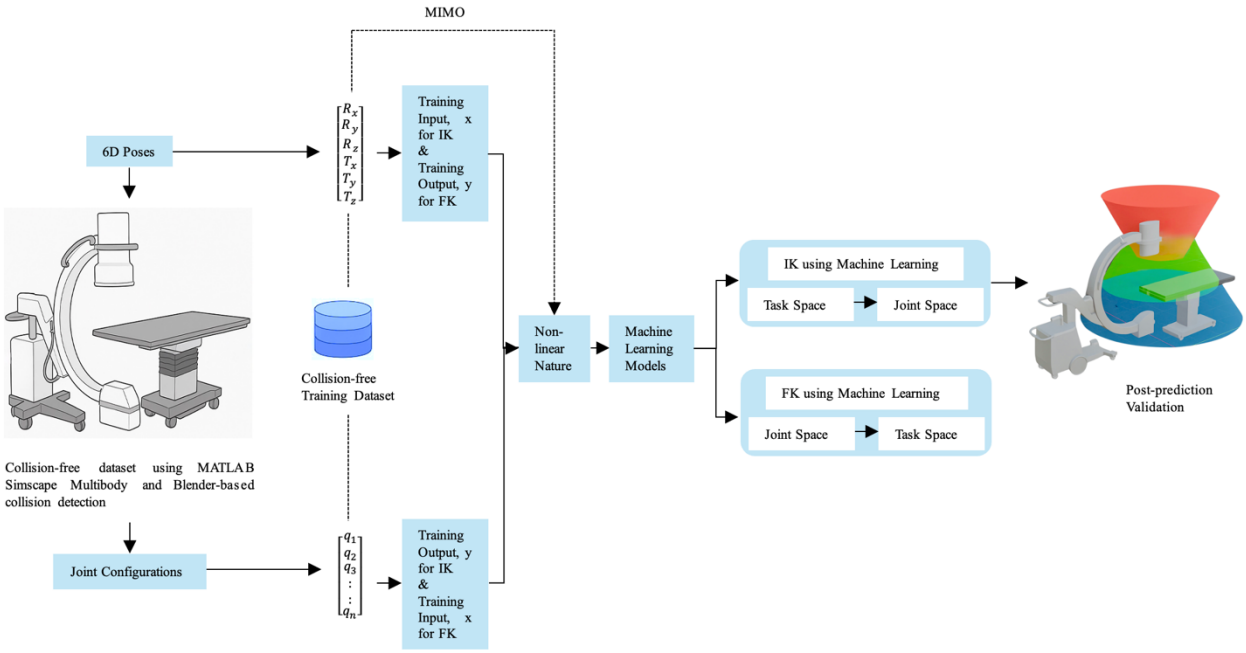

Figure 3.13: Kinematic Learning Framework.

The proposed kinematic learning framework as shown in fig. 3.13 employs a Multiple-Input, Multiple-Output (MIMO) modeling strategy to simultaneously predict high-dimensional robotic variables within the modular C-arm and surgical table system. This approach is structured into four key stages. In 1st stage, collision-free dataset generation is conducted using MATLAB Simscape Multibody and Blender-based collision detection pipelines. Datasets are created for five system configurations (ranging from 5 to 9 DoF), each comprising valid joint combinations and their corresponding 6D end-effector poses (translation and rotation). For each configuration, forward mapping pairs joint configurations as input with 6D poses as output, while inverse mapping pairs 6D poses as input with joint variables as output. In the 2nd stage, the MIMO model formulation replaces traditional single output regressors with a unified multi-output regression framework. In the forward kinematics task, the model learns a mapping from the joint vector $q \in R^n$ to a 6D pose vector $x = [R_x, R_y, R_z, T_x, T_y, T_z] \in R^6$.

Conversely, for inverse kinematics, the model takes the 6D pose as input and predicts up to 9 joint values simultaneously. This formulation captures spatial and kinematic dependencies across joints, allowing the model to learn interactions between coupled prismatic and revolute motions. In the third stage, model training and validation are performed using five supervised learning algorithms: Ridge Regression, K-

Nearest Neighbors, Random Forest, Gradient Boosting Machines, and Deep Neural Networks (DNNs). All models are configured for multi-output regression, and training is performed on a standardized 70/15/15 train-validation-test split. Hyperparameter optimization is conducted via 5-fold cross-validation to ensure generalizability. For DNNs, Principal Component Analysis (PCA) is optionally applied to improve numerical conditioning and reduce input redundancy. Finally, a comprehensive evaluation and comparative analysis is conducted using four regression metrics: MAE, MSE, RMSE, and R^2. These metrics are computed both per output and across all outputs to assess fine-grained performance and overall system accuracy. Evaluation results are visualized through joint-specific heatmaps and pose-level prediction plots enabling model-level and DoF-level insight. This structured MIMO-based learning framework not only ensures consistency across predicted joint configurations or poses but also reduces training complexity compared to isolated regressors. Its joint-aware architecture facilitates robust and interpretable kinematic learning for modular robotic systems operating in safety-critical surgical environments.

3.4.2 Collection of Collision-Free Pose Datasets

A comprehensive dataset generation pipeline was developed to support machine learning–based inverse kinematics prediction for modular C-arm systems with integrated operating table mobility. Kinematic models for five system configurations ranging from 5 to 9 degrees of freedom were constructed. These configurations included a combination of prismatic and revolute joints representing translational and rotational motions of the C-arm and translational mobility of the operating table. Each joint was constrained within experimentally validated motion limits. For every configuration, forward kinematics were computed in MATLAB to produce corresponding end-effector poses in task space represented by translation vectors (t_x, t_y, t_z) and Euler angles (r_x, r_y, r_z). To evaluate the physical feasibility of each configuration, the computed joint values and associated kinematic transforms were exported to Blender, where high-fidelity 3D mesh models of the C-arm and operating table were used to perform collision detection. In this simulation environment, a pose was classified as “colliding” if any portion of the C-arm mesh (e.g., image intensifier, gantry frame, X-ray source) intersected with the table geometry. Collision detection was automated using Blender’s physics engine and scripted logic that flagged any geometric intersections. Only configurations confirmed to be entirely collision-free were retained for downstream use. The original simulation workflow generated three types of samples: collision-prone, mixed-overlap, and collision-free. However, this contribution deliberately selects only the collision-free subset to ensure that all machine learning models are trained on physically valid data, reducing the risk of unsafe pose prediction at deployment.

The final datasets encompass five system configurations spanning from a Conventional C-arm (5DoF) to an Enhanced C-arm (6DoF) with additional lateral translation, and integrated table systems offering 7DoF, 8DoF, and 9DoF motion. The datasets comprise 131,229 poses for the 9DoF system (C-arm combined with

vertical, longitudinal, and transverse table translations), 96,257 for the 8DoF system (excluding longitudinal movement), 41,173 for the 7DoF system (only transverse table translation), 20,000 for the Enhanced 6DoF C-arm, and 7,209 poses for the Conventional 5DoF C-arm. The total sample sizes of collision-free pose datasets are summarized in Table 3.13.

Table 3.13: The total sample sizes of collision-free pose datasets generated for C-arm and integrated operating table configurations across varying degrees of freedom.

Configuration	Total Degrees of Freedom	Number of Collision-free Poses
C-arm + Table Vertical, Longitudinal & Transverse	9DoF	131229
C-arm + Table Vertical & Transverse	8DoF	96257
C-arm + Table Transverse	7DoF	41173
Enhanced C-arm (with added lateral motion)	6DoF	20000
Conventional C-arm (standard model)	5DoF	7209

3.4.3 Dataset Structure for Machine Learning-Based Inverse Kinematics

The dataset used for machine learning-based inverse kinematics comprises sequentially indexed entries (SI. No.), with each entry containing the active joint configuration and its corresponding end-effector pose. These poses calculated using forward kinematics are expressed as 6D transformations consisting of Euler angles (R_x, R_z, R_z) for orientation and Cartesian translations (T_x, T_y, T_z) for position. This representation captures the full spatial configuration of the C-arm imaging system in relation to the surgical field. Table 3.14 presents the complete dataset structure for the 9DoF configuration, which includes six degrees of freedom from the C-arm (CL, CV, CW, CH, CT, CO) and three translational degrees of freedom from the integrated mobile operating table (TV, TL, TT). This dataset is used within the contribution to illustrate the full joint-to-pose mapping and serves as the primary benchmark for model training and evaluation. For brevity and clarity, datasets corresponding to the 8DoF, 7DoF, enhanced 6DoF, and conventional 5DoF configurations are not included directly in the thesis. However, these datasets follow the same structural format as Table 3.14, with appropriate exclusion of joints (e.g., TL, TT, CL) based on the respective DoF constraints. These additional datasets, along with the 9DoF dataset are publicly available in a dedicated GitHub repository [141].

Table 3.14: Dataset of a 9DoF C-arm and integrated operating table.

Sl. No.	CL	CV	CW	CH	CT	CO	TV	TL	TT	R_x	R_y	R_z	T_x	T_y	T_z
1	9	1	7	1	180	0	35	70	-11	-83	0.00	-90	-3	-18.63	-25.60
2	11	2	6	0	180	0	36	54	-12	-84	0.00	-90	-3	-20.32	-14.32
3	-12	1	0	0	180	0	34	60	-13	-90	0.00	-90	-2	-20.50	-13.00
.	.	.	.	.	.	.	.	.	.	.	.	.	.	.	.
.	.	.	.	.	.	.	.	.	.	.	.	.	.	.	.
.	.	.	.	.	.	.	.	.	.	.	.	.	.	.	.
131227	-49	46	3	10	0	-35	16	6	0	87.54	1.72	124.96	61	2.28	86.37
131228	-41	30	10	9	0	-35	0	10	3	81.78	5.72	124.59	61	2.08	93.61
131229	-42	30	7	6	0	-35	0	5	5	84.26	4.01	124.80	61	2.34	91.01

3.4.4 Nonlinearity, Redundancy, and Singularity Handling

The integrated C-arm and operating table system exhibits a highly nonlinear and redundant kinematic structure because translational (prismatic) and rotational (revolute) joints are coupled through sequential trigonometric transformations. This results in a non-linear mapping between joint variables, and the end-effector pose, where multiple joint configurations can realize identical Cartesian positions and orientations.

All singularity analyses and redundancy-resolution strategies were established in earlier works by Jaheen et al. [157], [158]. During dataset generation for this study, singularity-prone and collision-inducing configurations were excluded, ensuring that the training data represent only mechanically feasible, continuous trajectories. The inverse-kinematics stage employed a BFGS gradient-projection algorithm to select the configuration closest to the preceding valid state, thereby maintaining continuity across the redundant workspace.

For rotational representation, the end-effector attitude was initially parameterized in unit-quaternion form and subsequently transformed into XYZ Euler angles following a consistent roll–pitch–yaw convention. A wrap-angle normalization within the range [–180°, 180°] was applied to preclude discontinuities at angular boundaries, thus maintaining orientation coherence throughout both data preprocessing and model evaluation. Consequently, the datasets utilized for learning realistically encapsulate the intrinsic nonlinear behavior of the C-arm and operating table mechanism while remaining singularity-free, dynamically coherent, and kinematically consistent across the entire workspace.

3.4.5 Machine-Learning Framework

To approximate the highly nonlinear and redundant mapping between joint-space variables and end-effector poses of the integrated C-arm-table system, a supervised machine-learning (ML) framework was developed and trained on the singularity-free, collision-free datasets generated from the preceding inverse-kinematics pipeline. The objective was to construct predictive models capable of learning the deterministic, continuous relationship between the joint configuration vector and the corresponding Cartesian pose representation. Multiple regression architectures were investigated to capture this mapping at varying levels of model complexity, including Ridge Regression, K-Nearest Neighbors (KNN), Random Forest (RF), Gradient Boosting Regressor (GBR), and Deep Neural Networks (DNN). Each model was independently optimized through cross-validation to minimize mean-squared-error loss, while preventing overfitting through regularization and data normalization.

The ML framework treats each pose component: three rotational (R_x, R_z, R_z)) and three translational (T_x, T_y, T_z) as a separate regression head, ensuring modularity and allowing comparative analysis across algorithms. Training and evaluation were conducted on stratified subsets to preserve workspace diversity, and performance metrics, including Mean Absolute Error (MAE), Root Mean Square Error (RMSE), and Coefficient of Determination (R^2), were computed for quantitative benchmarking. By leveraging these complementary learning paradigms, the framework establishes a data-driven surrogate capable of accurately reproducing the nonlinear kinematic behavior of the C-arm with surgical table system, thereby enabling efficient prediction and analysis across complex surgical configurations.

3.4.6 Machine Learning Model Architectures

This research assesses five supervised machine learning models to predict collision-free C-arm end-effector pose from joint configurations inputs and vice versa. The selected models span linear, instance-based, ensemble-based, and deep learning paradigms, enabling a comprehensive comparison of predictive performance under varying degrees of model complexity. The architectural details and configuration strategies for each model are described in the following subsections.

I. Ridge Regression

Ridge Regression serves as a baseline linear model that incorporates L2 regularization to mitigate overfitting and enhance numerical stability. Unlike standard Linear Regression, which may suffer from high variance in the presence of multicollinearity or high-dimensional feature spaces, Ridge Regression penalizes large coefficient values, thus reducing model sensitivity to noise and correlated input features. The model minimizes the residual sum of squares while applying a penalty on the magnitude of regression coefficients. The regularization strength α, a critical hyperparameter controlling the degree of shrinkage, was optimized using 5-fold cross-validation. This regularization is particularly beneficial in scenarios where

joint variables (e.g., multiple joint movements of C-arm and table) exhibit interdependence, as it prevents overfitting and improves generalization to unseen poses. Ridge Regression was selected over standard Linear Regression for its improved robustness and ability to handle ill-conditioned or collinear data, both of which are common in robotic systems involving multiple coupled degrees of freedom. Its efficiency, simplicity, and interpretability make it a suitable candidate for benchmarking against more complex models.

II. Gradient Boosting Machines

Gradient Boosting Machine (GBM) builds a sequence of weak learners typically shallow decision trees where each new learner attempts to correct the residual errors of the ensemble's cumulative prediction. Unlike Random Forests, GBM relies on additive model building and is sensitive to overfitting, necessitating careful regularization. Core hyperparameter, the learning rate all of which has been optimized through cross-validation. GBM is particularly adept at capturing complex, non-linear relationships in structured datasets, making it well-suited for learning the mapping between high-dimensional pose inputs and corresponding joint configurations.

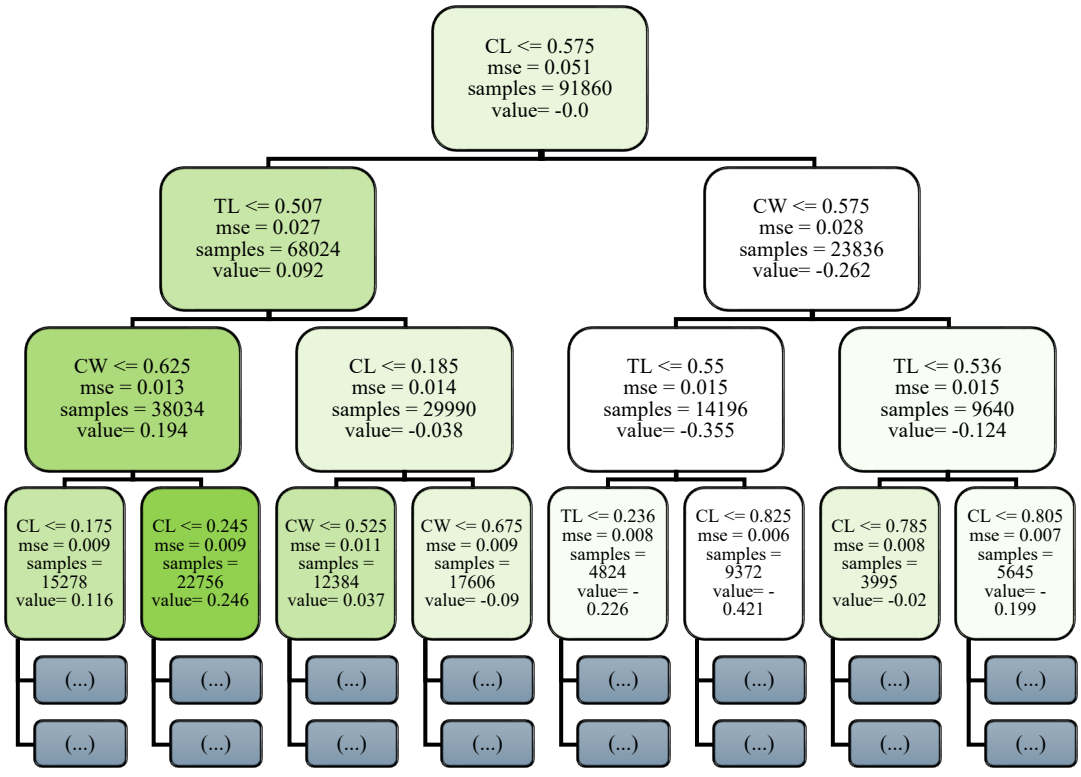

Figure 3.14: Visualization of the initial decision tree (Stage 0) in the Gradient Boosting Machine (GBM) model for C-arm pose. prediction.

Fig 3.14. presents the initial decision tree (Stage 0) in the Gradient Boosting Machine ensemble, offering critical insight into the model's foundational learning dynamics. GBM constructs an additive sequence of weak learners typically decision trees each aimed at correcting the residual errors of its predecessors. This first tree is particularly informative, as it reveals how the model initiates the mapping between joint-space input features and predicted C-arm pose components. Internal nodes within the tree represent binary decision rules based on input features such as CW, TL etc., with each node applying a threshold criterion to partition the dataset. Depending on whether an input value satisfies the threshold condition, the instance is routed to the left or right child node. Terminal nodes, or leaves, output scalar prediction values that contribute incrementally to the model's final prediction through boosting. While the complete GBM comprises hundreds of such trees, this single-tree visualization facilitates interpretability by highlighting early feature selection, decision thresholds, and hierarchical rule formation attributes that are vital for clinical transparency and trust in automated pose estimation systems.

III. K-Nearest Neighbors

K-Nearest Neighbors is a non-parametric, instance-based learning algorithm that infers the output of a test sample by aggregating the labels of its k closest neighbors in the feature space. The model operates under the assumption that similar inputs yield similar outputs. The optimal value of k, along with the choice of distance metric and weighting scheme, has been selected through cross-validation. To improve robustness, a distance-weighted voting mechanism is employed, allowing closer neighbors to contribute more significantly to the final prediction. KNN provides a simple yet powerful baseline, especially in data-rich environments.

IV. Random Forest

Random Forest (RF) is an ensemble learning algorithm that constructs multiple decision trees using bootstrap aggregation (bagging). Each tree is trained on a randomly sampled subset of the training data and a random subset of features, promoting model diversity. Predictions are made by averaging the outputs across all trees, reducing variance and improving generalization. Key hyperparameter, the number of trees (estimators) has been tuned using cross-validation. This model is particularly effective in capturing non-linear dependencies and handling feature interactions without requiring extensive preprocessing.

To enhance model interpretability, Fig 3.15. illustrates a truncated view of the first decision tree from the trained Random Forest model. The depth is limited to three levels to maintain readability. The tree shows how joint-space features (e.g., C-arm tilt, table transverse motion) are used to partition the data, with each decision node reflecting a threshold-based rule and each leaf node indicating a predicted output region.

The tree illustrates the hierarchical decision structure used to predict individual components of the C-arm pose based on joint-space input features. Nodes are split based on thresholds of joint variables such as C-

arm tilt, wigwag, or table translation, with leaf nodes representing predicted output values. Each node displays the decision rule, number of samples, and mean squared error at that node. The visualization offers interpretability into how the ensemble model learns non-linear, high-dimensional relationships in the joint-to-pose mapping task.

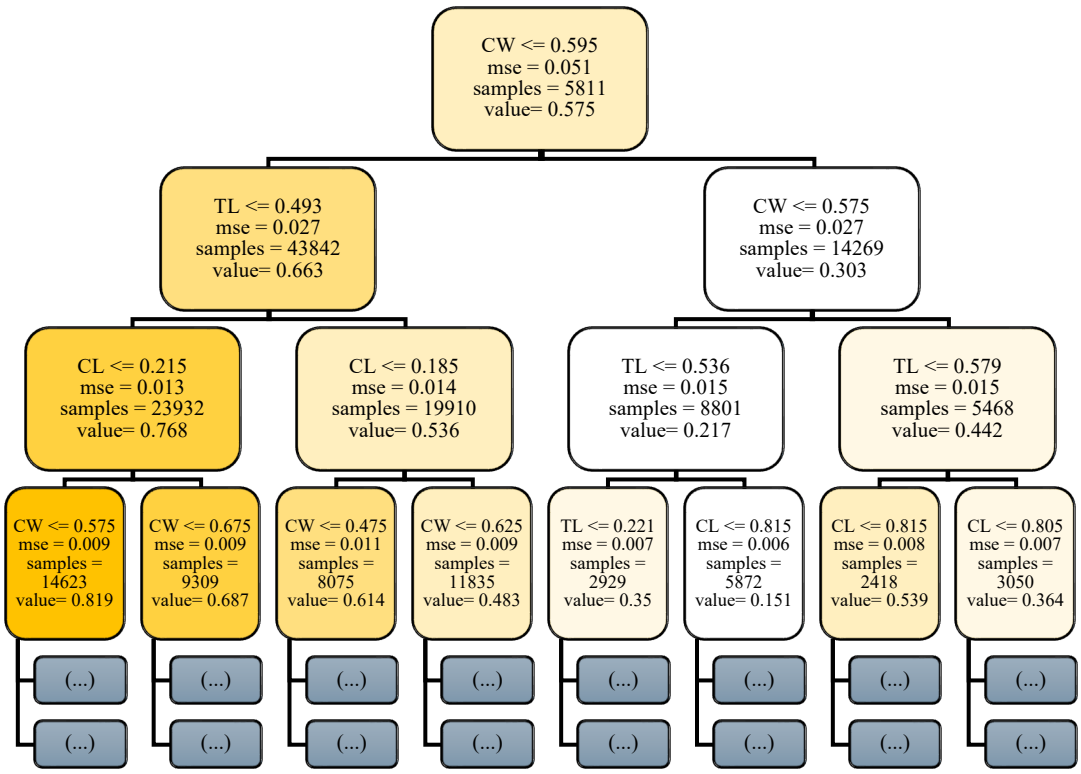

Figure 3.15: Visualization of the first decision tree (depth truncated to 3) from the trained Random Forest model.

V. Deep Neural Network

The DNN was explored in three progressively optimized configurations to evaluate its effectiveness in learning non-linear mappings between pose parameters and joint configurations. Each architecture was implemented as a feedforward network composed of fully connected layers and Rectified Linear Unit activation functions, with a six-neuron output layer corresponding to the 6D pose vector (R_x, R_y, R_z, T_x, T_y, T_z).

The initial DNN model adopted a lightweight architecture with three hidden layers of 128, 64, and 32 neurons, respectively, followed by the output layer. Although this configuration offered computational efficiency and acceptable baseline performance, it exhibited limited capacity in modelling complex, high-dimensional input relationships, often leading to underfitting.

To enhance the learning capability of the network, the architecture has been expanded to include three larger hidden layers with 256, 128, and 64 neurons, respectively. This deeper configuration as shown in Fig. 3.16, significantly improved performance by enabling the network to learn hierarchical abstractions from the input data. Dropout layers with rates of 0.3 and 0.2 were inserted after the first and second hidden layers to reduce overfitting and improve generalization.

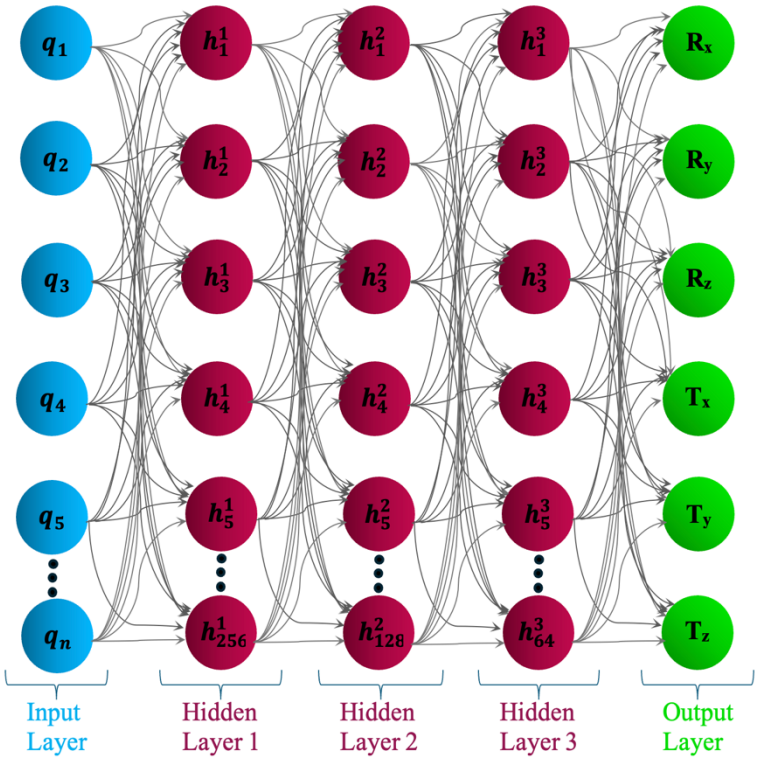

Figure 3.16: Architecture of the Deep Neural Network model with variable joint input layer and fixed 6D pose output.

The architecture of a DNN has been designed to map joint space inputs to corresponding 6D pose outputs. The input layer consists of 5 to 9 neurons, each representing a joint variable q_i, where the number of inputs depends on the modular configuration of the integrated C-arm system. The output layer comprises six neurons, each corresponding to one component of the predicted pose: R_x, R_y, R_z (rotational angles) and T_x, T_y, T_z (translational positions). These six outputs together form the full 6D pose vector that defines the end-effector configuration of the robotic system in task space.

In the final variant, the same deep architecture (256/128/64) has been retained, but the input features were first processed using PCA. PCA served as a dimensionality reduction technique to project the original feature space into a lower-dimensional, uncorrelated subspace, preserving the most significant components.

This not only improved training efficiency but also reduced model complexity and enhanced robustness against multicollinearity in the input space.

All DNN models were trained using the Adam optimizer with a learning rate of 0.001 and mean squared error (MSE) as the loss function. To stabilize convergence and prevent overfitting, early stopping with a patience of 30 epochs was applied. A dynamic learning rate schedule was also employed, reducing the learning rate by 10% if no improvement was observed in validation loss for 20 consecutive epochs.

The final DNN configuration with PCA preprocessing and a deeper architecture demonstrated superior performance in capturing the complex, non-linear relationships necessary for accurate and collision-free pose estimation in a high-dimensional modular C-arm workspace.

3.4.7 System Configuration and Training Methodology

The training and evaluation of models were performed on a high-performance workstation configured with a 13th Gen Intel® Core™ i7-13700KF processor (3.4 GHz, 16 physical cores, 24 logical threads) and 16 GB of DDR4 RAM, running a 64-bit Windows 11 operating system. The system was equipped with an NVIDIA GeForce RTX 4070 GPU featuring 12 GB GDDR6X memory and full support for CUDA and cuDNN acceleration. Model development was conducted using Python 3.12.3, with essential scientific and machine learning libraries including NumPy 1.26.4, pandas 2.2.2, scikit-learn 1.4.2, and SciPy 1.13.3. Development and experimentation were carried out within JupyterLab 4.0.11, offering an interactive environment for data preprocessing, model training, and result visualization. To ensure reproducibility and effective dependency management, all experiments were executed within a dedicated Conda virtual environment, encapsulating the necessary packages and configurations.

To optimize model performance and mitigate overfitting, hyperparameter tuning was systematically conducted for all five machine learning models using cross-validation. Each model was evaluated over a predefined, algorithm-specific hyperparameter search space. The DNN model was designed with four fully connected layers arranged sequentially, comprising 256, 128, 64, and output neurons, respectively. Dropout layers with rates of 0.3 and 0.2 were interleaved between the dense layers to provide regularization and mitigate overfitting, resulting in a total of six hidden layers in the architecture. For tree-based models such as Random Forest and Gradient Boosting Machines, key hyperparameters including the number of decision trees, and learning rate were tuned extensively. The KNN model was configured by testing different values for the number of neighbors and selecting the one that yielded the lowest validation error. As for the Ridge Regression model, regularization strength (α) was varied to determine the optimal balance between bias and variance.

To prevent overfitting and ensure generalization, the dataset was consistently partitioned into training (70%), validation (15%), and testing (15%) subsets across all five machine learning models. Early stopping

was applied during DNN training, with a patience of 30 epochs based on validation loss. In addition, a dynamic learning rate scheduler was employed, reducing the learning rate by 10% if no improvement was observed in validation loss for 20 consecutive epochs. This approach helped escape local minima and contributed to further optimization of the model, as evidenced by the consistent decline in validation error beyond epoch 120. Table 3.15 summarizes the optimized hyperparameters employed across all machine learning models and Degrees of Freedom, distinguishing between rotational (R_x, R_y, R_z) and translational (T_x, T_y, T_z) components of the 6D pose. These parameters are systematically selected using cross-validation to maximize generalization and prediction accuracy while avoiding overfitting, particularly in high-dimensional input spaces. For Ridge Regression, the regularization strength (α) controls the trade-off between model complexity and stability. A value of 1.0 is consistently assigned to rotational components in higher DoF settings (e.g., 9DoF and 8DoF) to suppress overfitting due to angular coupling. In contrast, lower values (as small as 0.01) are allocated to translational components to retain sensitivity to small positional shifts. In the case of GBM, the learning rate directly affects convergence speed and model granularity. Higher rates (0.2) are assigned to most pose components to ensure rapid learning, except for rotational components in 9DoF where lower rates (0.1) improve stability in complex angular mappings. The learning rate is tuned more conservatively in configurations with higher rotational variance. For KNN, the number of neighbors (k) significantly impacts the model's local sensitivity. A larger k (e.g., 9) is generally preferred for translational prediction to smooth noise in high DoF settings, while smaller values (3 to 5) are applied to rotational DoFs, where fine-grained prediction benefits from localized context. The RF model depends on the number of decision trees for ensemble robustness. Larger ensembles (e.g., 300 trees) are used for translational outputs across 8DoF and 9DoF systems to manage spatial complexity. For rotational components or lower DoF models, fewer trees (100–200) suffice, maintaining computational efficiency without degrading performance. The DNN architecture remains consistent across all configurations, comprising three fully connected layers (256, 128, 64 neurons) with dropout rates of 0.3 and 0.2 for regularization. The batch size is fixed at 32, and training proceeds for up to 300 epochs with early stopping based on validation loss. A learning rate scheduler reduces the learning rate by 10% after 20 stagnant epochs, facilitating convergence and avoiding local minima. This structured tuning approach ensures that each model adapts to the complexity and variability introduced by different DoF configurations, enhancing predictive accuracy and robustness across translational and rotational subspaces.

Table 3.15: Optimized Hyperparameters for Each Machine Learning Model Across multiple degrees of freedom.

Model	Hyperparameter	DoF	Rx	Ry	Rz	Tx	Ty	Tz
Linear Regression	Regularization Strength	9	1	1	1	0.01	0.01	0.1
		8	1	1	1	0.01	0.01	0.01
		7	1	1	1	0.01	0.01	0.01
		6	0.1	0.1	0.01	0.01	0.01	0.01
		5	0.01	0.1	0.01	0.01	0.01	0.01
Gradient Boosting Machine	Learning Rate	9	0.2	0.2	0.1	0.2	0.2	0.1
		8	0.2	0.2	0.2	0.2	0.2	0.2
		7	0.2	0.1	0.2	0.2	0.1	0.1
		6	0.2	0.2	0.2	0.2	0.1	0.1
		5	0.1	0.2	0.2	0.2	0.1	0.1
K-nearest Neighbors	Number of Nearest Neighbors	9	9	5	9	9	9	9
		8	9	3	7	9	9	9
		7	7	3	7	9	9	9
		6	3	9	5	9	7	9
		5	3	7	9	5	9	5
Random Forest	Number of Decision Trees	9	100	100	300	300	300	300
		8	100	300	200	300	300	300
		7	200	300	200	100	300	300
		6	200	100	100	100	300	300
		5	300	100	300	100	300	200
Deep Neural Network	Number of Layers, Activation Function Number of Epochs, Batch Size	All	Layers = [256, 128, 64], Activation Function= 'ReLU', Optimizer = 'Adam", Epochs = 300, Batch size = 32					

3.4.8 Evaluation Protocol and Generalization Strategy

To ensure reproducibility, statistical independence, and the elimination of data leakage, all machine-learning models were evaluated using a rigorously isolated data-handling protocol. For each Degree of Freedom (DoF) configuration, the complete dataset was partitioned into 70% training, 15% validation, and 15% testing subsets using stratified random sampling, thereby preserving the spatial and kinematic diversity

of the modular C-arm workspace. Each split was generated with a fixed random seed to guarantee deterministic reproducibility, while ensuring that no individual pose or configuration appeared in more than one subset.

All numerical features were normalized using the StandardScaler implementation in *scikit-learn*, applying a z-score transformation defined as:

$$x' = \frac{x - \mu_{train}}{\sigma_{train}} \quad (3.34)$$

where μ_{train} and σ_{train} denote the mean and standard deviation computed exclusively from the training subset. This approach maintains statistical independence between subsets and eliminates information leakage, a subtle yet common source of optimistic bias in regression tasks. Standardizing within the training domain also harmonizes feature magnitudes across translational and rotational dimensions, thereby improving numerical conditioning, gradient stability for deep models, and feature weighting consistency for distance-based algorithms such as KNN. Model evaluation followed a multi-stage validation pipeline designed to capture both local and global generalization behavior. During the development phase, hyperparameters were optimized through k-fold cross-validation within the training and validation sets. The finalized models were retrained using the merged training and validation data and evaluated on the independent test subset to derive an unbiased estimate of generalization performance. To examine spatial generalization beyond statistical sampling, an additional domain-level validation step was conducted using unseen workspace segments pose clusters intentionally withheld during training. This analysis confirmed that predictive consistency extended to spatially distinct regions of the workspace, demonstrating that the learned mappings captured functional relationships rather than memorized local geometries.

The top-performing Gradient Boosting Machine (GBM) model further underwent a robustness assessment under controlled perturbations to emulate encoder drift, sensor quantization, and minor mechanical backlash. Gaussian noise with zero mean and standard deviations of $\sigma = 0.01,\ 0.05, 0{,}10$ was injected into the test inputs, and variations in MAE, RMSE, and R^2 were analyzed to verify the GBM's numerical resilience and stability under noise (see Section 4.3.3).

Conclusively, model performance was quantified independently for the training, validation, and test subsets using Mean Absolute Error (MAE), Root Mean Square Error (RMSE), and the Coefficient of Determination (R^2). This hierarchical evaluation framework integrating isolated feature scaling, stratified partitioning, cross-domain validation, and noise-based robustness testing ensures that all reported results are statistically sound, free from normalization or sampling leakage, and demonstrably generalizable across the complete 9-DoF modular C-arm workspace.

3.4.9 Evaluation Metrics

To quantitatively evaluate the performance of the machine learning models in predicting collision-free poses of modular C-arm system, four widely accepted regression performance metrics: Mean Absolute Error (MAE), Mean Squared Error (MSE), Root Mean Squared Error (RMSE), and the Coefficient of Determination (R^2) are employed. These metrics provide complementary perspectives on model accuracy, bias, and variance, and have been validated across numerous benchmarking studies in regression modelling [142-143]. Before presenting these metrics, the notation used in the equations is depicted as follows:

- $\mathbf{y_i}$: The true value (ground truth) of the $\mathbf{i^{th}}$ data point.
- $\hat{\mathbf{y}}_\mathbf{i}$: The predicted value output by the model for the $\mathbf{i^{th}}$ sample.
- $\bar{\mathbf{y}}$: The mean of the true values across all samples.
- $\mathbf{n}$: The total number of data samples used for evaluation.

I. Mean Absolute Error (MAE)

MAE quantifies the average absolute difference between the predicted and actual values. It is particularly useful for understanding the magnitude of errors in physical units (e.g., millimeters or degrees) and is robust to outliers compared to squared-error metrics. Lower MAE values indicate higher predictive accuracy. It is calculated using the equation (3.35) as follows:

$$MAE = \frac{1}{n}\sum_{i=1}^{n}|y_i - \hat{y}_i| \qquad (3.35)$$

MAE is particularly suitable for applications where the cost of prediction errors grows linearly and is less sensitive to outliers compared to MSE [143].

II. Mean Square Error (MSE)

MSE calculates the average of the squared differences between true and predicted values. It penalizes larger errors more heavily, making it useful for highlighting model deviations with high impact. It is calculated using the equation (3.36) as follows:

$$MSE = \frac{1}{n}\sum_{i=1}^{n}(y_i - \hat{y}_i)^2 \qquad (3.36)$$

This metric is widely used for its strong mathematical properties in optimization and model training [19].

III. Root Mean Square Error (RMSE)

RMSE is the square root of MSE and retains the original unit of measurement, making it suitable for direct interpretability in physical domains. It is calculated using the equation (3.37) as follows:

$$RMSE = \sqrt{\frac{1}{n}\sum_{i=1}^{n}(y_i - \hat{y}_i)^2} \quad (3.37)$$

The sensitivity of RMSE to larger errors can be both a strength and a drawback, depending on application context [144].

IV. Coefficient of Determination (R2)

R^2, known as the coefficient of determination, quantifies the proportion of variance in the dependent (output) variable that can be explained by the independent (input) variables. It serves as a statistical measure of a model's goodness of fit [145]. The coefficient of determination or R^2 is defined using equation (3.38) as [145]:

$$R^2 = 1 - \frac{SSD_m}{SSD_y} = 1 - \frac{\sum_{i=1}^{n}(y_i - \hat{y}_i)^2}{\sum_{i=1}^{n}(y_i - \bar{y})^2} \quad (3.38)$$

where SSD_y denotes the sum of squared deviations from the mean of the dependent variable (i.e., the total variance in the response data), and SSD_m represents the sum of squared deviations of the model residuals (i.e., prediction errors). An R^2 value close to 1 indicates that the model predictions align closely with the true values, reflecting high predictive accuracy. Conversely, a value near 0 suggests that the model fails to capture the underlying patterns in the data [142].

These metrics were computed for three rotational components (R_x, R_y, R_z) and three translational components (T_x, T_y, T_z), which together constitute the complete 6D pose of the C-arm system within the clinical workspace. Evaluation was carried out across training, validation, and testing subsets for all five machine learning models. In the context of medical robotics and intraoperative imaging, precise task-space prediction is essential to ensure accurate end-effector positioning while maintaining patient safety. Accurate estimation of both position and orientation directly impacts the system's ability to achieve collision-free pose, particularly in constrained surgical environments. This metric-based evaluation supports a rigorous comparison of model performance in terms of pose estimation accuracy, consistency across data splits, and generalization to unseen configurations all of which are critical for deploying intelligent robotic systems that enhance imaging access without compromising clinical safety.

3.5 Chapter Summary

This chapter presented a comprehensive methodological framework unifying the three primary contributions of this thesis: (i) numerical kinematic modelling and surgical workspace analysis, (ii)

trajectory planning and dynamic control of multi-DoF C-arm systems, and (iii) machine learning–based modelling of forward and inverse kinematics.

The chapter began by introducing the integrated kinematic model of the GE OEC-3D C-arm and Steris CMAX™ operating table. Using Denavit-Hartenberg parameterization, forward kinematics of both subsystems were derived and validated against MATLAB Simscape Multibody models with transform sensors. Inverse kinematics was addressed using a numerical iterative solver (L-BFGS-B), incorporating strict joint limits and convergence tolerances. A large-scale workspace analysis pipeline was implemented by sampling joint configurations, applying collision detection via Blender-based watertight meshes, and classifying reachable volumes into collision-free, mixed, and infeasible regions. This ensured that subsequent simulation and planning tasks operated within clinically realizable domains.

The second methodological focus addressed trajectory planning. Four distinct trajectory profiles trapezoidal velocity, cubic polynomial, minimum jerk polynomial, and minimum snap polynomial were implemented and compared within MATLAB Simulink. To ensure robust execution under real-world clinical variability, a Computed Torque Control (CTC) strategy was integrated with the Joint Space Motion Model. Evaluations were conducted across six clinically significant projection trials under both normal (95 kg) and overweight (120 kg) loading conditions, demonstrating how system DoF and patient mass influence trajectory feasibility, smoothness, and positional accuracy. Lookup Tables (LUTs) were then constructed to guide clinicians in selecting trajectory methods and tuning parameters, providing an actionable bridge between simulation and clinical deployment.

The third component outlined the machine learning–based FK/IK framework, where collision-free datasets across 5-9 DoF configurations were curated. Multiple supervised learning algorithms including Ridge Regression, KNN, Random Forest, Gradient Boosting, and Deep Neural Networks were trained in a multi-output regression setting. Architectures were tuned via cross-validation and evaluated with standard regression metrics (MAE, MSE, RMSE, and R^2). These models captured nonlinear couplings across prismatic and revolute joints, offering a scalable alternative to iterative IK solvers while ensuring clinical safety through post-prediction collision and feasibility checks.

Finally, the chapter established evaluation metrics that cut across all methodological components: translational/orientation accuracy for FK/IK, reachable workspace volume, trajectory smoothness and tracking error, regression accuracy for ML models. This common evaluation framework ensures that results presented in the subsequent chapters are both technically rigorous and clinically meaningful.

In conclusion, the methodologies presented here provide a unified, validated, and reproducible pipeline for studying modular C-arm systems with integrated operating tables. By combining analytical modelling, dynamic trajectory optimization, and machine learning-based prediction, this framework establishes a robust foundation for the results and discussions that follow in Chapter 4. It not only enables large-scale

simulation under realistic constraints but also advances toward clinically deployable decision-support tools for intelligent surgical imaging systems.

Chapter 4 : Results and Discussions

The results and discussion of the three contributions of this thesis are presented in this chapter. In section 4.1, the outcomes of numerical FK/IK modelling and workspace analysis of the integrated multi-DoF C-arm and operating table system are examined. In section 4.2, the trajectory planning and control experiments are reported, with emphasis placed on robustness under varying patient loads and optimization across polynomial trajectory methods. In section 4.3, the machine learning-based FK/IK results are outlined, and predictive accuracy across different models together with their clinical relevance are highlighted. We conclude with a section focused on clinical implications. We also note here additional results are included in the appendices.

4.1 Numerical FK/IK and Surgical Workspace Evaluation

The total surgical workspace of the C-arm device and operating table integrated system increases as the DoF increases. Setup #5 with the highest DOF has the largest workspace. Whereas setup #6 and setup #1 have the same DoF, setup #6 with operating table joints has 1.4 times larger workspace compared to setup #1 with C-arm joints. Operating table joints with a large range of motion (joint limits) created a larger workspace compared to C-arm joints. Reachable workspace, i.e., collision-free and mixed collision regions vary based on the clinical interventional projection. For all six interventions provided in this study, setup #5 with highest DoF has the largest reachable workspace. Except for Vascular, for all other clinical interventions moving the operating table alone (setup #6) has more reachable workspace than moving the C-arm (setup #1 and setup #2). For these clinical interventions, C-arm tilt joint value is either zero or inverted to 180°, and in these configurations the C-shaped joint is close to the operating table base which creates more collisions for C-arm movements than operating table joint movements. Vascular projection V2 has the highest reachable workspace of 83.12 % for setup #5. In our setup, the C-arm is on the right side of the operating table which created a more reachable workspace for the V2 clinical intervention. In a similar setup with C-arm positioned on the left side of the operating table would have more reachable workspace for the Vascular V1 clinical interventional projection. For the V1 projection, there is no reachable workspace possible by moving the C-arm or operating table alone. Both C-arm and table joints need to be moved together to achieve collision-free pose. The reachability of a setup w.r.t that setup's total workspace provided in Table 4.1 shows that setup #6 (table joints) has the highest collision-free movement except for the Vascular interventions. For V2 projection, this value is closer to highest, whereas it is zero for the V1 projection since both C-arm and table joints need to be moved. This demonstrates that moving table joints could produce more collision-free poses.

Table 4.1: Workspace Reachability Comparative Analysis.

Projection	Setup	Reachability volume w.r.t its total workspace (%)	Reachability volume w.r.t setup#5's total workspace (%)	Reachability volume w.r.t setup#5's reachable workspace (%)
PA	1	5.74	0.42	1.28
	2	8.66	1.7	5.21
	3	8.81	3.9	11.97
	4	27.59	20.46	**62.75**
	5	32.6	**32.6**	100
	6	**100**	10.37	31.8
AP	1	5.74	0.42	1.22
	2	6.46	1.26	3.69
	3	6.62	2.93	8.55
	4	27.92	20.72	**60.51**
	5	34.23	**34.23**	100
	6	**50**	5.18	15.13
V1	1	0	0	0
	2	0	0	0
	3	4.15	1.83	4.13
	4	19.71	14.61	**32.92**
	5	**44.39**	**44.39**	100
	6	0	0	0
V2	1	90.85	6.59	7.93
	2	**92.83**	18.2	21.9
	3	87.96	38.92	46.82
	4	84.72	62.85	**75.61**
	5	83.12	**83.12**	100
	6	87.5	9.08	10.92
Ver	1	12.98	0.94	2.44
	2	17.72	3.48	9.01
	3	18.18	8.07	20.91
	4	31.7	23.58	**61.11**
	5	38.59	**38.59**	100
	6	**79.17**	8.22	21.31
Lat	1	38.51	2.79	5.44
	2	37.59	7.34	14.34
	3	32.05	14.14	27.63

	4	40.53	29.95	**58.51**
	5	51.19	**51.19**	100
	6	**93.75**	9.7	18.94

Since setup #5 with highest DoF has the largest workspace, this is used as baseline to calculate the reachability of other setups w.r.t setup 5 (Table 4.1). This quantifies the proportion of increase in reachability when a specific joint is added to the setup. For example, in the Posterior-Anterior (PA) projection, setup #2 with C-arm joints could reach 5.21% of maximum collision-free workspace. Adding operating table transverse joint (setup #3) increased reachability to 11.97% whereas including both table transverse and vertical joints (setup #4) significantly increased the reachability to 62.75%. This shows that operating table vertical joints have more collision-free reach compared to transverse joints. All the other clinical interventional projections followed the same trend.

Overall, this surgical workspace analysis shows the increase in workspace with increasing DoF, advantage of increased collision-free workspace from moving the operating table joints compared to C-arm joints, and demonstration that operating table movement is essential for some interventions like Vascular V1. In Table 4.2, minimum and maximum values of workspace in each coordinate axis w.r.t table end-effector are provided. Although these boundaries include both collision and collision-free poses, these values show an increase in the workspace with increasing DoF and amount of change in each coordinate axis direction. Workspace with sampled collision-free, collision, mixed-collision, and empty $5cm \times 5cm \times 5cm$ boxes details for all setups and clinical interventional projections are available in GitHub. This information could be used as a look-up table to pre-plan potential joints movements to achieve a desired clinical intervention pose.

To evaluate numerical IK finding collision-free solution, a dataset with 139,213 collision-free samples of random joint configurations and target pose pairs was created from setup #5's workspace (Table 4.3). In IK results (Table 4.4), setup #5 has the highest achievable poses as well as the lowest errors – within clinical tolerances of ±1mm and ±1°. This is true between 97.21% and 99.98% of all collision-free poses, and for all six interventional configurations. In future work, the dataset employed in this thesis could be used to train neural network models to obtain accurate IK solutions [146], [147]. Today's C-arm devices are sold with imaging capabilities and/or image capture functionalities accounting for mechanical errors and image distortion. To further account for potential positioning errors, surgeons are required to utilize advanced software features like virtual fluoroscopy systems that employ 2D/3D registration techniques between preoperative data and live X-ray images. Algorithms typically generate Digitally Reconstructed Radiographs (DRRs) from patient CT volumes to predict the 3D pose of the patient, minimizing misalignment between the CT and X-ray images, which should account for potential C-arm errors. Once the pose is established after a precise 2D/3D registration, the surgery can continue [35][147-148].

Table 4.2: Workspace Range and Volume Results.

Projection	Setup	Randomly generated poses						No. of 5 cm × 5 cm × 5 cm boxes				
		t_x^{min} (cm)	t_x^{max} (cm)	t_y^{min} (cm)	t_y^{max} (cm)	t_z^{min} (cm)	t_z^{max} (cm)	Collision-free	Mixed Collision	Empty	Collision	Total
PA	1	31.0	77.0	−9.78	7.5	6.35	63.65	0	27	10	443	480
	2	31.0	77.0	−9.78	7.5	−43.65	113.65	17	93	10	1,160	1,280
	3	31.0	77.0	−22.78	20.5	−43.65	113.65	52	201	9	2,618	2,880
	4	−5.0	77.0	−22.78	20.5	−43.65	113.65	1,063	263	90	3,480	4,896
	5	−5.0	77.0	−22.78	20.5	−113.31	113.65	**979**	**1,134**	556	4,369	**7,038**
	6	−5.0	31.0	−20.5	5.5	−35.0	35.0	672	0	0	0	672
AP	1	31.0	77.0	−9.78	7.5	6.35	63.65	27	0	10	443	480
	2	31.0	77.0	−9.78	7.5	−43.65	113.65	64	18	11	1,187	1,280
	3	31.0	77.0	−22.78	20.5	−43.65	113.65	145	45	10	2,680	2,880
	4	−5.0	77.0	−22.78	20.5	−43.65	113.65	976	368	82	3,470	4,896
	5	−5.0	77.0	−22.78	20.5	−113.65	113.65	**952**	**1,269**	550	4,267	**7,038**
	6	−5.0	31.0	−20.5	5.5	−35.0	35.0	252	84	0	336	672
V1	1	31.0	77.0	−9.78	7.5	6.35	63.65	0	0	10	470	480
	2	31.0	77.0	−9.78	7.5	−43.65	113.65	0	0	10	1,270	1,280
	3	31.0	77.0	−22.78	20.5	−43.65	113.65	12	107	11	2,750	2,880
	4	−5.0	77.0	−22.78	20.5	−43.65	113.65	557	392	81	3,866	4,896
	5	−5.0	77.0	−22.78	20.5	−113.13	113.65	**1,111**	**1,772**	543	3,612	**7,038**
	6	−5.0	31.0	−20.5	5.5	−35.0	35.0	0	0	0	672	672
V2	1	31.0	77.0	−9.78	7.5	6.35	63.65	373	54	10	43	480
	2	31.0	77.0	−9.78	7.5	−43.65	113.65	988	191	10	91	1,280
	3	31.0	77.0	−22.78	20.5	−43.65	113.65	2,073	448	14	345	2,880
	4	−5.0	77.0	−22.78	20.5	−43.65	113.65	3,122	949	91	734	4,896
	5	−5.0	77.0	−22.78	20.5	−113.48	113.48	**3,921**	**1,463**	561	1,093	**7,038**
	6	−5.0	31.0	−20.5	5.5	−35.0	35.0	518	70	0	84	672
Ver	1	31.0	77.0	−9.78	7.5	6.35	63.65	9	52	10	409	480
	2	31.0	77.0	−9.78	7.5	−43.65	113.65	51	174	10	1,045	1,280
	3	31.0	77.0	−22.78	20.5	−43.65	113.65	205	317	9	2,349	2,880
	4	−5.0	77.0	−22.78	20.5	−43.65	113.65	1,043	483	82	3,288	4,896
	5	−5.0	77.0	−22.78	20.5	−113.65	113.48	**965**	**1,532**	567	3,974	**7,038**
	6	−5.0	31.0	−20.5	5.5	−35.0	35.0	448	84	0	140	672
Lat	1	31.0	77.0	−9.78	7.5	6.35	63.65	137	44	10	289	480
	2	31.0	77.0	−9.78	7.5	−43.65	113.65	322	155	11	792	1,280
	3	31.0	77.0	−22.78	20.5	−43.65	113.65	632	287	13	1,948	2,880
	4	−5.0	77.0	−22.78	20.5	−43.65	113.65	1,438	508	95	2,855	4,896

	5	−5.0	77.0	−22.78	20.5	−113.48	113.65	**1,378**	**1,948**	541	3,171	**7,038**
	6	−5.0	31.0	−20.5	5.5	−35.0	35.0	588	42	0	42	672

Table 4.3: Collision-free Target Poses Randomly Sampled from C-arm and Operating table Workspace (Setup #5 with 7 DoF) for Interventional Configurations.

Projection	No. of collision-free target poses (Total no. of poses = 139,213)
Posterior-Anterior (PA)	17,292
Anterior-Posterior (AP)	17,278
Vascular 1 (V1)	16,583
Vascular 2 (V2)	42,610
Vertebroplasty (Ver)	18,733
Lateral (Lat)	26,717

Table 4.4: Inverse Kinematics Errors and Collision-free Poses Results.

Projection	**No. of poses**	**Setup**	**Inverse Kinematics Collision-free poses (%)**			
			No. of poses	$\|T^{err}_{\{x,y,z\}}\| \leq 1mm$	$\|R^{err}_{\{x,y,z\}}\| \leq 1°$	$\|T^{err}_{\{x,y,z\}}\| \leq 1mm$ *and* $R^{err}_{\{x,y,z\}} \leq 1°$
PA	17,292	1	71.94	0	71.94	0
		2	77.03	2.1	77.03	2.1
		3	77.21	5.67	77.21	5.67
		4	77.21	49.2	77.21	49.2
		5	**99.35**	**99.35**	**99.35**	**99.35**
		6	100	30.5	12.54	4.35
AP	17,278	1	73.15	0	73.15	0
		2	78.68	2.63	78.68	2.63
		3	78.89	6.97	78.89	6.97
		4	76.74	48.57	76.74	48.57
		5	**99.06**	**99.06**	**99.06**	**99.06**
		6	45.08	10.6	5.82	1.57
V1	16,583	1	0	0	0	0
		2	3.79	0.19	3.79	0.19

		3	14.54	2.65	14.54	2.65
		4	57.02	24.71	57.02	24.71
		5	**97.21**	**97.21**	**97.21**	**97.21**
		6	0	0	0	0
V2	42,610	1	76.79	0.05	76.79	0.05
		2	81	15.65	81	15.65
		3	82.21	37.97	82.21	37.97
		4	97.59	63.69	97.59	63.69
		5	**99.98**	**99.98**	**99.98**	**99.98**
		6	68.35	9.69	5.18	0.91
Ver	18,733	1	8.49	0.02	8.49	0.02
		2	10.33	3.73	10.33	3.73
		3	36.03	13.23	36.03	13.23
		4	75.95	49.95	75.95	49.95
		5	**99.03**	**99.03**	**99.03**	**99.03**
		6	90.05	25.45	12.24	3.62
Lat	26,717	1	71.5	0.04	71.5	0.04
		2	75.64	9.37	75.64	9.37
		3	76.08	22.78	76.08	22.78
		4	76.27	47.53	76.27	47.53
		5	**98.44**	**98.44**	**98.44**	**98.44**
		6	100	20.01	4.34	1.05

Table 4.8 and Table 4.11 under section 4.4 showcase DRR errors within the clinical tolerances of ±1mm and ±1° as attributed to setup#5. These DRRs can be used to produce accurate 2D/3D registration overlays to help navigate the surgery. Future work would reply on the clinical validation and use of such overlays on real patient surgeries while moving both C-arm device and operating table.

4.2 Trajectory Planning and Motion Control

The results are discussed for each of the two evaluation phases beginning with the impact of patient weight and concluding with detailed kinematic optimization, trajectory planning LUT.

4.2.1 Impact of Patient Weight (Trials 1,2,3)

Across all configurations and trajectories, overweight patient conditions consistently resulted in increased positional errors as illustrated in Appendix 1.**Error! Reference source not found.**For example, in Trial 1 under a 9DoF configuration, the C-arm Lateral joint exhibited errors of -0.0093 ± 0.0008cm for overweight

compared to -0.0074 ± 0.0008cm for normal weight with the Trapezoidal Velocity Profile trajectory. However, this increased positional errors though significant in relative terms, corresponds to low absolute deviations due to the system's precise control and trajectory planning. For instance, even under overweight conditions, positional errors for critical axes remained within clinically acceptable thresholds, with deviations in the range of 0.001cm to 0.03cm across all configurations and trajectories. These findings validate the robustness of the system's design and control methodology in managing dynamic loads associated with higher patient weights.

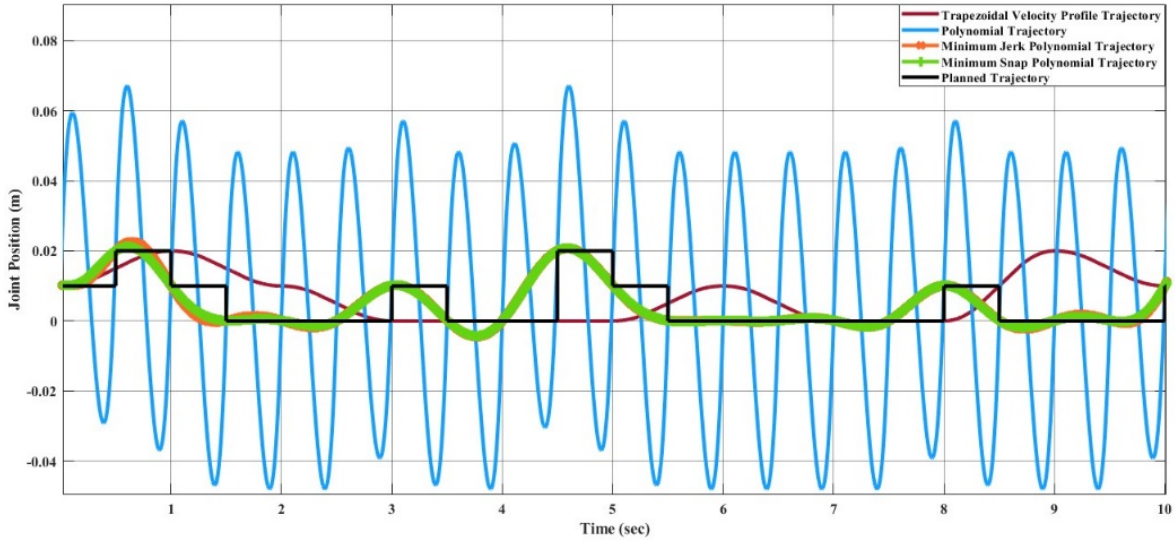

Figure 4.1: Position profile of C-arm Vertical across four trajectory planning methods in 9 DoF configuration.

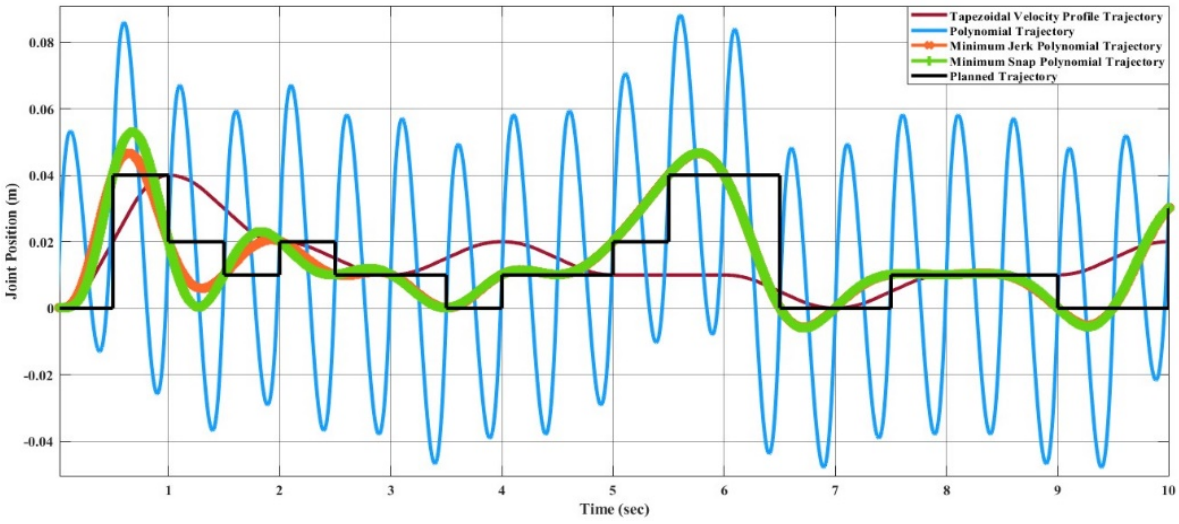

Figure 4.2: Position profile of C-arm Vertical across four trajectory planning methods in 8 DoF configuration.

Polynomial-based trajectories (Minimum Jerk and Minimum Snap) demonstrated superior performance in reducing positional errors across both weight categories. For instance, in Trial 2, the Minimum Snap trajectory under the 8DoF configuration resulted in an error of -0.0159 ± 0.0011cm on the C-arm Lateral axis, significantly lower than the Trapezoidal Velocity Profile trajectory. These trajectories ensured smoother transitions, reducing abrupt joint movements even under higher load conditions. Higher DoF configurations (8DoF and 9DoF) showed enhanced adaptability and precision, with positional errors reduced by approximately 20–30% compared to lower DoF setups. This improvement underscores the importance of kinematic flexibility in maintaining accuracy under dynamic weight conditions. For a visual understanding, the Trajectory tracking of the C-arm Vertical joint for a 9DoF C-arm system in Trial 1 are illustrated in Figs. 4.1-4.5.

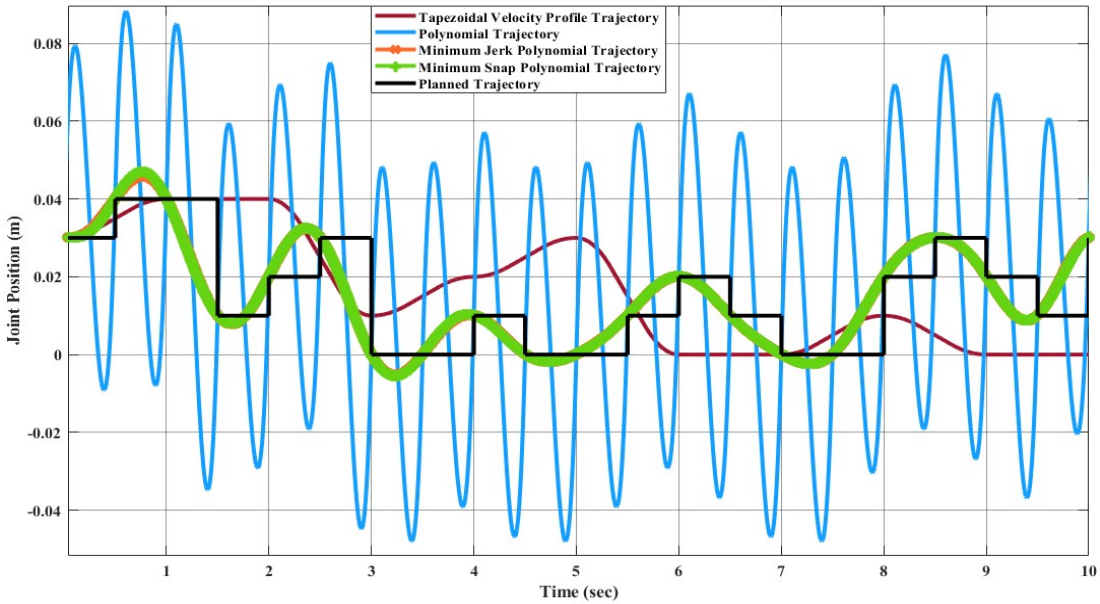

Figure 4.3: Position profile of C-arm Vertical across four trajectory planning methods in 7 DoF configuration.

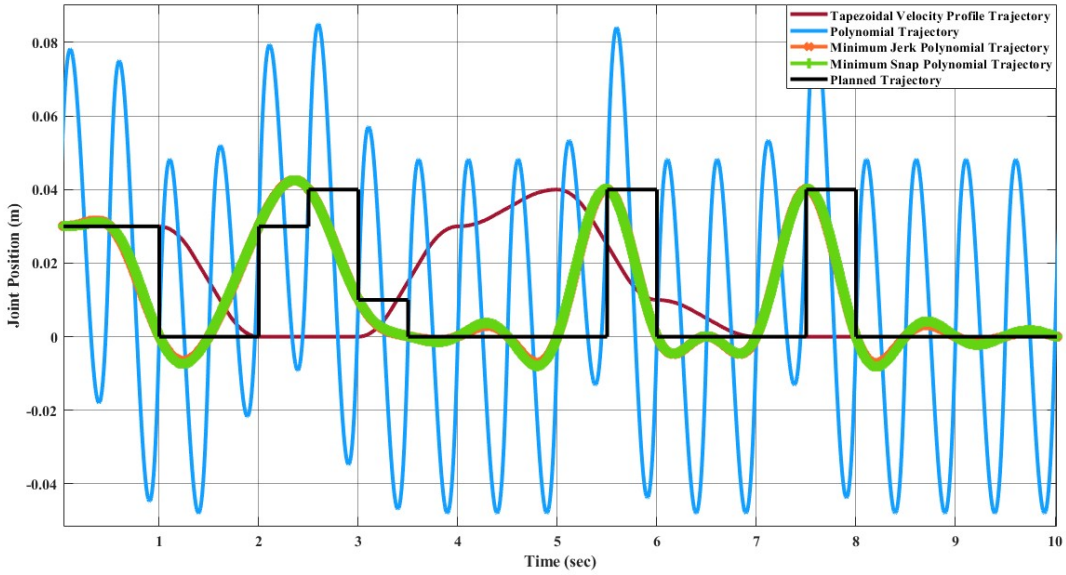

Figure 4.4: Position profile of C-arm Vertical across four trajectory planning methods in 6 DoF configuration.

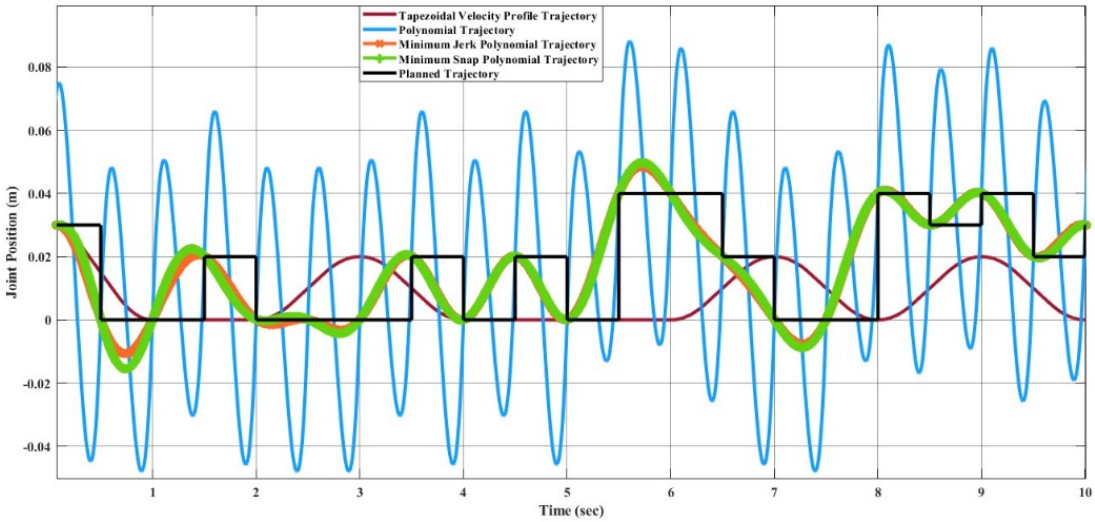

Figure 4.5: Position profile of C-arm Vertical across four trajectory planning methods in 5 DoF configuration.

4.2.2 Kinematic and Trajectory Optimization (Trials 4,5,6)

Given the system's demonstrated capability to handle patient overweight conditions with minimal performance degradation, the second phase of evaluation focused exclusively on normal weight patient conditions to streamline the analysis and optimize computational efficiency. By isolating the weight variable, the second phase ensured that the observed performance trends, particularly in trajectory

smoothness and positional accuracy, were attributed solely to kinematic and control parameters, rather than external dynamic factors.

The results consistently demonstrated the superior performance of polynomial-based methods, specifically Minimum Jerk and Minimum Snap trajectories, over Trapezoidal and standard Polynomial trajectories as shown in Appendix 2. In Trial 4, the C-arm Horizontal joint under the Minimum Jerk trajectory in the 9DoF configuration exhibited an error of 0.0057 ± 0.0025cm, compared to 0.0032 ± 0.0013cm in the 8DoF setup, indicating trajectory-specific benefits across configurations. Therefore, Minimum Jerk and Minimum Snap trajectories significantly reduced positional variability, ensuring consistent and smooth joint motion across all axes. This smoothness is particularly critical for clinical applications requiring high precision and minimal abrupt movements.

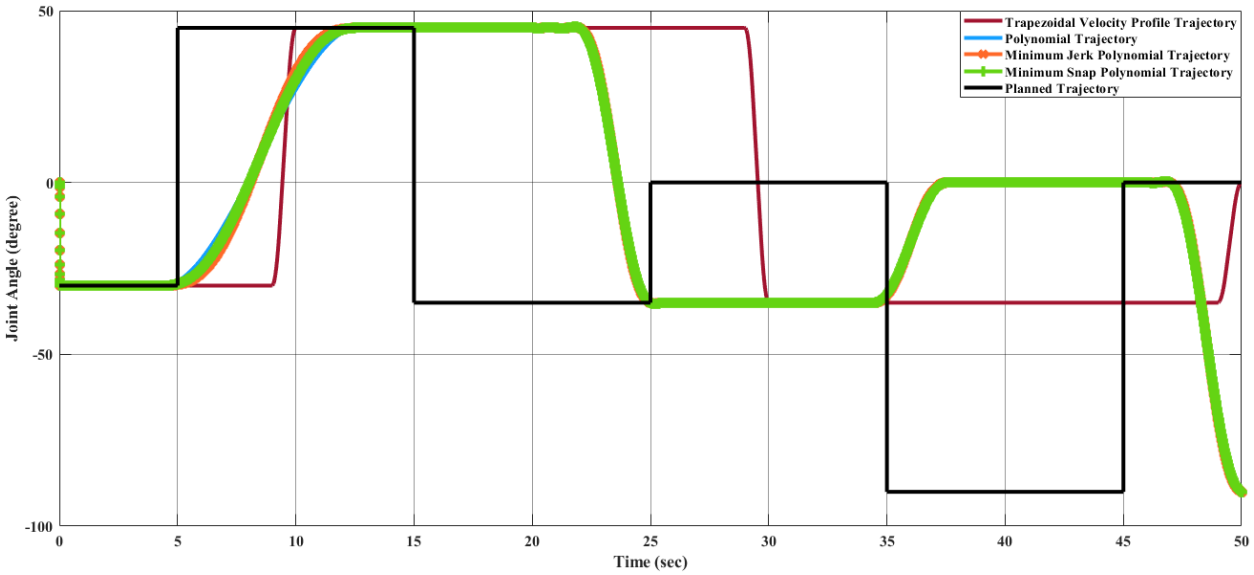

Figure 4.6: Angle profile of C-arm Orbital across four trajectory planning methods in 9 DoF configuration.

Higher DoF configurations demonstrated lower positional errors and smoother trajectories, with the 9DoF configuration achieving the best results. For instance, in Trial 6, the C-arm Orbital axis exhibited an error of -0.0076 ± 0cm under the Minimum Snap trajectory, showcasing superior precision. Contrarywise, lower DoF configurations (5DoF and 6DoF) showed higher deviations, particularly in dynamic axes such as C-arm Horizontal, where errors reached up to 0.0062 ± 0.0002cm in the 5-DoF setup. It is worth noting that the lower DoF configurations exhibit smoother trajectory tracking in some trajectories such as Trial 6 as exemplified in Figs. 4.6 - 4.10, but at the cost of reduced positional accuracy and limited adaptability, whereas higher DoF configurations achieve superior positional precision and flexibility but may exhibit

slightly less smooth trajectory tracking due to their increased system complexity. This finding underscores the importance of tailoring the choice of DoF configuration to specific clinical needs. For tasks requiring simplicity and smooth trajectory execution, lower DoF configurations may suffice. However, for complex imaging tasks demanding precision and adaptability, higher DoF systems are essential, with further opportunities for optimizing control algorithms to address their inherent complexity.

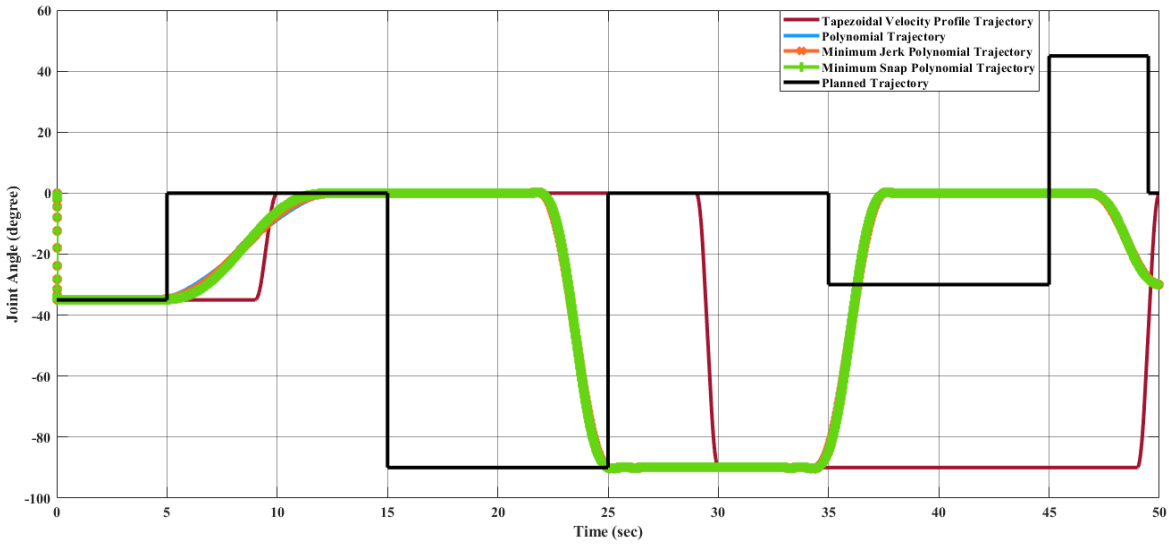

Figure 4.7: Angle profile of C-arm Orbital across four trajectory planning methods in 8 DoF configuration.

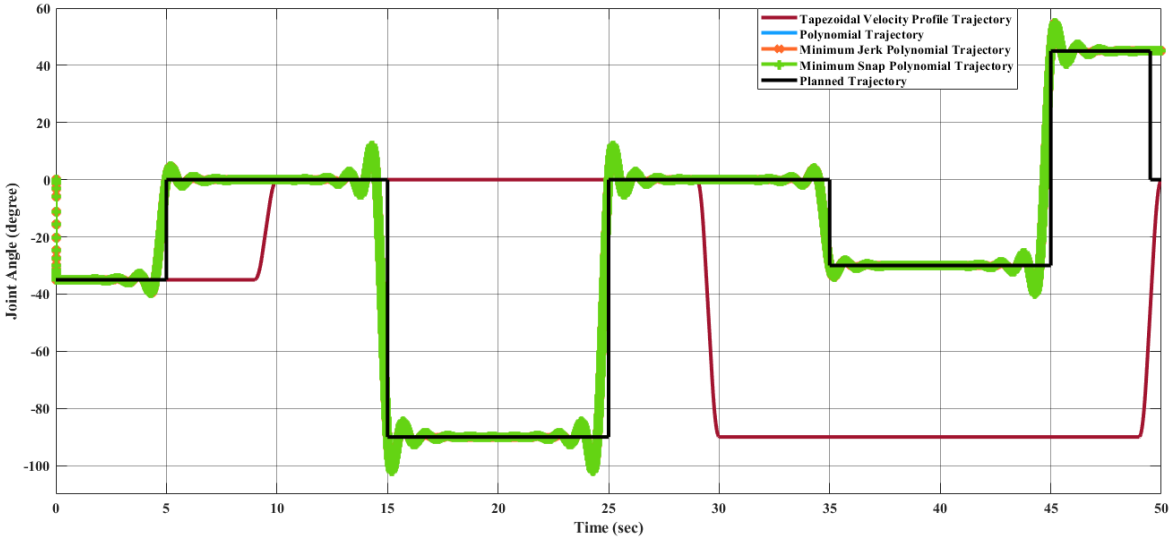

Figure 4.8: Angle profile of C-arm Orbital across four trajectory planning methods in 7 DoF configuration.

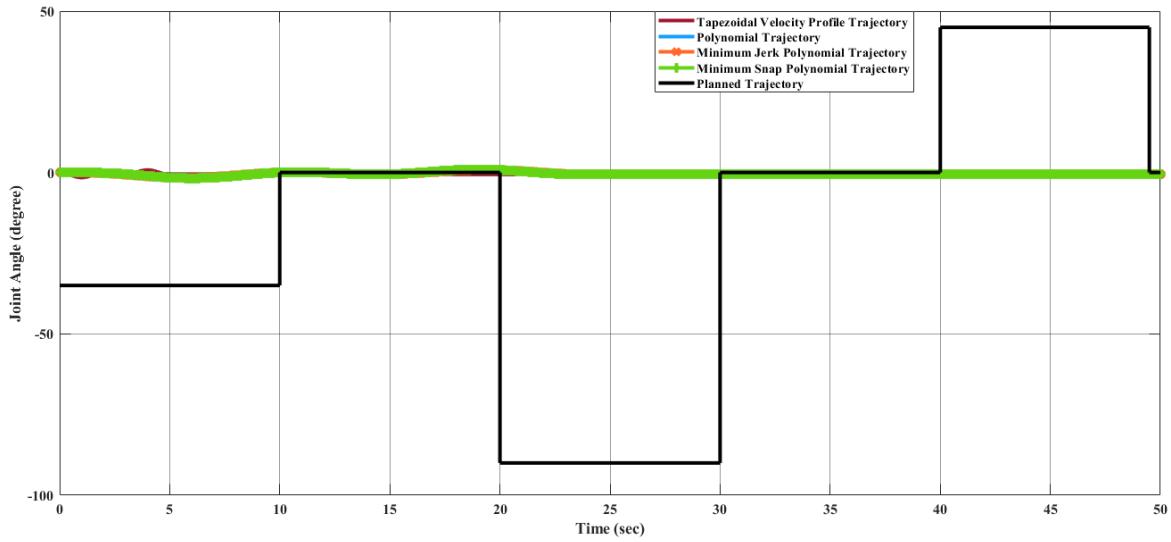

Figure 4.9: Angle profile of C-arm Orbital across four trajectory planning methods in 6 DoF configuration.

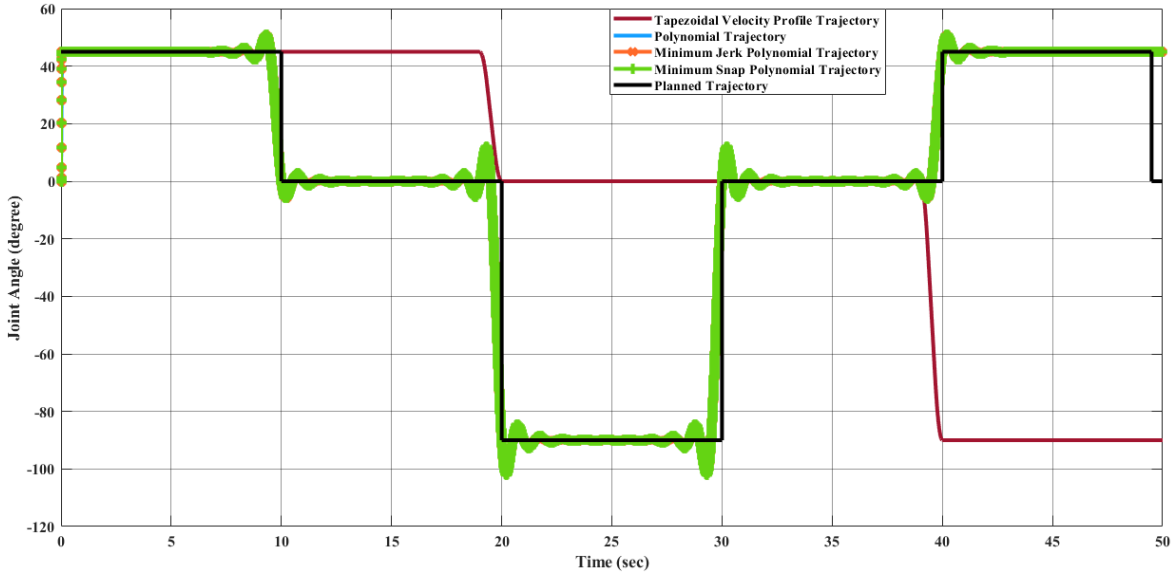

Figure 4.10: Angle profile of C-arm Orbital across four trajectory planning methods in 5 DoF configuration.

4.3 Evaluation of Machine Learning Approaches for FK/IK

4.3.1 Machine Learning-Based Forward Kinematics

The application of machine learning models is investigated to solve the forward kinematics problem, wherein joint variables from the 9DoF C-arm system serve as inputs to predict the corresponding 6D end-effector poses comprising three Euler angles and three translational components. A range of regression

techniques, including linear models and ensemble-based approaches, is employed to learn the complex mapping from joint space to task space. To evaluate model performance comprehensively and support the selection of optimal learning strategies for high-dimensional pose estimation, twelve heatmaps are generated as shown in Fig. 4.11– 4.22. These visualizations report standard regression metrics described in the last section across the training, validation, and testing phases. These visualizations compare model accuracy for each of the six pose components: three translation vectors (t_x, t_y, t_z) and three Euler angles (r_x, r_y, r_z) under the 9DoF configuration which are represented in the heatmaps as T_x, T_y, T_z and R_x, R_y, R_z respectively. For clarity, all errors in translational vectors are reported in millimeters (mm), while errors in Euler angles are expressed in degrees (°).

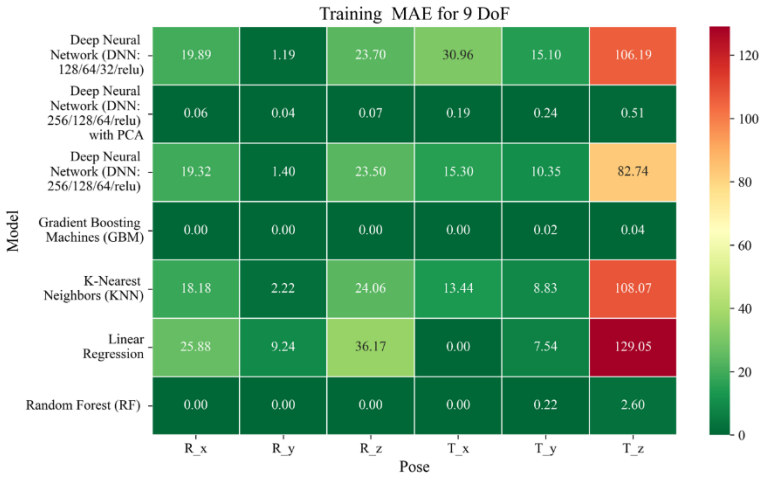

Figure 4.11: Heatmap of training set Mean Absolute Error for machine learning models.

Among all models as represented in Fig. 4.11 - 4.13 , GBM demonstrate the lowest MAE values. For Euler angles, the training, validation, and testing MAEs are all zero, indicating perfect alignment between predicted and ground truth rotations. For translational vectors, GBM achieves training MAEs ranging from 0 to 0.04 mm, validation MAEs from 0 to 0.07 mm, and testing MAEs from 0 to 0.07 mm. The DNN with PCA performs nearly as well. For Euler angles, MAEs range from 0 to 0.07° across all three phases. For translational components, training MAE ranges from 0.19 to 0.51 mm, validation MAE from 0.19 to 0.52 mm, and testing MAE from 0.19 to 0.52 mm. The standard DNN without PCA shows higher error magnitudes. For Euler angles, training MAEs range from 1.40 to 23.50°, validation MAEs from 1.41 to 24.10°, and testing MAEs from 1.42 to 22.81°. For translations, training MAEs range from 10.35 to 82.74 mm, validation from 10.39 to 82.48 mm, and testing from 10.35 to 83.16 mm.

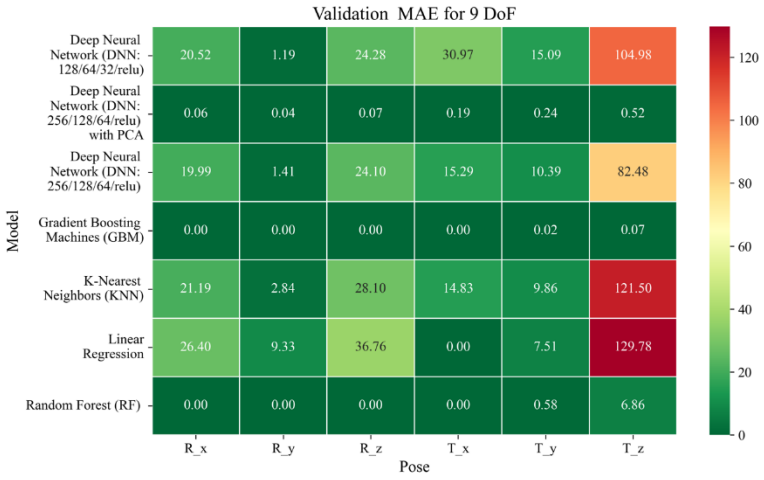

Figure 4.12: Heatmap of validation set Mean Absolute Error for machine learning models.

Figure 4.13: Heatmap of test set Mean Absolute Error for machine learning models.

The MSE analysis, as illustrated in Figs. 4.14 – 4.16, provides insight into the magnitude of squared prediction errors across models and datasets, while the RMSE analysis in Figs. 4.17 – 4.19 reaffirms MAE trends by offering a scale-sensitive interpretation of model performance. GBM again performs exceptionally well, with 0° RMSE for Euler angles across all splits and translational RMSE ranging from 0 to 0.06 mm (training), 0 to 0.09 mm (validation), and 0 to 0.09 mm (testing). For DNN with PCA, Euler angle RMSE spans 0.05 to 0.16° (training), 0.06 to 0.17° (validation), and 0.05 to 0.16° (testing). Translational RMSE lies between 0.23 to 0.64 mm consistently across all three phases. The DNN without PCA yields RMSE values for Euler angles between 1.90 to 58.38° (training), 1.92 to 59.70° (validation), and 1.92 to 56.96° (testing). For translational vectors, RMSE spans 12.66 to 104.38 mm (training), 12.71 to 104.38 mm (validation), and 12.69 to 104.83 mm (testing).

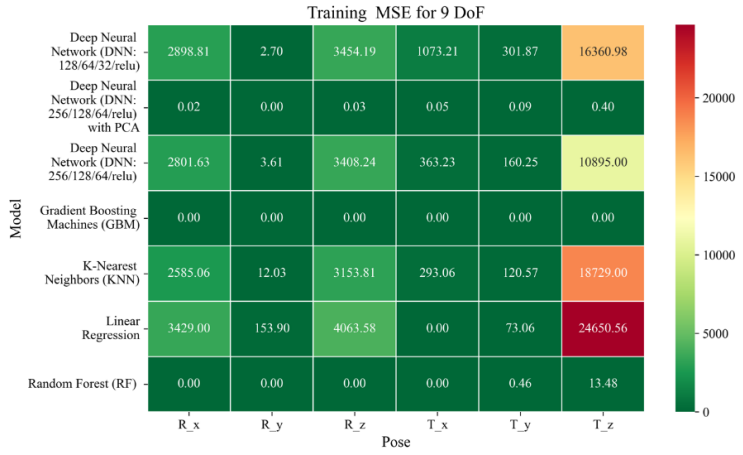

Figure 4.14: Heatmap of training set Mean Square Error for machine learning models.

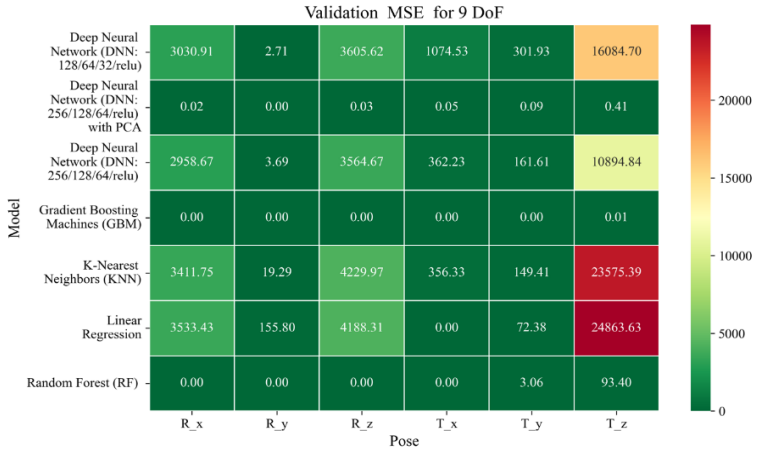

Figure 4.15: Heatmap of validation set Mean Square Error for machine learning models.

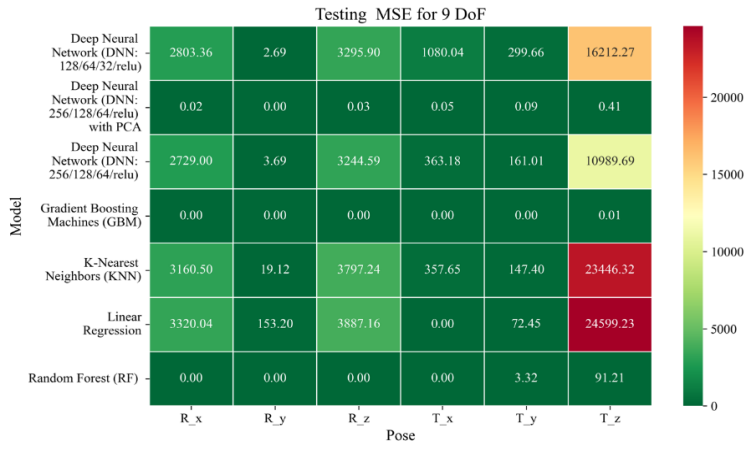

Figure 4.16: Heatmap of test set Mean Square Error for machine learning models.

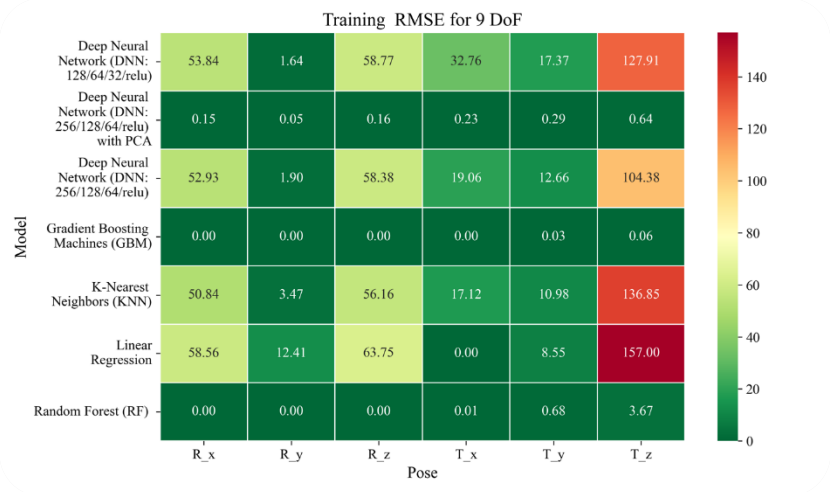

Figure 4.17: Heatmap of training set Root Mean Square Error for machine learning models.

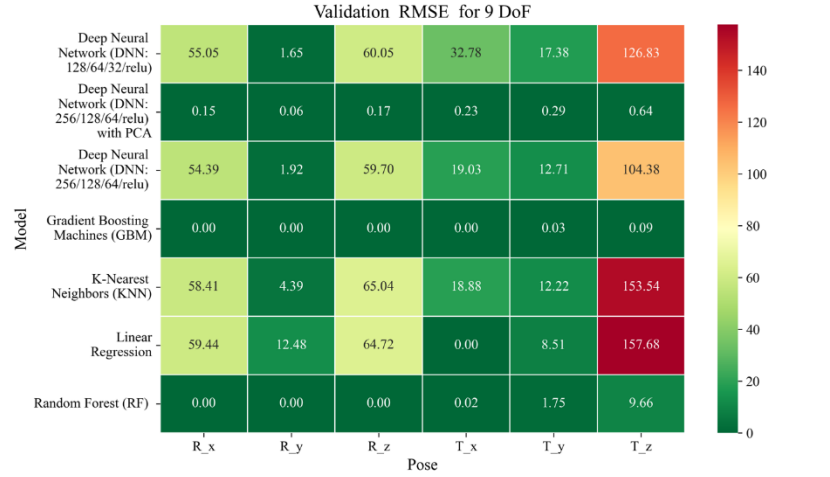

Figure 4.18: Heatmap of validation set Root Mean Square for machine learning models.

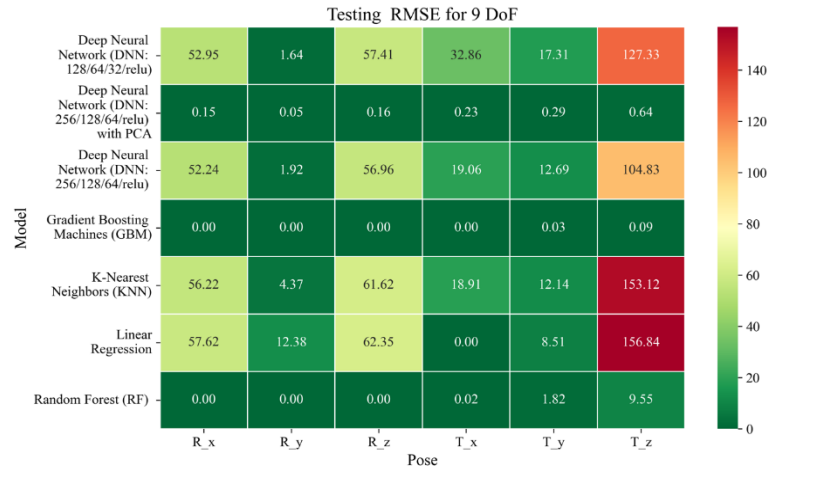

Figure 4.19: Heatmap of test set Root Mean Square Error for machine learning models.

The coefficient of determination (R^2) as depicted in Figs. 4.20 - 4.22 provides a normalized measure of how well the predicted values explain the variance in the actual pose components. Among all models evaluated, GBM achieves a perfect R^2 of 1.00 across all pose components encompassing both Euler angles and translational vectors during training, validation, and testing. While this indicates that the model captures the full variance present in the target data, such ideal scores, particularly when accompanied by near-zero MAE and RMSE values, require cautious interpretation.

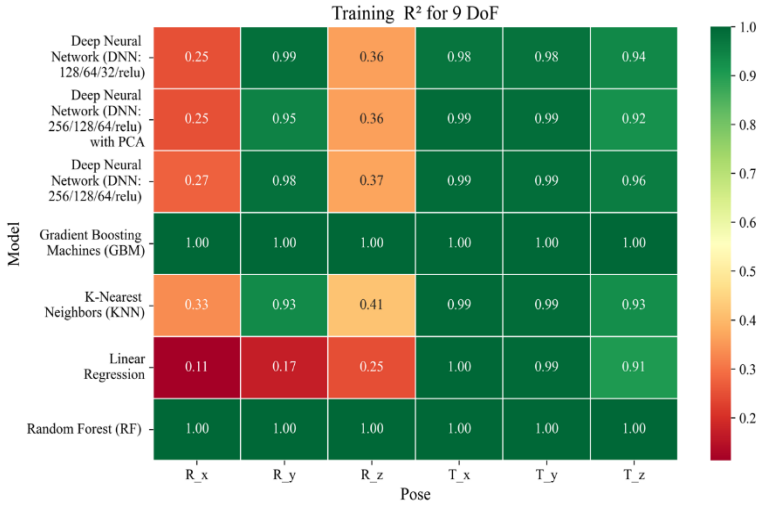

Figure 4.20: Heatmap of training set. Coefficient of Determination for machine learning models.

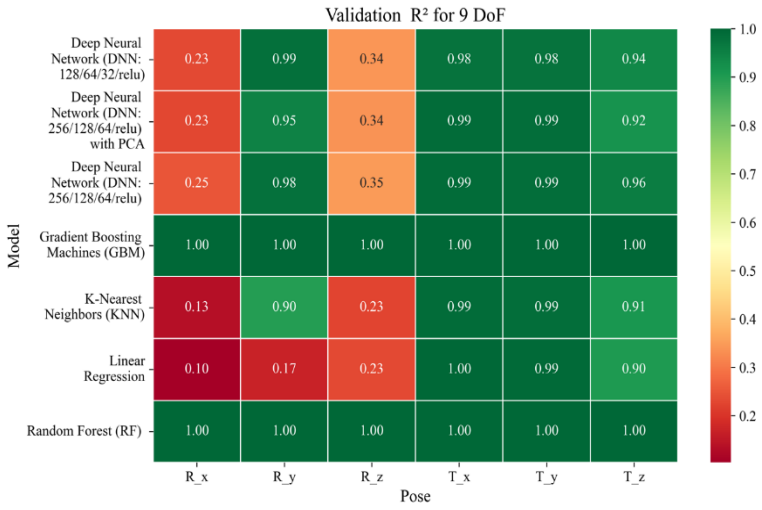

Figure 4.21: Heatmap of validation set Coefficient of Determination for machine learning models.

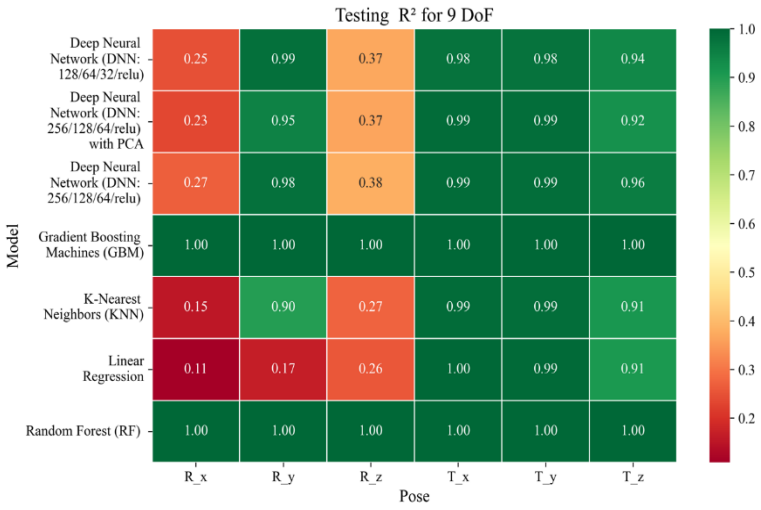

Figure 4.22: Heatmap of test set Coefficient of Determination for machine learning models.

To address potential concerns related to overfitting or data leakage, the evaluation protocol includes a clearly defined train-test split strategy and *k*-fold cross-validation during model development and hyperparameter tuning. These procedures ensure that model performance is not attributed to memorization or overlap across datasets. Nevertheless, validation on independent datasets remains essential to further establish the model's generalizability and robustness in real-world applications. The Deep Neural Network with PCA demonstrates high R^2 values for translational components across all splits, ranging from 0.92 to 0.99, indicating that the model captures nearly all variance in the positional data. This is consistent with the low RMSE values and reflects the relative linearity and predictability of translational motion from joint inputs. For rotational components, however, the R^2 values are more modest ranging from 0.25 to 0.36 (training), 0.23 to 0.35 (validation), and 0.23 to 0.37 (testing). These lower scores are not necessarily indicative of poor performance; rather, they reflect the inherently higher complexity and sensitivity of predicting angular components (Euler angles), where even small discrepancies can result in a large proportion of unexplained variance. Additionally, rotational motion tends to be more nonlinear and sensitive to joint interactions, making it harder for the model to explain variance compared to translational motion. The standard DNN without PCA follows a similar trend, achieving high R^2 values for translational vectors ranging from 0.96 to 0.99, and lower R^2 values for rotational components ranging from 0.25 to 0.35 across all three datasets. The slightly lower R^2 scores compared to the PCA-enhanced version suggest that feature dimensionality reduction plays a role in improving angular variance modelling by reducing noise and multicollinearity in the input space.

In summary, GBM establishes itself as the most accurate and reliable forward kinematics model for the 9DoF modular C-arm system, achieving near-zero error metrics and perfect variance capture across all pose

components. The DNN with PCA emerges as a viable alternative, particularly for translational tasks, while the standard DNN highlights the challenges posed by high-dimensional, nonlinear pose mapping.

4.3.2 Machine Learning-Based Inverse Kinematics

To address the inverse kinematics problem in a 9DoF C-arm robotic system with operating table, we recall that the input features consist of translation vectors (t_x, t_y, t_z) and rotational components encoded as Euler angles (r_x, r_y, r_z). The output space encompasses six C-arm joints and three operating table joints. Similarly, machine learning models are evaluated against the evaluation metrics, and their performance are manifested through twelve heatmaps (Figs. 4.23 – 4.34) across training, validation, and test datasets.

Among all evaluated approaches, the GBM model consistently delivers superior accuracy and generalization. For revolute joints specifically the C-arm Wigwag, Tilt, and Orbital joints GBM achieves perfect predictive accuracy, attaining MAE and RMSE values of 0.00° across all phases. This remarkable performance demonstrates the model's capacity to effectively learn the nonlinear transformation from Cartesian rotational descriptors to joint angles, despite the high dimensionality and inherent complexity of the rotational kinematics involved.

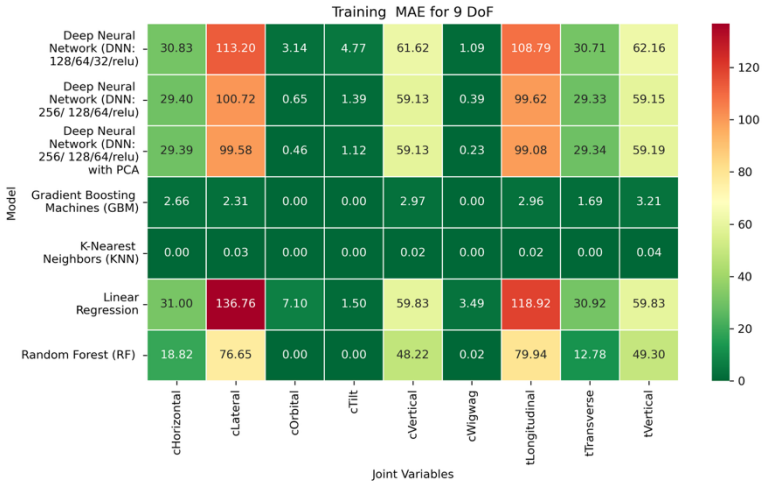

Figure 4.23: Heatmap of Training Set. Mean Absolute Error for Inverse Kinematics ML.

In contrast, performance on prismatic joints exhibits variation influenced by joint-specific mechanical constraints and pose-to-configuration mapping complexity. For the C-arm Vertical, C-arm Horizontal, Table Vertical, Table Longitudinal, and Table Transverse axes, error magnitudes differ across datasets. During the training phase, as illustrated in Fig. 4.23, the Table Transverse joint records the lowest MAE at 1.69 mm, while the Table Vertical joint exhibits the highest MAE at 3.21 mm. In the validation phase, shown in Fig. 4.24, the C-arm Horizontal joint incurs the largest error at 4.73 mm, whereas Table Transverse remains the most accurately predicted with an MAE of 2.66 mm. A similar trend is observed during testing,

as shown in Fig. 4.25, where MAE values range from 2.63 mm (Table Transverse) to 4.67 mm (C-arm Horizontal).

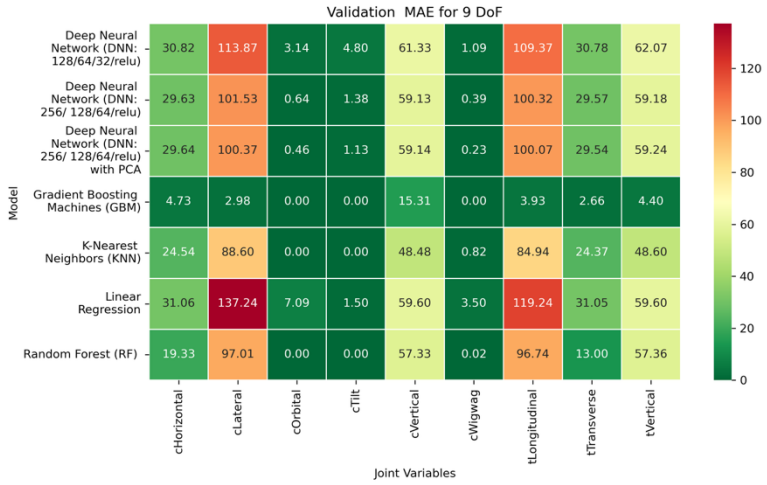

Figure 4.24: Heatmap of Validation Set. Mean Absolute Error for Inverse Kinematics ML.

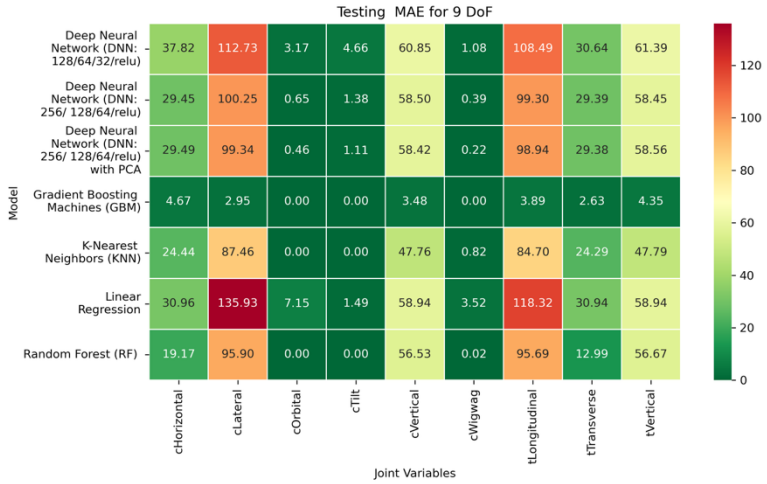

Figure 4.25: Heatmap of Test Set. Mean Absolute Error for Inverse Kinematics ML.

The RMSE results further reinforce these trends, providing deeper insight into the distribution and scale of prediction errors. While Fig. 4.26 – 4.28 present the MSE distributions across training, validation, and testing phases, the corresponding RMSE outcomes are illustrated in Fig. 4.29 – 4.31. For prismatic joints, training RMSE values span from 2.21 mm (Table Transverse) to 4.29 mm (Table Vertical). In the validation set, RMSE increases modestly, ranging from 3.48 mm to 6.24 mm, with the C-arm Horizontal joint again showing the highest deviation. Testing RMSE remains within acceptable bounds, varying between 3.44 mm and 6.18 mm. Notably, all translational errors fall within clinically acceptable thresholds, underscoring the model's applicability for high-precision medical imaging and surgical positioning tasks.

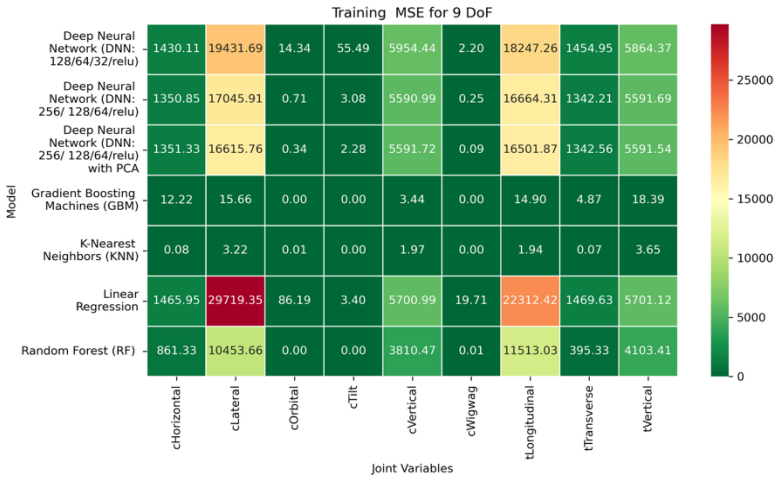

Figure 4.26: Heatmap of Training Set. Mean Square Error for Inverse Kinematics ML.

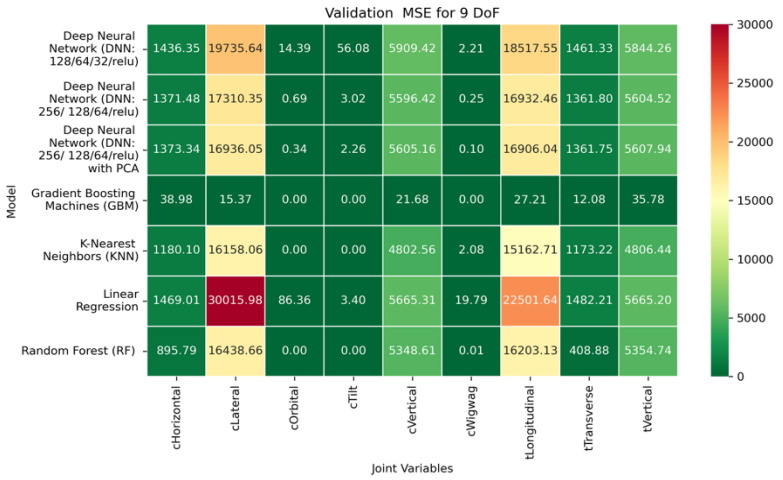

Figure 4.27: Heatmap of Validation Set. Mean Square Error for Inverse Kinematics ML.

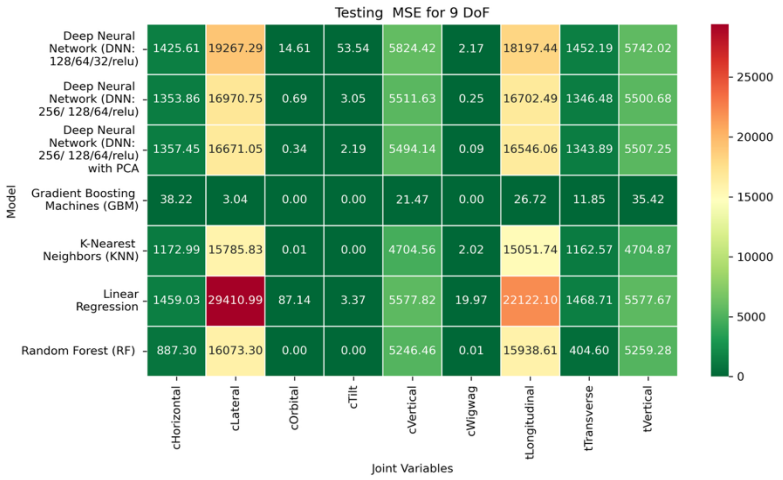

Figure 4.28: Heatmap of Test Set. Mean Square Error for Inverse Kinematics ML.

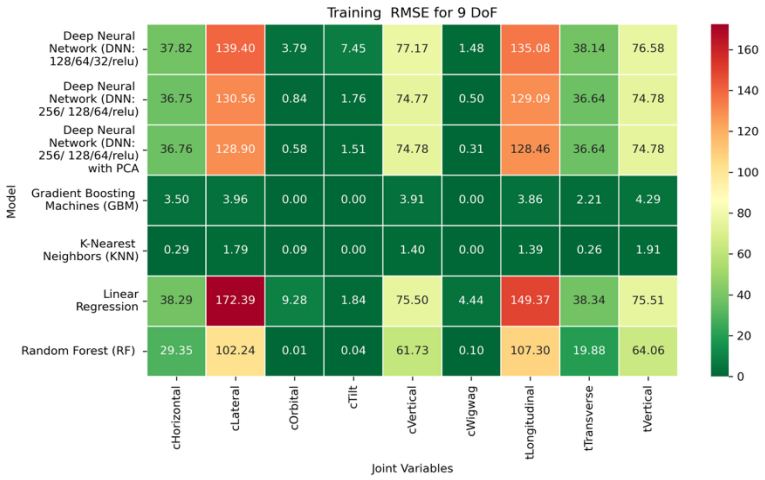

Figure 4.29: Heatmap of Training Set. Root Mean Square Error for Inverse Kinematics ML.

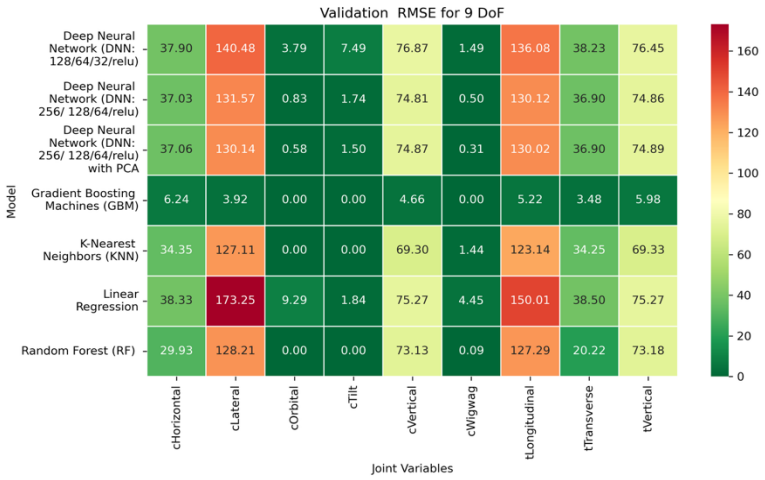

Figure 4.30: Heatmap of Validation Set. Root Mean Square Error for Inverse Kinematics ML.

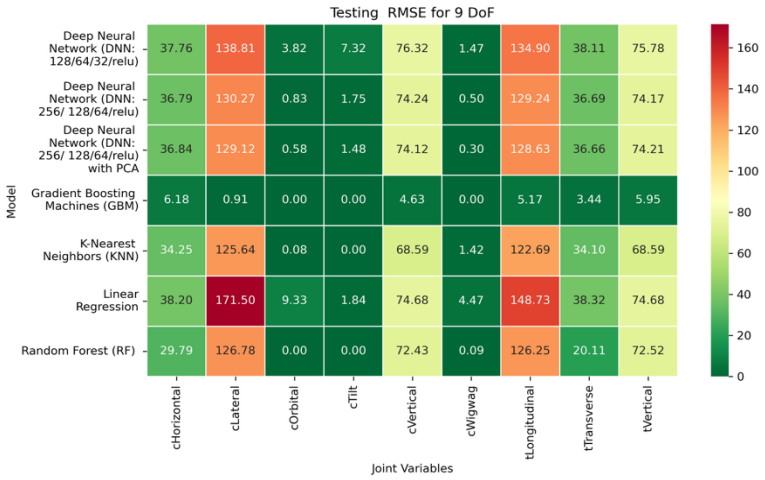

Figure 4.31: Heatmap of Test Set. Root Mean Square Error for Inverse Kinematics ML.

Regarding variance explanation, the coefficient of determination results, as depicted in Figs. 4.32 – 4.34, further validate the predictive robustness of the GBM model. As shown in Fig. 4.32, GBM achieves an R^2 score of 1.00 for all rotational joints in the training phase, affirming its perfect fit across all angular components. For translational joints, training R^2 values range from 0.88 (C-arm Horizontal) to 0.99 (Table Transverse). In the validation phase, illustrated in Fig. 4.33, a moderate decline in predictive performance is observed, with R^2 values spanning 0.61 to 0.88. The testing phase results presented in Fig. 4.34 shows a similar distribution, reinforcing the model's consistency across unseen data. Notably, the C-arm Horizontal joint characterized by an extensive motion envelope and nonlinear inter-axis dependencies consistently yields the lowest R^2 scores, underscoring its higher representational complexity and increased difficulty in generalization.

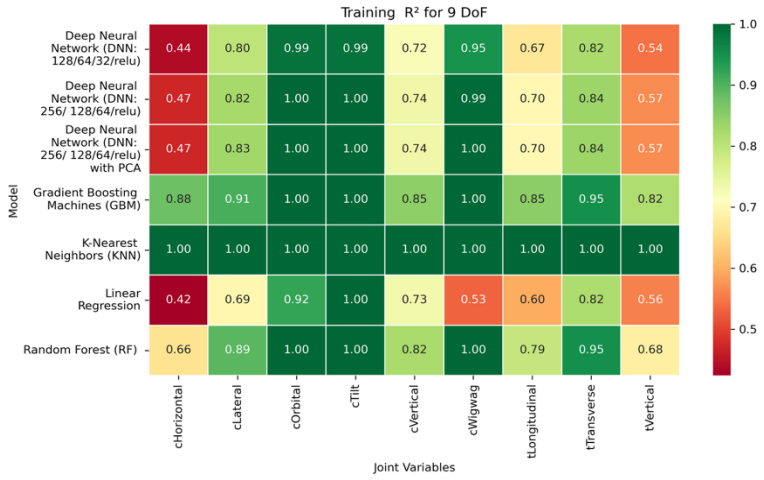

Figure 4.32: Heatmap of Training Set. Coefficient of Determination for Inverse Kinematics ML.

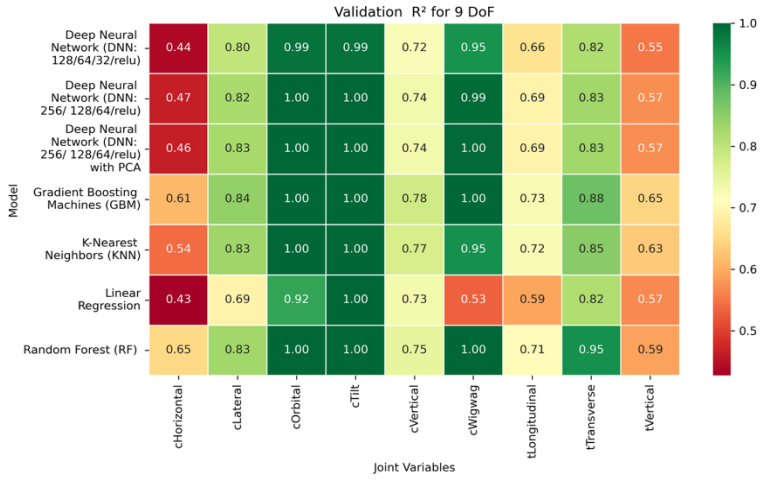

Figure 4.33: Heatmap of Validation Set. Coefficient of Determination for Inverse Kinematics ML.

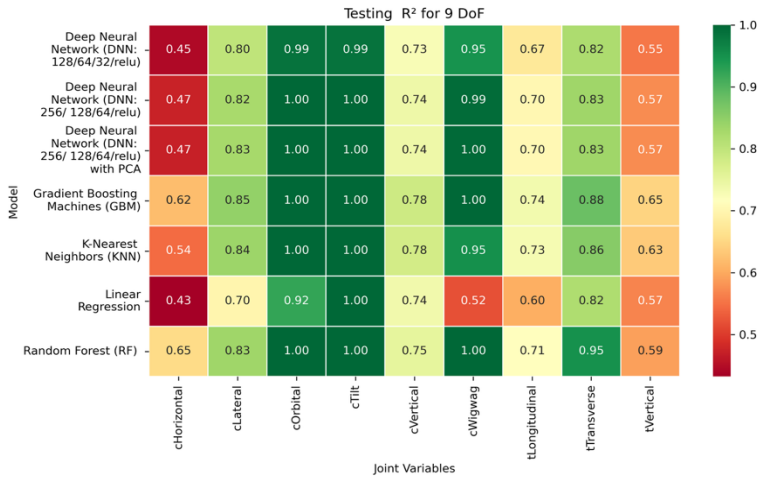

Figure 4.34: Heatmap of Test Set. Coefficient of Determination for Inverse Kinematics ML.

The GBM model demonstrates exceptional predictive accuracy for revolute joints and robust performance for prismatic joints, with sub-millimeter to low-millimeter error margins across datasets. These results position GBM as a highly effective, data-driven solution for inverse kinematics in modular C-arm systems. Its ability to generalize across diverse joint types makes it particularly well-suited for integration into real-time control systems and AI-assisted surgical trajectory planning frameworks, advancing the state of intelligent medical robotics.

The Predicted vs. True joint outputs on the test set are illustrated in the Appendix 3 Fig. 6.1– 6.7 for all nine joints under the 9-DoF configuration, offering a temporal comparison across 100 representative samples. These plots provide a clear visual interpretation of each model's fidelity in approximating the joint trajectories. The tight tracking of prediction lines to the true values in these plots reinforces the quantitative findings from MAE, RMSE, and R^2 analyses. Conversely, any observable phase shift, amplitude discrepancy, or increased oscillation between predicted and true lines in specific joints offers valuable insight into joint-specific limitations and opportunities for further model refinement.

Due to the exhaustive nature of the evaluation, and for brevity, we have included all results using ML on both forward and inverse kinematics, from 5DoF to 9DoF in Appendix 4.

4.3.3 Baseline Comparison with Analytical and Numerical Solvers

To establish a rigorous baseline for the machine-learning (ML) predictions, comparisons were performed against the analytical and numerically validated solvers developed in our prior work [157] . In that study, the forward kinematics of the isocentric C-arm with patient table were formulated analytically using the Denavit–Hartenberg (DH) parameter method providing a closed-form expression for the end-effector transformation matrix T_{ee}^{base}. The analytical results were subsequently validated numerically using a high-fidelity Simscape Multibody solver, where thousands randomly generated joint configurations were

simulated to compute end-effector poses. The rotational outputs were expressed in quaternion form (q_w, q_x, q_y, q_z) and the translational components as (t_x, t_y, t_z). Comparative analysis between the analytical and numerical results revealed zero rotational and translational error, confirming the deterministic accuracy of the DH-based analytical formulation and validating the Simscape solver as a reliable numerical reference. In the present study, these validated analytical-numerical results served as ground-truth baselines for assessing the accuracy of the ML regression models developed for the 9DoF C-arm system. The quaternion data from both input and output datasets were converted to Euler angles (r_x, r_y, r_z) to align with the pose representation used in the ML framework. As summarized in Table 4.5, the numerical comparison between the analytical and numerical solvers exhibited negligible orientation deviations, with both the mean absolute error (MAE) and root mean square error (RMSE) effectively equal to zero degrees confirming complete rotational consistency between the two formulations; translational discrepancies remained sub-millimetric with RMSE values of 0.00282 mm, 0.00438 mm, and 0.00845 mm along the x, y, and z axes respectively. While baseline errors for lower DoF modular configurations (5 to 8 DoF) have been comprehensively presented in earlier work [157], the present validation confirms that the extended 9DoF C-arm system architecture preserves geometric fidelity and orientation precision across all degrees of freedom.

Table 4.5: Baseline validation between analytical and numerical solvers for the 9-DoF C-arm system.

Metrics	r_x	r_y	r_z	t_x	t_y	t_z
MAE	0	0	0	0.00026	0.00314	0.00340
RMSE	0	0	0	0.00282	0.00438	0.00845

By incorporating both analytical and numerical baselines, the study establishes a rigorous foundation for verifying the accuracy, stability, and generalizability of the proposed data-driven framework. The analytical DH-based formulation provides a deterministic and interpretable reference for kinematic relationships, while the numerical solver ensures high-fidelity validation under realistic multibody dynamics and computational perturbations. Together, these baselines confirm that the model preserves both geometric exactness and physical consistency across all degrees of freedom. Among all machine learning models evaluated in this study, the Gradient Boosting Machine (GBM) and the Deep Neural Network (DNN) integrated with Principal Component Analysis (PCA) most effectively replicated the deterministic DH-based analytical formulation, achieving near-perfect correspondence with the validated numerical solver. These models extend the applicability of the analytical baseline to complex and redundant clinical workspaces where closed-form solvers become computationally prohibitive. This dual validation

underscores the numerical fidelity, physical interpretability, and scalability of the GBM- and DNN-based machine learning framework for advanced C-arm kinematic modeling.

4.3.4 Robustness Analysis with Perturbed Inputs

Among the five evaluated regression models: Ridge Regression, K-Nearest Neighbors, Random Forest, Gradient Boosting Machine (GBM), and Deep Neural Network (DNN), the GBM consistently achieved near-zero error and a perfect coefficient of determination ($R^2 \approx 1.0$) across all pose components of 9DoF C-arm system. Although this accuracy highlights its strong learning capability, it also warrants verification against possible overfitting or data-leakage artifacts. Therefore, robustness evaluation was performed exclusively for the GBM, as its ensemble-boosting architecture is particularly sensitive to distributional shifts. Assessing GBM under noisy and perturbed inputs provides the most stringent diagnostic of the framework's numerical stability and generalization strength.

To emulate real-world uncertainties arising from encoder drift, sensor noise, and mechanical backlash, additive Gaussian perturbations were introduced into the standardized test features:

$$X_{noisy} = X_{test} + \mathcal{N}(0,\ \sigma^2) \qquad (4.1)$$

with $\sigma \in \{0.01, 0.05, 0.10\}$ representing low, moderate, and high perturbation levels. Each perturbed dataset was scaled using the same normalization parameters derived from the training subset to avoid leakage. For each σ level, the model's predictions were compared with ground-truth pose values using Mean Absolute Error (MAE), Root Mean Square Error (RMSE), and Coefficient of Determination (R^2).

Fig. 4.35- 4.37 illustrate the variation of MAE, RMSE, and R^2, respectively, as a function of σ across the six pose components: three rotational (r_x, r_y, r_z) and three translational (t_x, t_y, t_z). At minimal perturbation ($\sigma = 0.01$), the GBM maintained near-perfect performance (MAE < 0.01, RMSE < 0.05, $R^2 \approx 1.0$) for all rotational (r_x, r_y, r_z) and translational (t_x, t_y, t_z) components. As σ increased, both MAE and RMSE grew smoothly and linearly, while R^2 declined monotonically yet remained high, indicating a well-conditioned and stable response to noise. The maximum MAE remained below 0.08 and RMSE below 0.6 at $\sigma = 0.10$, corresponding to < 3 % performance degradation well within tolerances.

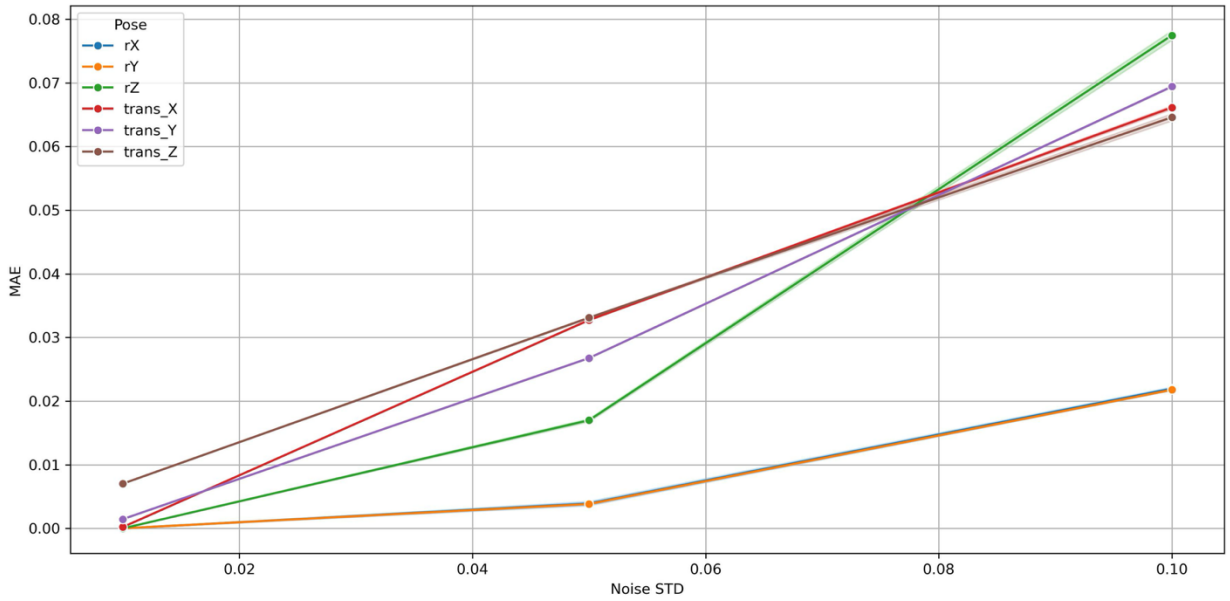

Figure 4.35: Variation of Mean Absolute Error (MAE) with Gaussian noise standard deviation (σ) for the Gradient Boosting Machine (GBM) across six pose components in the 9-DoF configuration.

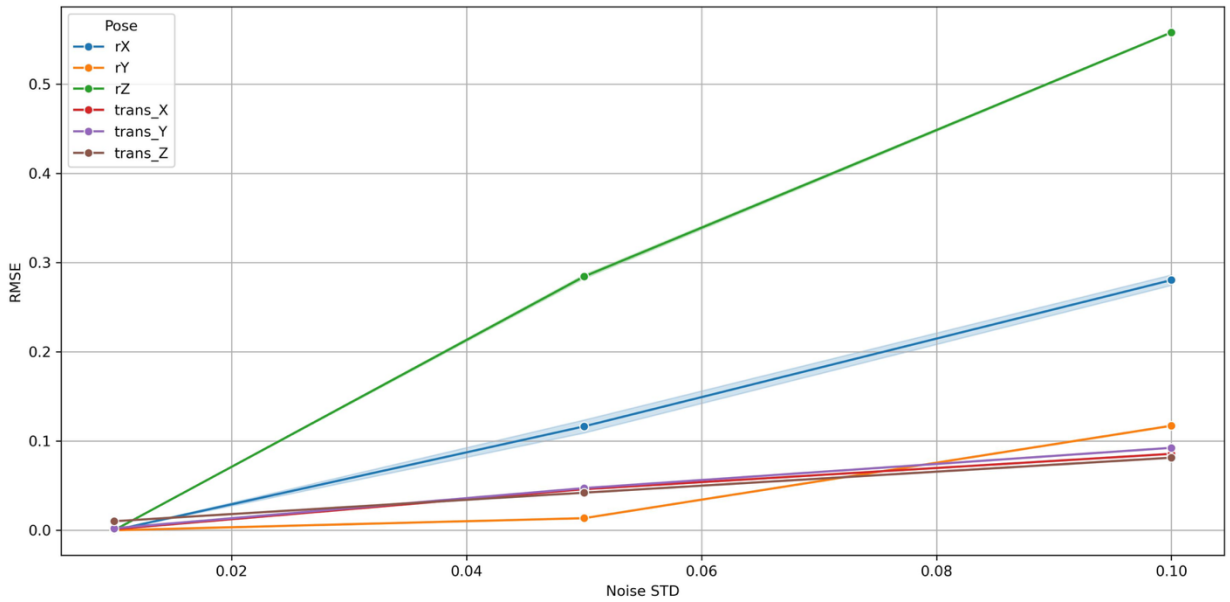

Figure 4.36: Variation of Root Mean Square Error (RMSE) with Gaussian noise standard deviation (σ) for the GBM across six pose components in the 9-DoF configuration. The linear and bounded RMSE growth confirms predictable sensitivity to input perturbations.

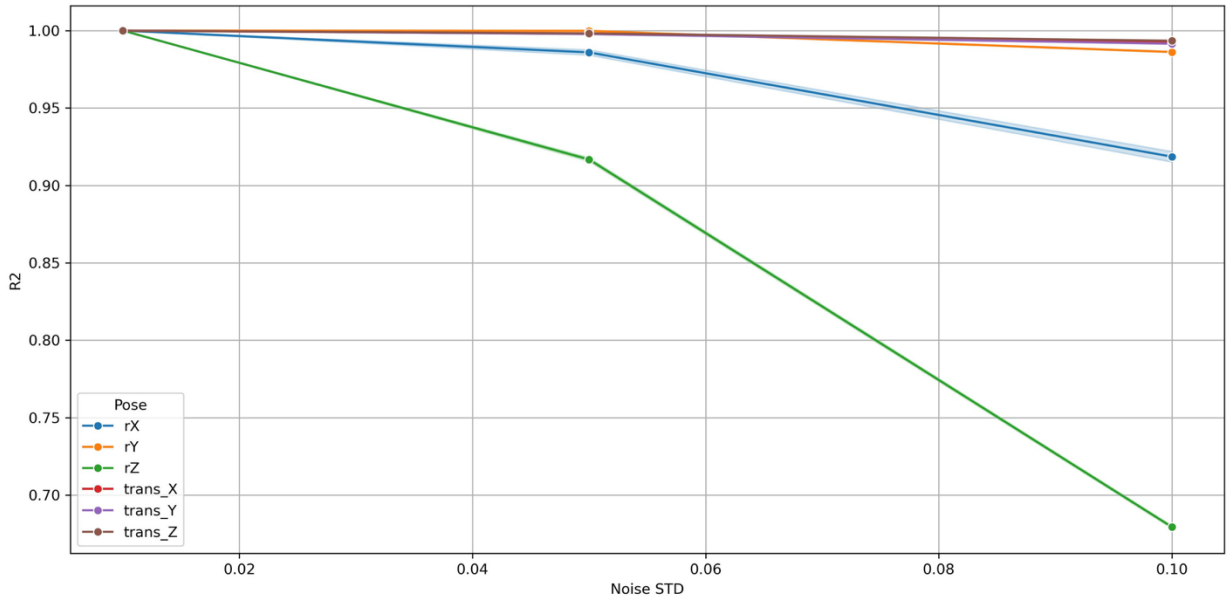

Figure 4.37: Variation of Coefficient of Determination (R^2) with Gaussian noise standard deviation (σ) for the GBM across six pose components in the 9-DoF configuration.

Among rotational variables, r_z showed the steepest sensitivity ($R^2 \approx 0.70$ at $\sigma = 0.10$) owing to its multi-axis coupling with translational joints in the 9-DoF architecture. Conversely, r_x and r_y remained highly stable ($R^2 > 0.90$), exhibiting negligible MAE and RMSE growth. The translational components (t_x, t_y, t_z) maintained $R^2 > 0.98$ for all σ, demonstrating high resilience of prismatic motion estimation.

Collectively, these findings confirm that the GBM is robust, numerically stable, and non-overfitted. Its bounded, linear error progression and absence of abrupt degradation establish the model's capability to sustain accurate predictions under realistic sensor perturbations. This robustness ensures reliable C-arm positioning even with moderate measurement noise, validating the suitability of Gradient Boosting Machine for real-time intraoperative pose prediction and trajectory correction.

4.3.5 Feature Importance and Model Interpretability

To elucidate the internal mechanics of the Gradient Boosting Machine (GBM) and to substantiate the transparency of its predictive behavior, a feature-importance analysis was performed using the Mean Decrease in Impurity (MDI) criterion. This metric quantifies the average reduction in node impurity achieved when a given feature is used for data partitioning across all decision trees in the ensemble, thus serving as an interpretable proxy for each feature's overall contribution to model performance. Higher MDI values correspond to features that induce greater reductions in residual variance and thereby exert stronger predictive influence on the target output. The resulting importance scores were normalized and plotted on a linear scale to preserve the relative magnitudes of contribution across all joint variables.

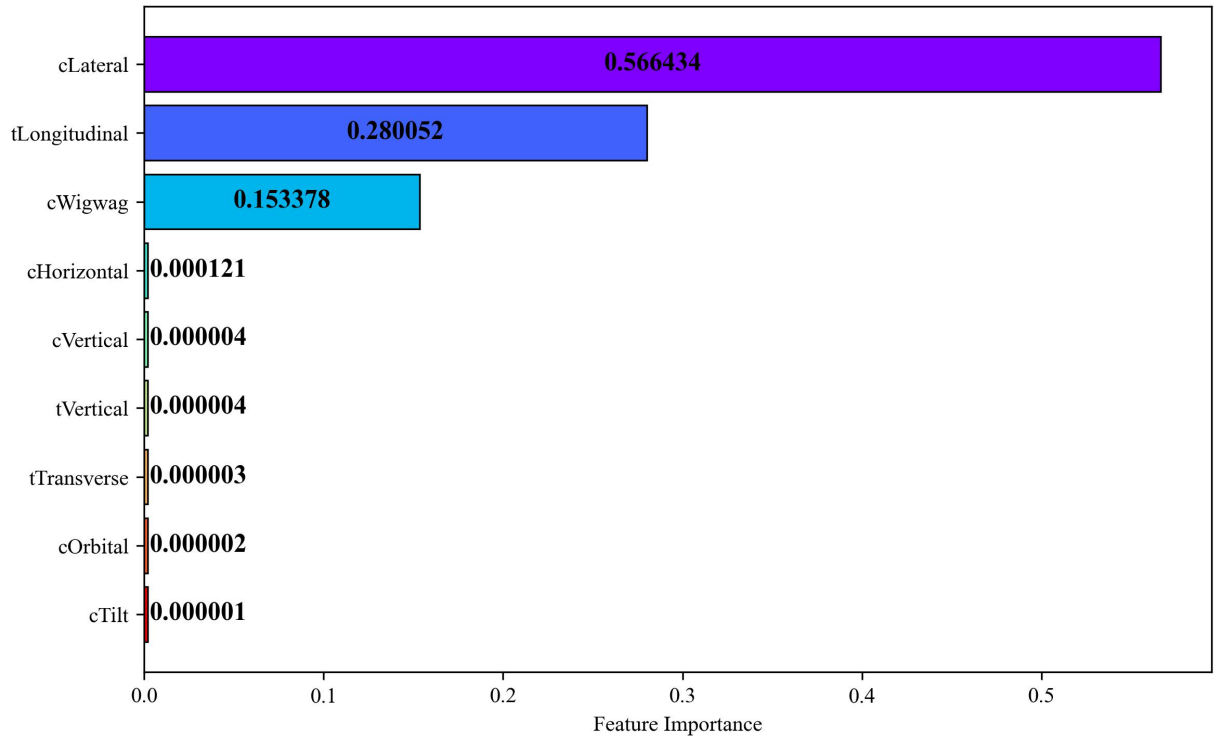

Figure 4.38: Feature importance of joint variables computed using the Mean Decrease in Impurity (MDI) metric.

Each horizontal bar in Fig. 4.38 represents an individual joint variable, color-coded to visually distinguish among features. Numerical annotations on the bars convey the exact MDI values, ensuring quantitative clarity and reproducibility. The visualization reveals a distinct hierarchy in feature relevance: the C-Arm Lateral, Table Longitudinal, and C-Arm Wigwag joints exhibit substantially higher MDI values 0.566, 0.280, and 0.153, respectively demonstrating their dominant influence on end-effector pose prediction. In contrast, the remaining joints possess near-zero importance values indicating negligible contributions to the model's predictive variance.

The analysis revealed that translational joints particularly the C-Arm Lateral, Table Longitudinal, exhibited the highest MDI values underscoring their dominant role in determining spatial alignment within the surgical workspace. In contrast, joints responsible for fine-tuning adjustments displayed lower importances indicating subsidiary contributions primarily associated with local pose refinement. This hierarchy corroborates the predominance of planar and longitudinal translations in defining workspace variability and highlights the capability of the Gradient Boosting Machine to learn physically interpretable motion patterns. By incorporating impurity-based interpretability, the proposed framework extends beyond numerical accuracy to provide transparent insights into the hierarchical structure of learned kinematic dependencies. Such interpretability not only reinforces the model's reliability but also aligns with established variable-

selection methodologies that exploit impurity-reduction indices namely, Mean Decrease Accuracy (MDA) and Mean Decrease Gini (MDG) for feature relevance evaluation [160]. The integration of MDI-based importance analysis thus substantiates the robustness and explainability of ensemble learning in high-dimensional robotic regression tasks.

4.3.6 Post-Prediction Validation Findings

To assess the physical feasibility and safety of the predicted joint configurations, a workspace validation is performed using a simulation-based collision analysis framework in Blender. This step is designed to ensure that the predicted poses not only satisfy kinematic feasibility but also reside within the robot's collision-free operational task space under real-world constraints. In this process, the predicted joint configurations obtained from each machine learning model are applied to the C-arm's 3D kinematic structure modelled in Blender using the *Armature* and *Constraint* system. A Python script executed within the Blender environment systematically samples these joint configurations and forwards them to the robot model. The end-effector poses are then computed and analyzed for collisions with both the robot's own structure and environmental boundaries, leveraging Blender's built-in rigid body physics engine for precise detection.
Table 4.6 reports the percentage of predicted configurations that successfully fall within the collision-free workspace, across various DoF reductions. For the full 9DoF configuration, 100% workspace validity is achieved across all models, confirming the physical plausibility of learned solutions. As dimensionality is reduced, slight degradation in workspace coverage is observed for a few models – most notably at 5DoF, where linear regression and tree-based models such as RF and GBM drop to 99.48% and 99.82% respectively. Conversely, deep neural networks, particularly the DNN with PCA, maintain 100% validity even in underactuated conditions.

Table 4.6: Percentage of collision-free poses across machine learning models for 5DoF to 9DoF configurations.

Configuration	Linear Regression	Gradient Boosting Machine (GBM)	K-Nearest Neighbor (KNN)	Random Forest (RF)	Deep Neural Network (DNN-128-64-32)	Deep Neural Network (DNN-256-128-64)	Deep Neural Network (DNN-256-128-64) with PCA
9DoF	100%	100%	100%	100%	100%	100%	100%
8DoF	100%	100%	100%	100%	100%	100%	99.99%
7DoF	99.99%	99.99%	100%	100%	100%	100%	100%

6DoF	99.99%	99.99%	100%	99.99%	100%	100%	100%
5DoF	99.41%	99.48%	99.82%	99.48%	100%	99.82%	100%

4.3.7 Computational Cost and Runtime Analysis

To evaluate computational efficiency and assess real-time feasibility, a comprehensive runtime analysis was conducted for the two most accurate models Gradient Boosting Machine (GBM) and Deep Neural Network (DNN) with PCA applied to the 9-DoF C-arm with operating table configuration. This configuration was deliberately selected because it represents the maximum kinematic complexity within the modular system, combining a 6-DoF enhanced C-arm with a 3-DoF surgical table. As the highest-order model, it encapsulates the complete set of translational and rotational couplings, redundancy, and nonlinear dependencies inherent to the integrated architecture. Evaluating computational cost under this scenario therefore provides a conservative upper bound on runtime and scalability, ensuring that all lower-DoF configurations would entail proportionally lower computational requirements.

The computing environment and framework specifications are provided in Section III.F (System Configuration and Training Methodology). Each pose component three rotational (r_x, r_y, r_z) and three translational (t_x, t_y, t_z) was trained and validated independently under identical hardware and software conditions to ensure methodological uniformity.

Table 4.7: Empirical Runtime Analysis of GBM and DNN Models under Identical Computational Settings for the 9-DoF Configuration.

Pose	Runtime of Deep Neural Network with PCA (min: sec)	Runtime of Gradient Boosting Machine (min: sec)
$\mathbf{r_x}$	02:22	09:13
$\mathbf{r_y}$	01:44	07:28
$\mathbf{r_z}$	03:00	09:55
$\mathbf{t_x}$	01:12	12:47
$\mathbf{t_y}$	01:12	12:37
$\mathbf{t_z}$	01:07	12:24

Table 4.7 summarizes the total time, encompassing the training, validation, and robustness evaluation phases for both Gradient Boosting Machine and Deep Neural

Network with PCA. Although the two architectures achieved similar predictive accuracy, their computational characteristics diverged significantly. The Gradient Boosting Machine model exhibited longer training durations due to its sequential additive boosting process, wherein each weak learner (decision tree) is iteratively fitted to the residual errors of preceding learners. Conversely, the Deep Neural Network with PCA leveraged vectorized GPU-accelerated tensor operations for parallelized backpropagation, achieving markedly faster convergence despite having over 100,000 trainable parameters. The cumulative runtime indicates that the DNN with PCA achieved approximately a six-fold speed-up relative to GBM under identical conditions. This improvement arises from the intrinsic parallelizability of neural computations and the exploitation of GPU-based acceleration, in contrast to the inherently serial tree construction of boosting ensembles. Despite the larger parameter count, the DNN achieved faster optimization due to efficient gradient-based learning and adaptive learning-rate scheduling.

Furthermore, inference latency for both architectures remained below 1 millisecond per sample, which is orders of magnitude faster than the mechanical actuation latency of contemporary robotic C-arm systems (typically 10-50 millisecond). These findings confirm that both models satisfy the real-time operational constraints required for intraoperative imaging and trajectory control. While GBM provides enhanced interpretability and robustness to outliers, the DNN offers a superior balance of accuracy, scalability, and computational efficiency, rendering it the most suitable architecture for predictive motion control and real-time pose estimation in modular C-arm systems.

Hence, the reported results for the 9-DoF configuration represent the upper computational bound for all modular architectures considered in this study, ensuring that the proposed framework remains computationally feasible across the full range of system complexities.

4.4 Clinical Implication

The preceding chapters introduced a unified computational framework integrating high-degree-of-freedom (high-DoF) kinematic modelling, collision-aware workspace analysis, dynamic trajectory planning, and machine-learning-based forward and inverse kinematics. Although these components were developed and validated primarily through simulation and data-driven experimentation, their clinical relevance ultimately depends on how variations in C-arm pose affect radiographic image formation. Fluoroscopic imaging is inherently sensitive to the spatial configuration of the X-ray source and detector; therefore, even small deviations in C-arm positioning may lead to perceptible distortions in anatomical structures, altered projection geometry, and reduced visibility of clinically significant landmarks.

To establish a concrete linkage between the computational models and their clinical consequences, this section evaluates the sensitivity of X-ray projections to controlled perturbations in C-arm pose. Digitally Reconstructed Radiographs (DRRs) generated from real patient CT datasets are employed as a surrogate

for clinical fluoroscopic images. Using a standardized perturbation protocol, the C-arm pose is displaced by ±1 mm along each translational axis and rotated by ±1° about the x-axis. The resulting DRRs are compared to baseline projections using feature-based correspondence analysis. This evaluation quantifies how inaccuracies in kinematic modelling, workspace estimation, trajectory execution, or inverse kinematic prediction propagate into visible anatomical deviations. Consequently, the analysis bridges the gap between computational simulation and clinical imaging behavior and provides insight into the practical accuracy requirements for safe and reliable C-arm operation.

4.4.1 DRR-Based Analysis of Positional Sensitivity

Below, four tables present X-ray projections of representative anatomies derived from real patients' CT scans. The projections were obtained using the fast auto differentiable Digitally Reconstructed Radiographs (DRR) method [149]. Each table contains six standard clinical poses, and for each pose, three images are provided:

1. Baseline DRR: X-ray DRR image generated from the original CT scan.
2. Perturbed DRR: X-ray DRR image generated after shifting the C-arm position by 1 mm along each of the x, y, and z axes and applying a 1° rotation about the x-axis, relative to the baseline image.
3. Key-point visualization: Key points extracted from images (1) and (2) and matched using the Scale-Invariant Feature Transform (SIFT) algorithm [150]. For clarity, key points from image (1) are overlaid on image (2) with "+" markers, and corresponding pairs are connected by lines, thus illustrating the displacement of anatomical features under the imposed 1 mm and 1° perturbation in C-arm positioning.

Key-point extraction and matching were performed using the Scale-Invariant Feature Transform (SIFT) implementation in the OpenCV Python library (version 4.11) [151]. Correspondence pairs were visualized by projecting the baseline key-points onto the perturbed DRR and connecting matched pairs with line segments. These correspondences highlight the magnitude and distribution of structural displacement induced by small pose perturbations. Across all anatomical regions, the analysis demonstrates that millimetric and sub-degree variations representative of realistic mechanical tolerances or IK prediction errors lead to noticeable misalignment of vertebrae, vascular bifurcations, cortical boundaries, and pelvic landmarks. This quantification provides an empirical measure of the positional accuracy required to preserve anatomical fidelity in fluoroscopic imaging.

- Table 4.8: Upper body anatomy, CT scan from the *TotalSegmentator* dataset [152].
- Table 4.9: Thorax region, example CT scan from [149].
- Table 4.10: Cerebrovasculature anatomy, dataset from University Medical Center Ljubljana [153].
- Table 4.11: Pelvis anatomy, *DeepFluoro* dataset [154].

Table 4.8: Upper body anatomy.

Clinical pose	Ground Truth	DRR image shifted and rotated	Key points comparison
AP			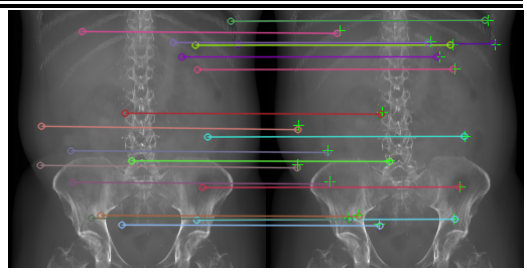
PA	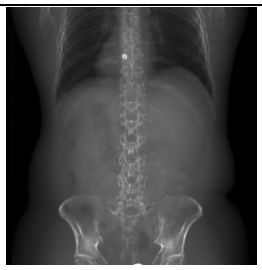	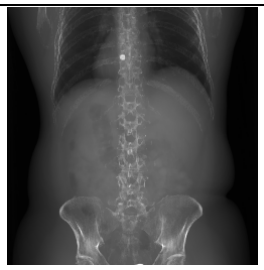	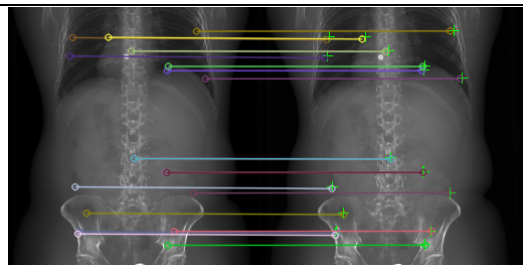
V1			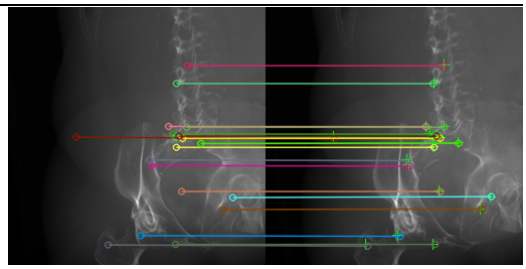
V2			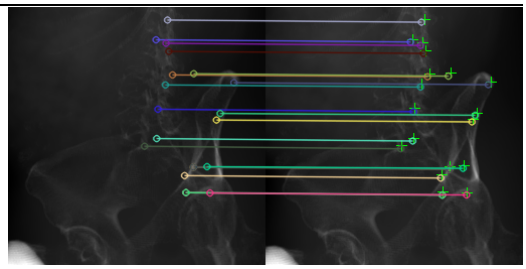
Ver			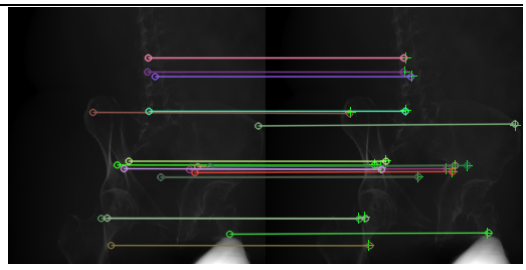

Lat			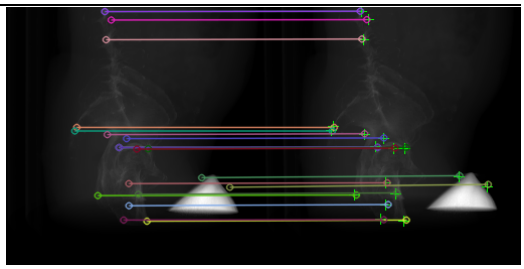

Table 4.9: Thorax anatomy.

Clinical pose	Ground Truth	DRR image shifted and rotated	Key points comparison
AP			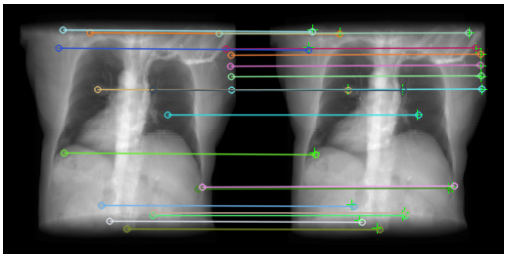
PA			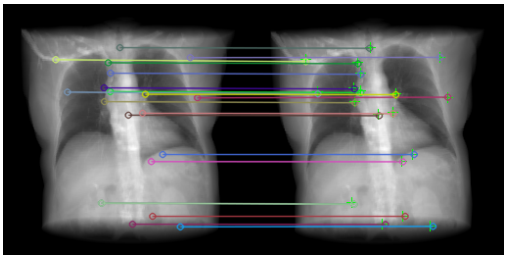
V1	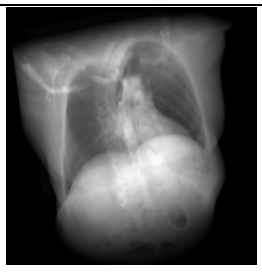	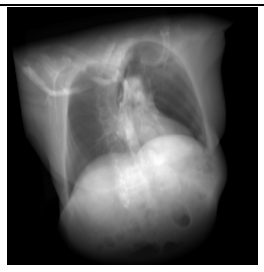	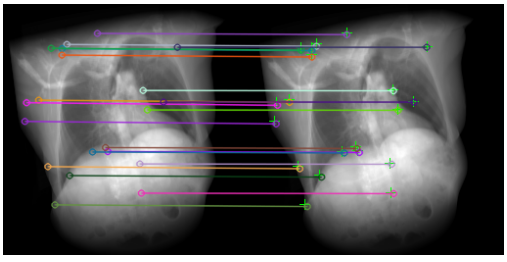

V2	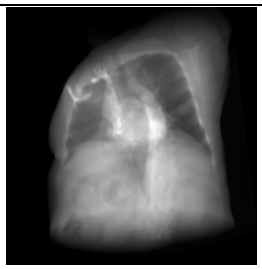	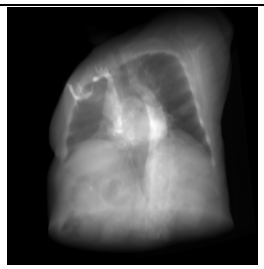	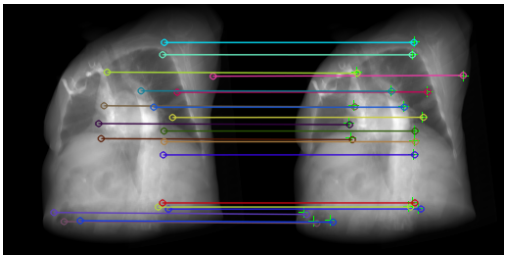
Ver		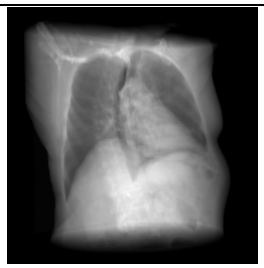	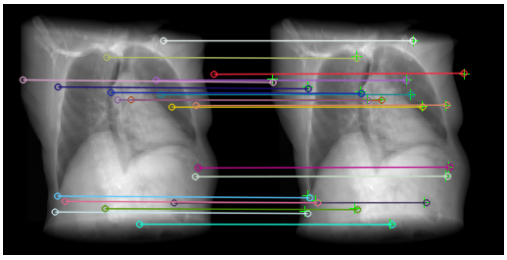
Lat	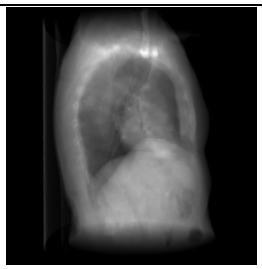	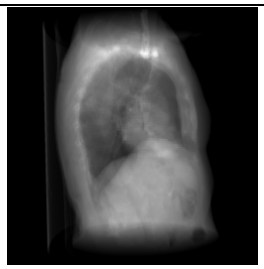	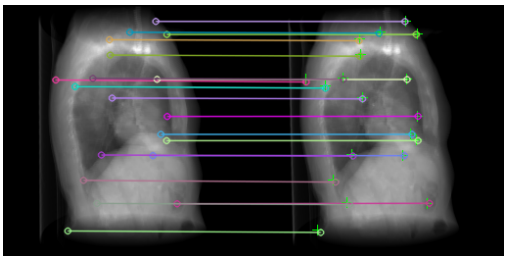

Table 4.10: Cerebrovasculate anatomy.

Clinical pose	Ground Truth	DRR image shifted and rotated	Key points comparison
AP	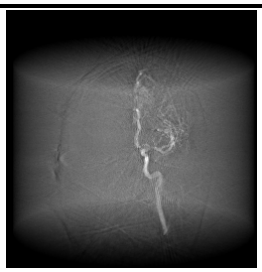	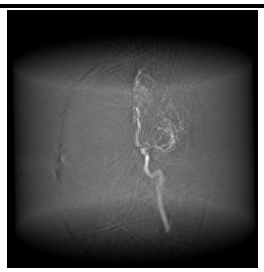	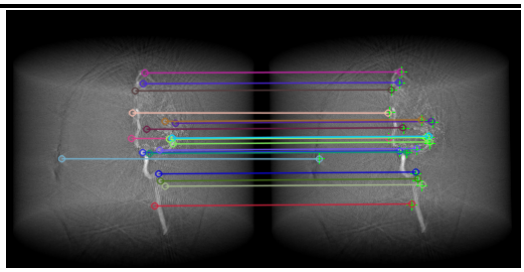
PA	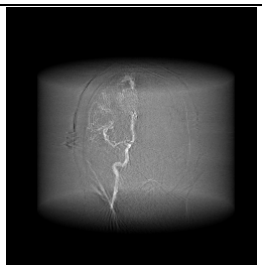	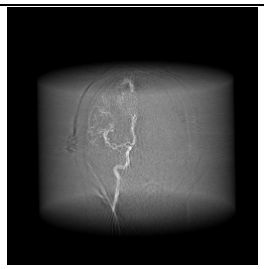	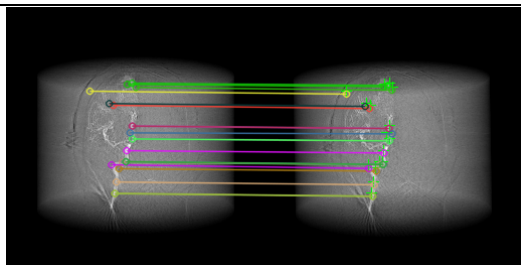

V1			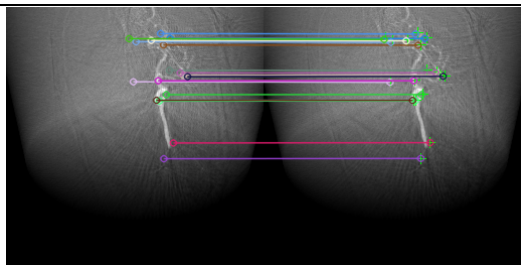
V2	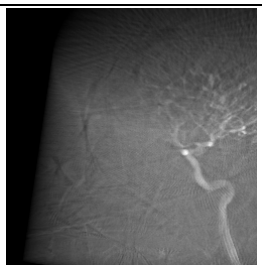	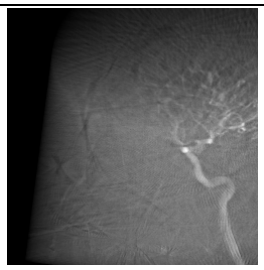	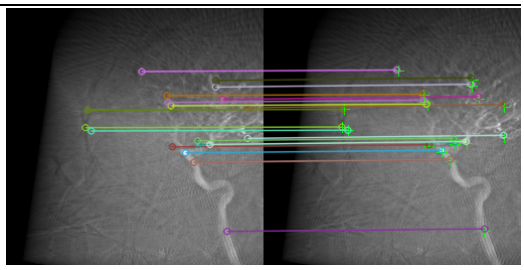
Ver	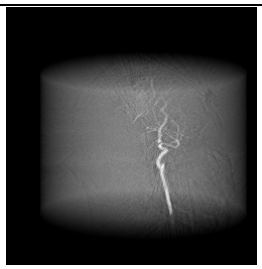	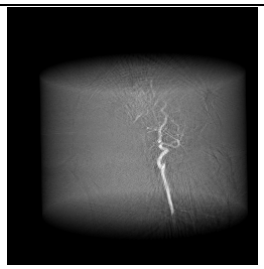	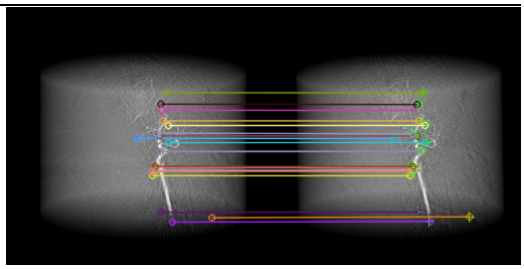
Lat	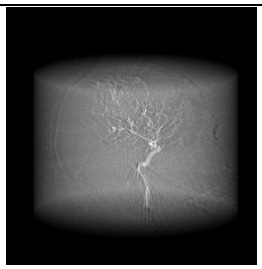	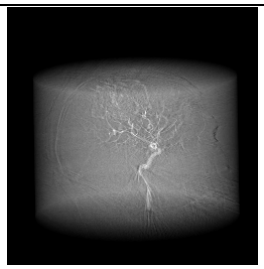	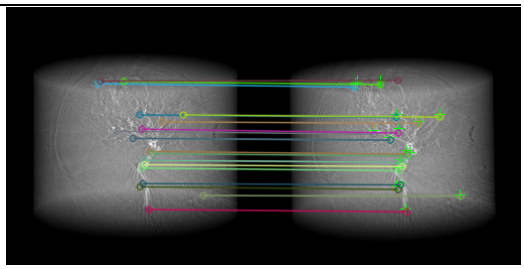

Table 4.11: Pelvis Anatomy.

Clinical pose	Ground Truth	DRR image shifted and rotated	Key points comparison
AP			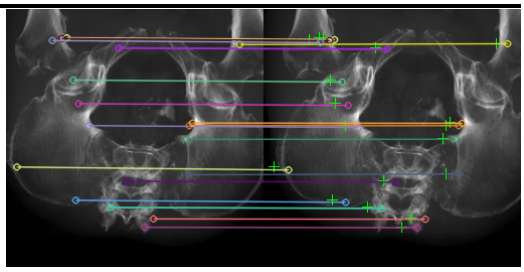

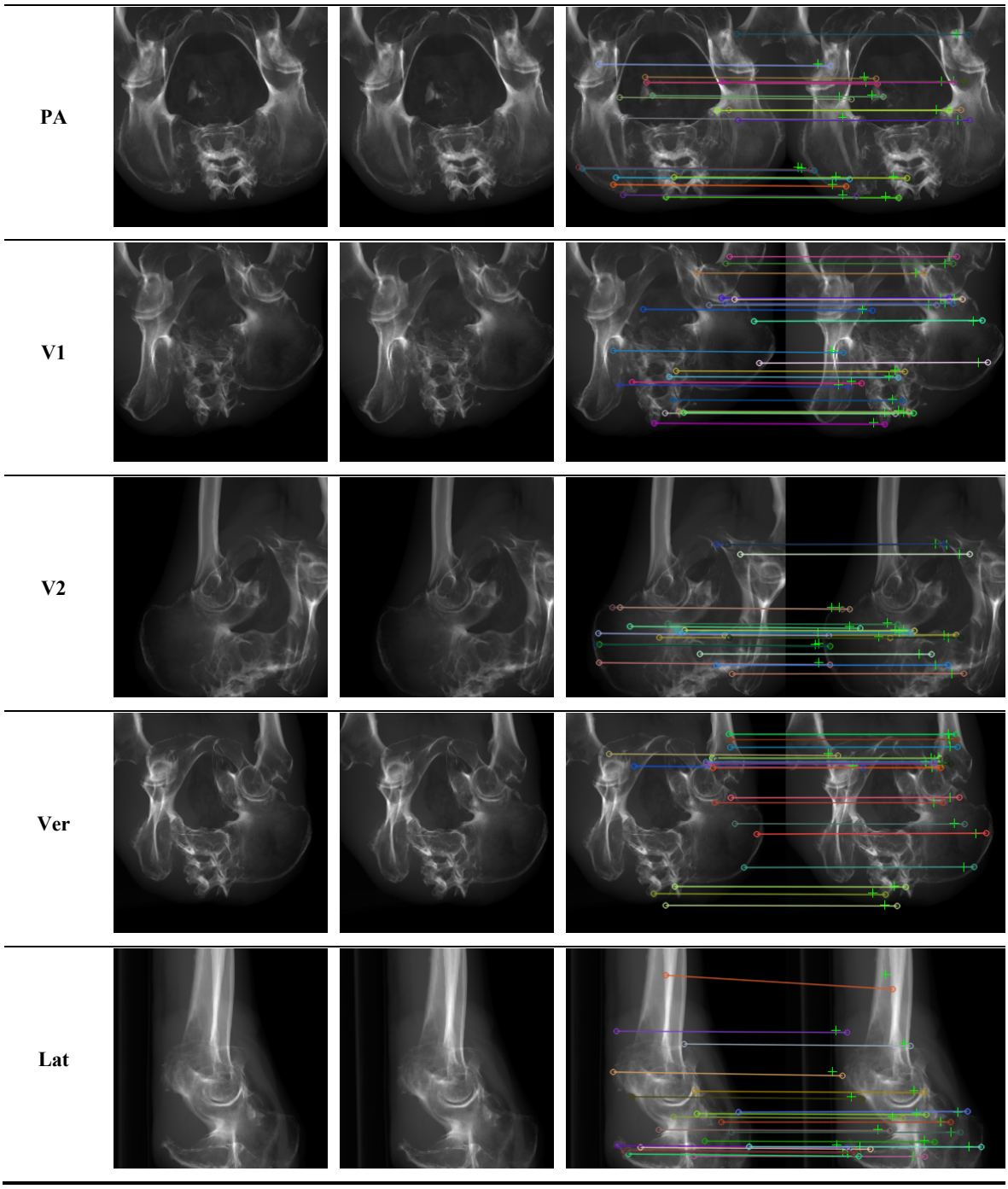

4.4.2 Linking DRR Sensitivity to the Methods Developed in This Thesis

The DRR sensitivity results are not independent observations; rather, they directly substantiate the necessity of the modelling, planning, and learning components developed throughout the thesis.

First, the observed anatomical displacements confirm the importance of high-DoF kinematic modelling. The 9-DoF C-arm and table configuration accurately captures the full range of clinically required motions and mitigates the risk of image degradation due to insufficient angular or translational reach. In contrast,

lower-DoF models, such as the 5 or 6-DoF systems evaluated in prior literature, are unable to satisfy the pose requirements for several essential oblique and cranial/caudal projections. The DRR results demonstrate that inadequate DoF does not merely restrict reachability; it compromises image quality by preventing precise alignment of X-ray source, detector, and anatomy.

Second, the sensitivity analysis reinforces the relevance of collision-aware workspace computation. The clinical projections used in the DRR study: AP, LAT, PA, V1, V2, and VER are only achievable when the C-arm can maneuver within the anatomical environment without colliding with the patient table or surrounding hardware. If the workspace limits identified in Chapters 2 and 3 are violated, the system cannot obtain the appropriate view angles even if IK solutions exist. The feature displacements seen in perturbed DRRs underscore that small errors in angulation or patient to C-arm distance directly influence radiographic quality. Therefore, accurate workspace mapping is fundamental to ensuring that clinically essential projections are physically attainable.

Third, the perturbation study validates the need for smooth and dynamically feasible trajectory planning. Since fluoroscopic imaging is conducted during continuous C-arm movement, abrupt accelerations or imprecise joint coordination can introduce millimetric deviations at the imaging plane. The DRR results illustrate that such small perturbations yield measurable differences in anatomical alignment. The optimized trajectories evaluated in Section 4.2 particularly minimum jerk and high-order polynomial profiles are therefore justified as essential to maintaining imaging accuracy while minimizing interventional time.

Finally, the results directly support the necessity of reliable machine-learning-based inverse kinematics. The DRR displacements depict the consequences of even small Inverse Kinematic prediction errors on clinical image formation. As shown in Chapter 4, the machine learning models achieve sub-millimetric and sub-degree prediction accuracy. The DRR findings confirm that such precision is necessary to maintain anatomical consistency, especially in complex projections such as V1, V2, and vertebroplasty, where oblique visualization depends critically on precise pose control. The DRR comparisons therefore serve as an image-based validation of the accuracy requirements for ML-driven Inverse Kinematic solutions.

4.4.3 Summary of Clinical Implication

The DRR-based perturbation analysis demonstrates that fluoroscopic projections are acutely sensitive to small pose variations, with 1 mm or 1° perturbations producing noticeable distortions of clinically significant anatomical features. These results validate the modelling accuracy, workspace feasibility, trajectory smoothness, and Kinematic precision targeted throughout this thesis. Collectively, the findings emphasize that intelligent C-arm positioning systems must maintain strict pose fidelity to ensure safe catheter navigation, minimize radiation exposure, and consistently produce diagnostically reliable images.

The proposed framework lays the computational foundation for future autonomous or semi-autonomous C-arm systems capable of achieving these requirements in real clinical environments.

4.5 Clinical Validation and Path Toward Physical Validation

The proposed machine-learning framework is inherently designed for unified integration into clinical C-arm fluoroscopy workflows and for future deployment on physical hardware platforms. All simulations were executed under strict mechanical range-of-motion constraints, reflecting the translational and angular limits (in meters and degrees) of commercially available C-arm and operating table systems. These parameters were derived from the manufacturer specifications of GE Healthcare and STERIS, ensuring that every simulated configuration remains mechanically feasible and directly reproducible on real devices.

While simulation-based validation confirmed that all predicted joint configurations remained within collision-free and kinematically feasible regions, the transition from virtual evaluation to clinical implementation necessitates careful consideration of hardware-specific dynamics and calibration fidelity. In practice, positioning inaccuracies in C-arm fluoroscopy arise primarily from device-level factors rather than anatomical deformation. These include encoder quantization, mechanical backlash, hysteresis, and constraints in smooth control of velocity, acceleration, and jerk, which can introduce minor positional drift of the imaging gantry during prolonged procedures or repeated articulations. Accordingly, the simulation environments in this study were explicitly constrained by manufacturer-defined motion limits for both the GE OEC 3D C-arm and the STERIS CMAX™ X-ray operating table. By enforcing these bounds, the generated datasets reflect mechanically realizable trajectories that can be executed by current clinical systems without violating operational constraints.

Modern C-arm fluoroscopes already incorporate quasi-automatic image-distortion correction and continuous geometric calibration routines that substantially mitigate hardware-induced errors. Residual drift, when present, typically stems from long-term mechanical wear, gravitational sag and so on. Contemporary interventional protocols address these residual errors through virtual-fluoroscopy systems that employ 2D/3D CT X-ray registration overlays. In such frameworks, preoperative CT volumes are aligned with intraoperative X-ray images by synthesizing Digitally Reconstructed Radiographs (DRRs) and iteratively optimizing projection geometry to minimize misalignment. This process provides an accurate, real-time estimation of the C-arm's 3D pose, thereby compensating for both calibration offsets and mechanical deviations.

The present study directly builds upon these clinically validated practices. In prior investigations by Jaheen *et al.* [157-158], DRR-based registration pipelines were applied for validating datasets in multiple clinical

projections to assess the geometric fidelity of simulated C-arm poses. The DRR-based validation confirmed sub-millimeter alignment between reconstructed and acquired fluoroscopic projections, thereby demonstrating that the simulated kinematics faithfully reproduce real device behavior. The current machine-learning framework extends this foundation by learning kinematic mappings exclusively from datasets generated within these experimentally validated motion envelopes, ensuring both physical realism and clinical consistency. The integration of DRR-based registration within the proposed workflow is further supported by contemporary advancements in 2D/3D registration algorithms [35], [147-148], which collectively reinforce the methodological continuity between simulation and clinical imaging systems.

Although direct hardware experimentation falls outside the present study's scope, the proposed models are readily compatible with existing C-arm calibration and tracking infrastructures. The predicted joint configurations can serve as data-driven pose priors that initialize or accelerate registration-based tracking pipelines, improving computational efficiency during intraoperative alignment. Moreover, once trained on empirical device data, the framework could function as a real-time predictive controller, continuously refining pose trajectories to ensure smooth, collision-free motion under mechanical and safety constraints.

A future hardware-in-the-loop validation environment is envisioned, wherein the predicted trajectories will be executed on a physical C-arm system and compared against encoder feedback and optically tracked end-effector poses. Such experiments will quantitatively assess the framework's robustness to encoder noise, mechanical backlash, and actuation nonlinearity. In this regard, the proposed methodology not only bridges the gap between simulation-driven modeling and clinical translation but also establishes a scalable foundation for intelligent C-arm systems capable of real-time pose prediction, adaptive trajectory planning, and drift compensation in image-guided minimally invasive surgery. The outlined validation pathway provides a rigorous and technically feasible roadmap to transition from simulation-based development toward hardware-grounded, clinically viable implementation.

Chapter 5 : Conclusion

5.1 Restatement of the Research Problem and Aim

Minimally invasive surgery has undergone a paradigm shift in recent decades, marked by an unprecedented escalation in procedural complexity and an unwavering demand for surgical precision. This trend has propelled the adoption of advanced intraoperative imaging systems, which are now integral to surgical workflows across disciplines ranging from orthopedics to interventional cardiology. Within this context, the C-arm fluoroscope, an indispensable modality for real-time radiographic guidance, occupies a central role. However, despite its ubiquity, the conventional C-arm suffers from two fundamental limitations: restricted mechanical degrees of freedom and the absence of intrinsic, algorithmically integrated motion planning capabilities.

These limitations manifest clinically in three ways. First, they hinder optimal positioning for multiple, sequential clinical projections, leading to repeated manual adjustments that disrupt workflow continuity. Second, they prolong setup time, which can be detrimental in high-acuity environments. Third, they increase the risk of geometric suboptimality in imaging, potentially compromising diagnostic clarity and procedural safety. A further systemic impediment lies in the paucity of expansive, collision-free, and clinically validated datasets for modular C-arm systems. The scarcity of such data precludes the scalable application of advanced optimization techniques and machine learning-based positioning strategies in real-world surgical environments. Without a robust corpus of representative positional data, algorithmic pose prediction and intelligent trajectory generation remain largely theoretical. Hence, such datasets are indispensable for the application of data-driven optimization and intelligent positioning strategies both of which are emerging as key enablers in the future of surgical robotics and image-guided intervention.

Accordingly, the primary objective of this research was the development of an end-to-end, unified methodology encompassing kinematic modelling, workspace analysis, trajectory planning, and machine learning-driven pose prediction for modular C-arm systems integrated with operating tables. The central aims were threefold:

1. Dataset Generation: Created clinically validated, large-scale, collision-free pose datasets for multiple modular C-arm configurations.
2. Trajectory Planning: Developed and benchmarked diverse trajectory generation strategies for smooth, efficient, and accurate transitions between canonical clinical projections.
3. Machine Learning Prediction: Implemented and optimized machine learning architectures capable of predicting joint configurations from desired end-effector poses with clinically acceptable precision thresholds.

Through the synergistic integration of these components, the research sought not merely to solve an engineering problem, but to pioneer a scalable computational framework with direct translational impact in surgical imaging practice. Furthermore, this research sought to bridge the gap between deterministic kinematic modelling and data-driven predictive control, creating a modular, extensible architecture with both immediate clinical utility and long-term research potential.

5.2 Summary of Key Findings

The research was conducted in three sequential phases, each designed to address an interdependent pillar of the overarching methodological framework.

Phase 1: Workspace Analysis and Collision-Free Dataset Generation

A high-fidelity kinematic model was developed for modular C-arm systems with variable DoFs (5-11), reflecting the mechanical features of the GE OEC 3D C-arm and the STERIS CMAX™ surgical table. This model facilitated forward and inverse kinematics computations, Jacobian-based singularity analysis, and automated collision detection across thousands of simulated poses. Importantly, six canonical clinical projections: Anterior-Posterior (AP), Lateral (LAT), Posterior-Anterior (PA), Vascular 1 (V1), Vascular 2 (V2), and Vertebroplasty (VER) were exhaustively analyzed. The outcome was a comprehensive, collision-free dataset, unprecedented in scale, which not only enables robust trajectory optimization but also constitutes a transferable asset for future machine learning applications in surgical robotics.

Phase 2: Motion Planning and Trajectory Optimization

Four distinct trajectory generation methodologies: *Trapezoidal Velocity Profile*, *Polynomial Trajectory*, *Minimum Jerk Polynomial Trajectory*, and *Minimum Snap Polynomial Trajectory* were implemented within MATLAB Simulink's Joint Space Motion Model environment. Comparative analysis revealed a nuanced trade-off between computational efficiency and motion smoothness:

- *Minimum Jerk* and *Minimum Snap* profiles achieved superior smoothness, critical for delicate intraoperative adjustments where sub-millimetric deviations can be consequential.
- The *Trapezoidal Velocity Profile*, though less smooth, offered computational simplicity and predictable dynamic behavior, making it advantageous in time-critical situations.

To operationalize these findings for clinical use, lookup tables were constructed storing optimized joint parameter configurations tailored to both the projection type and patient-specific constraints. This empowers clinicians to dynamically select motion profiles according to intraoperative priorities, balancing speed, smoothness, and patient safety.

Phase 3: Machine Learning-Based Pose Prediction

Five machine learning architectures: *Linear Regression*, *Gradient Boosting Machines (GBM)*, *K-Nearest Neighbours (KNN)*, *Random Forest (RF)*, and *Deep Neural Networks (DNN)* were trained on the generated datasets to map end-effector pose parameters (translational coordinates and Euler rotations) to the requisite joint configurations. Hyperparameter optimization via Optuna was instrumental in achieving substantial error reduction. Notably, the highest-performing models achieved sub-millimetre translational accuracy and sub-degree rotational accuracy, meeting stringent clinical tolerances.

Crucially, these models demonstrated robust cross-projection generalization, evidencing that the learned mappings are not narrowly task-specific but are adaptable to diverse surgical imaging configurations. This positions the methodology for integration into real-time clinical workflows, where speed and adaptability are paramount.

5.3 Implications for Theory, Practice, and Policy

5.3.1 Theoretical Contributions

This research contributes to the theoretical understanding of robotic imaging systems by extending established formulations of rigid-body kinematics and workspace analysis to integrated and modular interventional imaging systems. The modeling and analysis framework developed in this thesis provides a systematic approach for representing such systems and for evaluating their reachable, collision-free workspaces across varying degrees of freedom. In addition, the proposed methodology for large-scale collision-free dataset generation establishes a generalizable analytical pipeline that can be adapted to other classes of medical robotic systems where workspace feasibility and safety are critical considerations. Finally, by combining deterministic kinematic modeling with supervised machine-learning-based pose prediction, this work contributes to the growing body of research on data-driven kinematics demonstrating how learned models can complement analytical methods for complex, high-DoF systems without replacing underlying physical constraints.

5.3.2 Practical Contributions

From a practical standpoint, this research delivers a set of tools and methodologies that are applicable to clinical and preclinical imaging workflows. The generated lookup tables (LUTs), trajectory planning strategies, and machine-learning-based pose predictors provide a structured means of supporting C-arm positioning under varying system configurations and patient loading conditions. These contributions enable:

- Reduction of pre-procedure setup time through informed selection of feasible trajectories and joint configurations, thereby improving workflow efficiency in the operating room.

- Improved consistency and repeatability of imaging poses with the potential to reduce radiation exposure by limiting unnecessary trial-and-error repositioning.
- A modular and system-agnostic control and planning framework allowing the methodology to be adapted to different C-arm architectures and future imaging platforms without fundamental redesign.

Importantly, these contributions are positioned as decision-support and automation-enabling tools rather than fully autonomous clinical systems, ensuring alignment with current clinical practice and safety requirements.

5.3.3 Policy Implications

Beyond technical contributions, this work has implications for future regulatory and standardization efforts in interventional imaging systems. The proposed dataset generation and validation framework illustrates how collision-aware workspace analysis can be systematically embedded into the design and evaluation of imaging devices. Such methodologies could inform future safety assessment protocols by providing quantitative evidence of reachable, collision-free operational envelopes. Moreover, the integration of C-arm and operating table kinematics highlights the importance of standardized communication and coordination interfaces between imaging systems and auxiliary robotic components. Establishing such standards could facilitate interoperability among imaging hardware, robotic manipulators, and surgical navigation systems supporting the gradual evolution toward more integrated and digitally coordinated surgical environments. While regulatory adoption remains a long-term prospect, the concepts presented in this thesis offer a technically grounded foundation for future discussion in this area.

5.4 Limitations and Scope

While this research delivers a novel and technically rigorous framework with demonstrable promise, it is equally important to recognize its boundaries. Acknowledging these limitations not only contextualizes the reported findings but also provides a realistic foundation for future refinement. The constraints outlined below stem primarily from the transition between controlled simulation environments and the complex, variable nature of real-world surgical practice.

- Simulation-to-Reality Gap: While the motion planning and machine learning frameworks developed in this research were stringently validated within high-fidelity simulation environments, their eventual clinical deployment necessitates a further tier of translational rigor. This transition demands comprehensive hardware-in-the-loop evaluation, seamless integration with proprietary imaging system application programming interfaces (APIs), mitigation of network and control-loop latencies, and compensation for mechanical tolerances as well as

environmental perturbations that remain inherently absent from purely computational models. To partially attenuate this gap, an intermediate validation stage was undertaken using Digitally Reconstructed Radiographs (DRRs) synthetic X-ray projections computationally derived from volumetric CT datasets of real patients across heterogeneous anatomies. Comparative analysis between DRRs and their corresponding ground-truth radiographs demonstrated sub-millimetre translational fidelity and sub-degree rotational congruence, thereby substantiating that the conventional 2D/3D overlay visualisations [35], [147], [155] employed intraoperatively retain clinical veracity within our proposed system. DRRs are not a embryonic concept; they have long constituted a methodological cornerstone in high- precision medical imaging domains such as radiation therapy planning and image-guided interventions, serving as a gold-standard reference for patient positioning verification and treatment accuracy assessment [156]. The incorporation of DRR-based validation thus confers dual significance: it not only bolsters the external validity of our simulation-derived results but also affirms the robustness and clinical plausibility of our integrated kinematic and trajectory-planning framework under conditions approximating authentic surgical imaging workflows.

- Dataset Characteristics: The generated datasets encompass thousands of poses across six clinically relevant projections; however, they are inevitably bounded by the surgical scenarios and patient anatomies modelled during this study. Patient variability, non- standard procedural workflows, and rare intraoperative postures may necessitate significant dataset expansion to ensure robust generalization in clinical use.

5.5 Recommendations for Future Work

To sustain the momentum generated by this research and to ensure its translation from theoretical constructs into routine clinical practice, it is imperative to pursue targeted advancements that address both technical and translational gaps. While the developed framework has demonstrated significant promise in simulation, its full clinical impact will only be realized through iterative refinement, integration with real-world systems, and validation in diverse surgical environments. The following recommendations outline a strategic roadmap for future research:

1. Real-Time Hardware Integration: Establishing direct interfaces between the developed trajectory planners and operational C-arm and surgical table systems. This integration will facilitate hardware-in-the-loop testing, enabling the identification and resolution of latency, control precision, and safety challenges before clinical deployment.
2. Multi-Objective Planning: Advancing the trajectory optimization framework to concurrently balance multiple clinically relevant objectives, such as minimizing radiation exposure,

maximizing surgeon line-of-sight, and reducing ergonomic strain on the operating team. This will align technical optimization with broader patient safety and workflow efficiency goals.

3. Clinical Validation: Collaborative discussions with surgical teams at The Ottawa Hospital, particularly within the Divisions of Vascular and Orthopedic Surgery, have underscored a pronounced interest in empirically assessing the proposed integration of table positioning within intraoperative workflows. A rigorous next phase would entail the development and execution of a controlled, two-arm clinical trial, wherein one patient cohort undergoes procedures with conventional C-arm imaging alone, and a matched cohort is treated using the proposed C-arm/table integrated kinematic system. Comparative evaluation across quantifiable performance indicators including the aggregate number of X-ray acquisitions, cumulative radiation dose, and total operative duration would provide robust, objective evidence of the system's clinical efficacy, operational efficiency, and safety impact. Moreover, the trial would serve as a conduit for collecting nuanced, experiential feedback from surgical teams, thereby informing iterative refinements to both the algorithmic architecture and hardware integration to ensure alignment with the complex realities of live surgical environments.
4. Interoperability Frameworks: Collaborating with imaging system manufacturers, surgical robotics developers, and standards bodies to create open, vendor-agnostic communication protocols. This will ensure that future imaging–robotics–navigation ecosystems are interoperable, scalable, and future-proof, thereby accelerating widespread adoption.

References:

1. Moataz, Amr, et al. "Three-dimensional angiography using mobile C-arm with IMU sensor attached: Initial study." *2015 IEEE Nuclear Science Symposium and Medical Imaging Conference (NSS/MIC)*. IEEE, 2015.
2. Mandigers, Tim J., et al. "Patients' radiation exposure during endovascular abdominal aortic aneurysm repair." *Annals of Vascular Surgery* 98 (2024): 115-123.
3. Clauss, Nicolas, et al. "Intraoperative staff radiation exposure during aortic endovascular procedures." *Annals of vascular surgery* 106 (2024): 16-24.
4. Murphey, Mark D. "Imaging aspects of new techniques in orthopedic surgery." *Radiologic Clinics of North America* 32.2 (1994): 201-225.
5. Langlotz, Frank. "State-of-the-art in orthopaedic surgical navigation with a focus on medical image modalities." The Journal of Visualization and Computer Animation 13.1 (2002): 77-83.
6. S. Webb, The Physics of Medical Imaging. Taylor & Francis Group, Jan. 1988.
7. Wolbarst, Anthony B., and William R. Hendee. "Evolving and experimental technologies in medical imaging." *Radiology* 238.1 (2006): 16-39.
8. Stiehl, James B., et al., eds. *Navigation and MIS in orthopedic surgery*. Springer Medizin Verlag Heidelberg, 2007.
9. Schep, Niels Willem Luitzen, I. A. M. J. Broeders, and Chr Van der Werken. "Computer assisted orthopaedic and trauma surgery: State of the art and future perspectives." *Injury* 34.4 (2003): 299-306.
10. Langlotz, Frank, and Lutz-Peter Nolte. "Technical approaches to computer-assisted orthopedic surgery." *European Journal of Trauma* 30.1 (2004): 1-11.
11. Zheng, Guoyan, and Lutz-Peter Nolte. "Technical principles of computer assisted orthopaedic surgery." *Suom Ortop ja Traumatol* 31.2 (2008): 135-47.
12. Nolte, Lutz P., and Thomas Beutler. "Basic principles of CAOS." *Injury* 35 (2004): S-A6.
13. Kahler, David M. "Image guidance: fluoroscopic navigation." *Clinical Orthopaedics and Related Research (1976-2007)* 421 (2004): 70-76.
14. Wang, Lejing. *Novel techniques for integrating video augmented X-ray imaging into orthopedic and trauma surgery*. Diss. Technische Universität München, 2012.
15. Robb, J. D. *Estimates of radiation detriment in a UK population*. No. NRPB-R--260. National Radiological Protection Board, Chilton (United Kingdom), 1994.
16. Beir, V. "Health effects of exposure to low levels of ionizing radiation." *Biological effects of ionizing radiations.* (1990): 22-45.

17. Cousins, Claire, et al. "International commission on radiological protection." *ICRP publication* 120 (2011): 1-125.
18. Stübig, Timo, et al. "Comparative study of different intraoperative 3-D image intensifiers in orthopedic trauma care." *Journal of Trauma and Acute Care Surgery* 66.3 (2009): 821-830.
19. Kendoff, Daniel, et al. "Intraoperative 3D imaging: value and consequences in 248 cases." *Journal of Trauma and Acute Care Surgery* 66.1 (2009): 232-238.
20. Kendoff, D., et al. "Value of 3D fluoroscopic imaging of acetabular fractures comparison to 2D fluoroscopy and CT imaging." *Archives of orthopaedic and trauma surgery* 128.6 (2008): 599-605.
21. Lemieux, Louis, Dale L. Bailey, and David Bell. "Correcting for scanner errors in CT, MRI, SPECT, and 3D ultrasound." *Medical Image Registration* (2001).
22. Robertson, Douglas D., et al. "Evaluation of CT techniques for reducing artifacts in the presence of metallic orthopedic implants." *Journal of computer assisted tomography* 12.2 (1988): 236-241.
23. Mahnken, Andreas H., et al. "A new algorithm for metal artifact reduction in computed tomography: in vitro and in vivo evaluation after total hip replacement." *Investigative radiology* 38.12 (2003): 769-775.
24. Rohlfing, Torsten, et al. "Reduction of metal artifacts in computed tomographies for the planning and simulation of radiation therapy." *Computer Assisted Radiology and Surgery*. 1998.
25. Yazdia, Mehran, Luc Gingras, and Luc Beaulieu. "An adaptive approach to metal artifact reduction in helical computed tomography for radiation therapy treatment planning: experimental and clinical studies." *International Journal of Radiation Oncology* Biology* Physics* 62.4 (2005): 1224-1231.
26. Yu, Lifeng, et al. "Metal artifact reduction from reformatted projections for hip prostheses in multislice helical computed tomography: techniques and initial clinical results." *Investigative radiology* 44.11 (2009): 691-696.
27. Zhang, Yongbin, et al. "Reducing metal artifacts in cone-beam CT images by preprocessing projection data." *International Journal of Radiation Oncology* Biology* Physics* 67.3 (2007): 924-932.
28. Fong, Yuman, et al., eds. *Imaging and visualization in the modern operating room: a comprehensive guide for physicians*. Springer, 2015.
29. Matthews, Felix, et al. "Navigating the fluoroscope's C-arm back into position: an accurate and practicable solution to cut radiation and optimize intraoperative workflow." *Journal of orthopaedic trauma* 21.10 (2007): 687-692.
30. Navab, Nassir, et al. "Visual servoing for intraoperative positioning and repositioning of mobile C-arms." *International conference on medical image computing and computer-assisted intervention*. Berlin, Heidelberg: Springer Berlin Heidelberg, 2006.

31. Matthäus, Lars, et al. "Closed-form inverse kinematic solution for fluoroscopic C-arms." *Advanced Robotics* 21.8 (2007): 869-886.

32. Dressel, Philipp, et al. "Intraoperative positioning of mobile C-arms using artificial fluoroscopy." *Medical Imaging 2010: Visualization, Image-Guided Procedures, and Modelling*. Vol. 7625. SPIE, 2010.

33. Schaller, Christian, et al. "Inverse C-arm positioning for interventional procedures using real-time body part detection." *International Conference on Medical Image Computing and Computer-Assisted Intervention*. Berlin, Heidelberg: Springer Berlin Heidelberg, 2009.

34. Markelj, Primoz, et al. "A review of 3D/2D registration methods for image-guided interventions." *Medical image analysis* 16.3 (2012): 642-661.

35. Fallavollita, Pascal, et al. "Unsupervised C-arm pose tracking with radiographic fiducial." *Medical physics* 38.4 (2011): 2241-2245.

36. Fallavollita, Pascal, et al. "C-arm tracking by intensity-based registration of a fiducial in prostate brachytherapy." *International Conference on Information Processing in Computer-Assisted Interventions*. Berlin, Heidelberg: Springer Berlin Heidelberg, 2010.

37. Graetzel, Chauncey, et al. "A non-contact mouse for surgeon-computer interaction." *Technology and Health Care* 12.3 (2004): 245-257.

38. Wachs, Juan, et al. "A real-time hand gesture interface for medical visualization applications." *Applications of Soft Computing: Recent Trends*. Berlin, Heidelberg: Springer Berlin Heidelberg, 2006. 153-162.

39. Stern, Helman I., Juan P. Wachs, and Yael Edan. "Optimal consensus intuitive hand gesture vocabulary design." *2008 IEEE International Conference on Semantic Computing*. IEEE, 2008.

40. McLaughlin, K. "Microsoft Partners See Kinect Going Beyond Games." *ChannelWeb http://www. crn. com/software/225700575 17th June* (2010).

41. Johnson, Rose, et al. "Exploring the potential for touchless interaction in image-guided interventional radiology." *Proceedings of the SIGCHI Conference on Human Factors in Computing Systems*. 2011.

42. Ruijters, Daniel Simon Anna, Sander Denissen, and Nicolaas Hylke BAKKER. "Automatic c-arm viewing angles for structural heart disease treatment." U.S. Patent No. 8,681,935. 25 Mar. 2014.

43. Virga, Salvatore, et al. "Optimal c-arm positioning for aortic interventions." *Bildverarbeitung für die Medizin 2015: Algorithmen-Systeme-Anwendungen. Proceedings des Workshops vom 15. bis 17. März 2015 in Lübeck*. Berlin, Heidelberg: Springer Berlin Heidelberg, 2015.

44. Fallavollita, Pascal, et al. "Desired-view controlled positioning of angiographic C-arms." *International Conference on Medical Image Computing and Computer-Assisted Intervention*. Cham: Springer International Publishing, 2014.
45. Wang, Xiang, et al. "Inverse visualization concept for RGB-D augmented C-arms." *Computers in biology and medicine* 77 (2016): 135-147.
46. Wang, Lejing, et al. "Closed-form inverse kinematics for interventional C-arm X-ray imaging with six degrees of freedom: modelling and application." *IEEE transactions on medical imaging* 31.5 (2012): 1086-1099.
47. Kausch, Lisa, et al. "Toward automatic C-arm positioning for standard projections in orthopedic surgery." *International journal of computer assisted radiology and surgery* 15 (2020): 1095-1105.
48. Yazdanshenas, Armin. "Acute Angle Repositioning in Mobile C-Arm Using Image Processing and Deep Learning." (2019).
49. Yazdanshenas, Armin, Alireza Yazdanshenas, and Chung-Hyun Goh. "Automatic and accurate repositioning of C-arm prototype using motion capture systems and deep learning." *SN Computer Science* 1.3 (2020): 135.
50. Kagawa, Takahiro, et al. "Optimization-based motion planning in joint space for walking assistance with wearable robot." *IEEE Transactions on Robotics* 31.2 (2015): 415-424.
51. Kagawa, Takahiro, and Yoji Uno. "Gait pattern generation for a power-assist device of paraplegic gait." *RO-MAN 2009-The 18th IEEE International Symposium on Robot and Human Interactive Communication*. IEEE, 2009.
52. Li, Shupei, et al. "Hybrid polynomial-based trajectory planning for lower limb exoskeleton robots." *2023 IEEE 18th Conference on Industrial Electronics and Applications (ICIEA)*. IEEE, 2023.
53. Kim, Byoung-Ho. "A Bio-Mimetic Joint Motion Planning for Humanoid Fingers: Practical Analysis." *2006 IEEE International Conference on Robotics and Biomimetics*. IEEE, 2006.
54. Huang, Panfeng, et al. "Motion trajectory planning of space manipulator for joint jerk minimization." *2007 international conference on mechatronics and automation*. IEEE, 2007.
55. Porawagama, Chinthaka D., and S. Rohan Munasinghe. "Reduced jerk joint space trajectory planning method using 5-3-5 spline for robot manipulators." *7th International Conference on Information and Automation for Sustainability*. IEEE, 2014.
56. Goloburdin, Nikolay V., et al. "Planning the Trajectory of a Manipulator Robot for a Set of Configurations in Joint Space." *2023 7th International Conference on Information, Control, and Communication Technologies (ICCT)*. IEEE, 2023.

57. Luo, Kun, et al. "Research on trajectory planning and motion control of 7-DoF sawyer manipulator." *2021 IEEE 1st international conference on digital twins and parallel intelligence (DTPI)*. IEEE, 2021.
58. Edition, Third, and John J. Craig. "Introduction to Robotics." (2005).
59. Hargest, Rachel. "Five thousand years of minimal access surgery: 3000BC to 1850: early instruments for viewing body cavities." *Journal of the Royal Society of Medicine* 113.12 (2020): 491-496.
60. Mattelaer, J. J., and Ignace Billiet. "Catheters and sounds: the history of bladder catheterisation." *Spinal Cord* 33.8 (1995): 429-433.
61. Driver, Godfrey Rolles, and John C. Miles. *The Babylonian Laws*. Wipf and Stock Publishers, 2007.
62. Singh, Vibha. "Sushruta: The father of surgery." *National journal of maxillofacial surgery* 8.1 (2017): 1-3.
63. Rudiman, Reno. "Advances in gastrointestinal surgical endoscopy." *Annals of Medicine and Surgery* 72 (2021): 103041.
64. Schollmeyer, Thoralf, et al., eds. *Practical manual for laparoscopic & hysteroscopic gynecological surgery*. JP Medical Ltd, 2013.
65. Amr, Samir S., and Abdelghani Tbakhi. "Abu al Qasim al Zahrawi (Albucasis): pioneer of modern surgery." *Annals of Saudi medicine* 27.3 (2007): 220-221.
66. Frampton, Sally, and Roger L. Kneebone. "John Wickham's new surgery:'minimally invasive therapy', innovation, and approaches to medical practice in twentieth-century Britain." *Social History of Medicine* 30.3 (2017): 544-566.
67. Schlich, Thomas. "'the days of brilliancy are past': Skill, styles and the changing rules of surgical performance, ca. 1820–1920." *Medical History* 59.3 (2015): 379-403.
68. Doctor in the House. Directed by Ralph Thomas, performance by Dirk Bogarde, ITV Studios Home Entertainment, 1954, London, 2002, DVD.
69. Mattelaer, J. J., and Ignace Billiet. "Catheters and sounds: the history of bladder catheterisation." *Spinal Cord* 33.8 (1995): 429-433.
70. "Sakkara Doctor Tomb Unearthed." Legends, www.jayepurplewolf.com/LEGENDS/sakkaradoctortomb.html. Accessed 11 Aug. 2025.
71. Adamson, P. B. "Surgery in ancient Mesopotamia." *Medical History* 35.4 (1991): 428-435.
72. Babylonian Talmud. 1300 BC.
73. "Medicine." Jewish Encyclopedia, www.jewishencyclopedia.com/articles/10544-medicine. Accessed 11 Aug. 2025.

74. Natarajan, K. "Surgical instruments and endoscopes of Susruta, the sage surgeon of ancient India." *Indian Journal of Surgery* 70.5 (2008): 219-223.
75. Singhal, G., and L. Singh. "Ancient Indian surgery based on Susrata Samhita." (1981).
76. Bhishagratna, Kunja Lal, ed. *An English translation of The Sushruta Samhita: based on original Sanskrit text*. Vol. 2. author, 1911.
78. Sharma, P. V., and Sushruta Samhita. "Chaukhambha Visvabharati." (2000).
79. Hippocrates. Aphorisms. Section 7 No. 87, 400BC.
80. Gurunluoglu, Raffi, et al. "Giulio Cesare Aranzio (Arantius)(1530–89) in the pageant of anatomy and surgery." *Journal of Medical Biography* 19.2 (2011): 63-69.
81. De Ronsil, Georges Arnaud, and William Hunter. *Memoires de chirurgie, avec quelques remarques historiques sur l'etat de la médecine & de la chirurgie en France & en Angleterre. Par George Arnaud, docteur en médecine, ancien membre de l'académie royale de chirurgie de Paris, & un des professeurs en l'ecole de St. Cosme, membre de la société des chirurgiens de Londres. Premiere [-seconde] partie*. chez J. Nourse, libraire du Roi, dans le Strand., 1768..
82. Bozzini, Philipp. "Lichtleiter, eine Erfindung zur Anschauung innerer Theile und Krankheiten nebst der Abbildung." *Journal der practischen Heilkunde, Berlin* 24 (1806): 107-124.
83. Nezhat, Camran, and Barbara J. Page. *Nezhat's history of endoscopy: a historical analysis of endoscopy's ascension since antiquity*. CNezhatMD, 2011.
84. Fisher, J. "Instruments for illuminating dark cavities." *Phil J Med Phys Sci* 14 (1827): 409.
85. Desormeaux, Antonin Jean. *De l'endoscope et de ses applications au diagnostic et au traitement des affections de l'urethre et de la vessie*. Baillière, 1865.
86. Sircus, W. "Milestones in the evolution of endoscopy: a short history." *Journal of the Royal College of Physicians of Edinburgh* 33.2 (2003): 124-134.
87. Desormeaux, A. J. "The endoscope, and its application to the diagnosis and treatment of urinary affections." *The Chicago medical journal* 24.4-5 (1867): 177.
88. Noël, Jonathan Patrick, and Jonathan Charles Goddard. "FRI-15 THE INTRODUCTION OF THE CYSTOSCOPE TO THE BRITISH ISLES." *The Journal of Urology* 191.4S (2014): e625-e626.
89. Ojodu, Ishaq, et al. "C-arm fluoroscopy in orthopaedic surgical practice." *European Journal of Orthopaedic Surgery & Traumatology* 28.8 (2018): 1563-1568.
90. Wong, Kang Min, et al. "Cone beam computed tomography for vascular interventional radiology procedures: early experience." *Annals of the Academy of Medicine-Singapore* 40.7 (2011): 308.
91. Schafer, S., et al. "Mobile C-arm cone-beam CT for guidance of spine surgery: image quality, radiation dose, and integration with interventional guidance." *Medical physics* 38.8 (2011): 4563-4574.

92. Fiani, Brian, et al. "Thoracic endoscopic spine surgery: a comprehensive review." *International Journal of Spine Surgery* 14.5 (2020): 762-771.
93. Staufer, Theresa, and Florian Grüner. "Review of development and recent advances in biomedical X-ray fluorescence imaging." *International Journal of Molecular Sciences* 24.13 (2023): 10990.
94. Balter, Stephen. "Fluoroscopic technology from 1895 to 2019 drivers: Physics and physiology." *Medical Physics International*7 (2019): 111-140.
95. Krettek, C., and Florian Gebhard. "Development of intraoperative C-arm imaging in trauma surgery." *Der Unfallchirurg* 115.2 (2012): 100-106.
96. Xing, Shuwei, et al. "Virtual fluoroscopy for interventional guidance using magnetic tracking." *International Journal of Computer Assisted Radiology and Surgery* (2025): 1-9.
97. Plastaras, Christopher T., et al. "C-arm fluoroscope angle settings for fluoroscopically guided lumbar transforaminal epidural injections." *Pain Medicine* 17.5 (2016): 832-838.
98. Shirbache, Kamran, et al. "A systematic review and meta-analysis of radiation exposure in spinal surgeries: Comparing C-Arm, CT navigation, and O-Arm techniques." *Journal of medical imaging and radiation sciences* 56.2 (2025): 101831.
99. Kaneko, Tsuyoshi, and Michael J. Davidson. "Use of the hybrid operating room in cardiovascular medicine." *Circulation*130.11 (2014): 910-917.
100. Park, Sangman, et al. "Novel C-arm-based planning robotic spinal surgery in a cadaver model using quantitative accuracy assessment methodology." *The International Journal of Medical Robotics and Computer Assisted Surgery* 18.6 (2022): e2442.
101. Hua, Chiaho, et al. "A robotic C-arm cone beam CT system for image-guided proton therapy: design and performance." *The British journal of radiology* 90.1079 (2017): 20170266.
102. Wang, Fuhao, et al. "FABRIKv: A Fast, Iterative Inverse Kinematics Solver for Surgical Continuum Robot with Variable Curvature Model." *2023 IEEE/RSJ International Conference on Intelligent Robots and Systems (IROS)*. IEEE, 2023.
103. Yang, Yingkan, et al. "Design of a dexterous robotic surgical instrument with a novel bending mechanism." *The International Journal of Medical Robotics and Computer Assisted Surgery* 18.1 (2022): e2334.
104. Dumitru, V., et al. "Determining the Design Specifications for Mechanical Polyarticulated System Compatible with Minimally Invasive Surgery." *New Trends in Mechanism and Machine Science: Theory and Applications in Engineering*. Dordrecht: Springer Netherlands, 2012. 367-374.

105. Pisla, Doina, et al. "Kinematics and workspace modelling of a new hybrid robot used in minimally invasive surgery." *Robotics and Computer-Integrated Manufacturing* 29.2 (2013): 463-474.

106. Mohamed, Khaled, Hassan Elgamal, and Amr Elsharkawy. "Dynamic analysis with optimum trajectory planning of multiple degree-of-freedom surgical micro-robot." *Alexandria engineering journal* 57.4 (2018): 4103-4112.

107. Xie, Yanchun, et al. "Flexible control and trajectory planning of medical two-arm surgical robot." *Frontiers in Neurorobotics* 18 (2024): 1451055.

108. Du, Yuxiao, and Yihang Chen. "Time optimal trajectory planning algorithm for robotic manipulator based on locally chaotic particle swarm optimization." *Chinese Journal of Electronics* 31.5 (2022): 906-914.

109. Zhang, Rui, et al. "Computer-assisted needle trajectory planning and mathematical modelling for liver tumor thermal ablation: A review." *Mathematical biosciences and engineering*16.5 (2019): 4846-4872.

110. Yao, Jianhua, et al. "A C-arm fluoroscopy-guided progressive cut refinement strategy using a surgical robot." *Computer Aided Surgery* 5.6 (2000): 373-390.

111. Li, Meng, et al. "A stability and safety control method in robot-assisted decompressive laminectomy considering respiration and deformation of spine." *IEEE Transactions on Automation Science and Engineering* 20.1 (2022): 258-270.

112. Prendergast, J. Micah, and Mark E. Rentschler. "Towards autonomous motion control in minimally invasive robotic surgery." *Expert review of medical devices* 13.8 (2016): 741-748.

113. Young, Taylor R., Yuen K. Yong, and Andrew J. Fleming. "Data-Driven Inverse Control of Pneumatic Soft Robotic Actuators with On-Off Valves: Simulated Performance." *2025 IEEE International Conference on Mechatronics (ICM)*. IEEE, 2025.

114. Leibrandt, Konrad, Christos Bergeles, and Guang-Zhong Yang. "Concentric tube robots: Rapid, stable path-planning and guidance for surgical use." *IEEE Robotics & Automation Magazine* 24.2 (2017): 42-53.

115. Siciliano, Bruno, Oussama Khatib, and Torsten Kröger, eds. *Springer handbook of robotics*. Vol. 200. Berlin: springer, 2008.

116. Craig, John J. "Introduction to Robotics." (2005).

117. Xiao, Bo, et al. "Learning-Based Inverse Kinematics Identification of the Tendon-Driven Robotic Manipulator for Minimally Invasive Surgery." *IECON 2023-49th Annual Conference of the IEEE Industrial Electronics Society*. IEEE, 2023.

118. Relaño, Carlos, Javier Muñoz, and Concepción A. Monje. "Gaussian process regression for forward and inverse kinematics of a soft robotic arm." *Engineering Applications of Artificial Intelligence* 126 (2023): 107174.

119. Kinoshita, Koji, Hiroshi Okimoto, and Kenji Murakami. "Forward-propagation rule based on ridge regression for inverse kinematics problem." *2008 SICE annual conference*. IEEE, 2008.

120. Shah, Muhammad Faizan, et al. "A Deep Learning-Aided Framework for Joint Angle Estimation of an Upper Limb Rehabilitation Robot." *2024 26th International Multi-Topic Conference (INMIC)*. IEEE, 2024.

121. Hsieh, Po-Yu, and June-Hao Hou. "Comparative Evaluation of Learning Models for Bionic Robots." *2024 International Symposium on Intelligent Signal Processing and Communication Systems (ISPACS)*. IEEE, 2024.

122. Cho, Brian Y., et al. "Accounting for hysteresis in the forward kinematics of nonlinearly-routed tendon-driven continuum robots via a learned deep decoder network." *IEEE Robotics and Automation Letters* (2024).

123. Singh, Ranbir, et al. "Application of Deep Learning Model for Analysis of Forward Kinematics of a 6-Axis Robotic Hand for a Humanoid." *2024 3rd International Conference on Artificial Intelligence and Autonomous Robot Systems (AIARS)*. IEEE, 2024.

124. Shimizu, Soya, et al. "Whole-body motion blending under physical constraints using functional PCA." *2018 IEEE-RAS 18th International Conference on Humanoid Robots (Humanoids)*. IEEE, 2018.

125. Carreira, Fernando, et al. "2d pca-based localization for mobile robots in unstructured environments." *2012 IEEE/RSJ International Conference on Intelligent Robots and Systems*. IEEE, 2012.

126. Tamimi, Hashem, and Andreas Zell. "Global visual localization of mobile robots using kernel principal component analysis." *2004 IEEE/RSJ International Conference on Intelligent Robots and Systems (IROS)(IEEE Cat. No. 04CH37566)*. Vol. 2. IEEE, 2004.

127. Ra, Syungkwon, et al. "PCA-based genetic operator for evolving movements of humanoid robot." *2008 IEEE Congress on Evolutionary Computation (IEEE World Congress on Computational Intelligence)*. IEEE, 2008.

128. GE Healthcare, “OEC 3D Surgical Imaging System,” GE Healthcare, [Online]. Available: https://www.gehealthcare.com/products/surgical-imaging/oec-3d.

129. STERIS Corporation, CMAX™ X-Ray Operating table—Product Specification Manual, Mentor, OH, USA: STERIS Corp., 2023. [Online]. Available: https://www.steris.com.

130. “MATLAB R2023a - Transform Sensor.” Accessed: May 12, 2024. [Online]. Available: https://www.mathworks.com/help/sm/ref/transformsensor.html

131. Huynh, Du Q. "Metrics for 3D rotations: Comparison and analysis." *Journal of Mathematical Imaging and Vision* 35.2 (2009): 155-164.

132. “Blender.” Accessed: May 12, 2024. [Online]. Available: https://www.blender.org/.

133. “Vedo- Collision Detection.” Accessed: May 12, 2024. [Online]. Available: https://vedo.embl.es/docs/vedo/mesh.html#Mesh.inside_points.

134. Rodas, Nicolas Loy, et al. "Pose optimization of a C-arm imaging device to reduce intraoperative radiation exposure of staff and patient during interventional procedures." *2017 IEEE International Conference on Robotics and Automation (ICRA)*. IEEE, 2017.

135. “L-BFGS-B.” Accessed: Oct. 16, 2024. [Online]. Available: https://docs.scipy.org/doc/scipy/reference/optimize.minimize-lbfgsb.html#optimize-minimize-lbfgsb.

136. Biagiotti, Luigi, and Claudio Melchiorri. *Trajectory planning for automatic machines and robots*. Springer Science & Business Media, 2008.

137. Sciavicco, Lorenzo, and Bruno Siciliano. *Modelling and control of robot manipulators*. Springer Science & Business Media, 2012.

138. Chaturvedi, Nirbhay Kumar, and L. B. Prasad. "A comparison of computed torque control and sliding mode control for a three zink robot manipulator." *2018 International Conference on Computing, Power and Communication Technologies (GUCON)*. IEEE, 2018.

139. Li, Shuwei, et al. "Blind-Kriging based natural frequency modelling of industrial Robot." *Precision Engineering* 74 (2022): 126-139.

140. Naiem, Ahmed A., et al. "Association Between Obesity and Outcomes Following Endovascular Aneurysm Repair." *Annals of Vascular Surgery* 94 (2023): 356-361.

141. Jaheen, Faria. “Modular C-Arm Kinematics Dataset (5–9 DoF),” *GitHub repository*, 2025. [Online]. Available: https://github.com/FariaJaheen/Modular-CArm_Dataset.

142. Sekeroglu, Boran, et al. "Comparative evaluation and comprehensive analysis of machine learning models for regression problems." *Data Intelligence* 4.3 (2022): 620-652.

143. Botchkarev, Alexei. "Evaluating performance of regression machine learning models using multiple error metrics in azure machine learning studio." *Available at SSRN 3177507* (2018).

144. Dumre, Prabin, Somnath Bhattarai, and H. K. Shashikala. "Optimizing linear regression models: A comparative study of error metrics." *2024 4th International Conference on Technological Advancements in Computational Sciences (ICTACS)*. IEEE, 2024.

145. Rhinehart, R. Russell. *Nonlinear regression modelling for engineering applications: modelling, model validation, and enabling design of experiments*. John Wiley & Sons, 2016.

146. Lu, Jiaoyang, Ting Zou, and Xianta Jiang. "A neural network based approach to inverse kinematics problem for general six-axis robots." *Sensors* 22.22 (2022): 8909.

147. Miao, Shun, et al. "Dilated FCN for multi-agent 2D/3D medical image registration." *Proceedings of the AAAI Conference on Artificial Intelligence*. Vol. 32. No. 1. 2018.

148. Liao, Haofu, et al. "Multiview 2D/3D rigid registration via a point-of-interest network for tracking and triangulation." *Proceedings of the IEEE/CVF Conference on Computer Vision and Pattern Recognition*. 2019.

149. Gopalakrishnan, Vivek, and Polina Golland. "Fast auto-differentiable digitally reconstructed radiographs for solving inverse problems in intraoperative imaging." *Workshop on Clinical Image-Based Procedures*. Cham: Springer Nature Switzerland, 2022.

150. Lowe, David G. "Distinctive image features from scale-invariant keypoints." *International journal of computer vision* 60.2 (2004): 91-110.

151. "OpenCV". Accessed: Jun. 06, 2025. [Online]. Available: https://opencv.org/

152. Wasserthal, Jakob, et al. "TotalSegmentator: robust segmentation of 104 anatomic structures in CT images." *Radiology: Artificial Intelligence* 5.5 (2023): e230024.

153. Pernus, Franjo. "3D-2D registration of cerebral angiograms: A method and evaluation on clinical images." *IEEE transactions on medical imaging* 32.8 (2013): 1550-1563.

154. Grupp, Robert B., et al. "*X-ray Computed Tomography and Fluoroscopy Collected during Cadaveric Periacetabular Osteotomy Experiments*." Johns Hopkins Research Data Repository, 2022, doi:10.7281/T1/C304HZ/SNMOHX. https://doi.org/10.7281/T1/C304HZ/SNMOHX

155. Frysch, Robert, Tim Pfeiffer, and Georg Rose. "A novel approach to 2D/3D registration of X-ray images using Grangeat's relation." *Medical Image Analysis* 67 (2021): 101815.

156. Yang, Demin, et al. "2D/3D registration based on biplanar X-ray and CT images for surgical navigation." *Computer Methods and Programs in Biomedicine* 257 (2024): 108444.

157. Jaheen, Faria, Vinod Gutta, and Pascal Fallavollita. "C-Arm and Patient Table Integrated Kinematics and Surgical Workspace Analysis," in *IEEE Access*, vol. 13, pp. 180276-180290, 2025, doi: 10.1109/ACCESS.2025.3615843.

158. Jaheen, Faria, Vinod Gutta, and Pascal Fallavollita. "Trajectory Planning for Multiple Degrees of Freedom C-Arm Systems," in *IEEE Access*, vol. 13, pp. 181396-181415, 2025, doi: 10.1109/ACCESS.2025.3623567.

159. Jaheen, Faria, Vinod Gutta, and Pascal Fallavollita. "Modelling C-arm fluoroscopy and Operating table Kinematics via Machine Learning" in Front. Robot. AI. **Accepted:** 10 Nov 2025.

160. Han, Hong, Xiaoling Guo, and Hua Yu. "Variable selection using mean decrease accuracy and mean decrease gini based on random forest." *2016 7th ieee international conference on software engineering and service science (icsess)*. IEEE, 2016.

Appendices

Appendix 1

The supplementary dataset corresponding to the positional error analysis across all configurations and trajectory profiles for overweight versus normal weight patient conditions, has been deposited in an open-access GitHub repository.

Appendix 2

The complete dataset and supplementary results corresponding to this appendix are hosted in a dedicated GitHub repository. The repository contains detailed trajectory comparisons and reproducibility of the presented findings.

Appendix 3

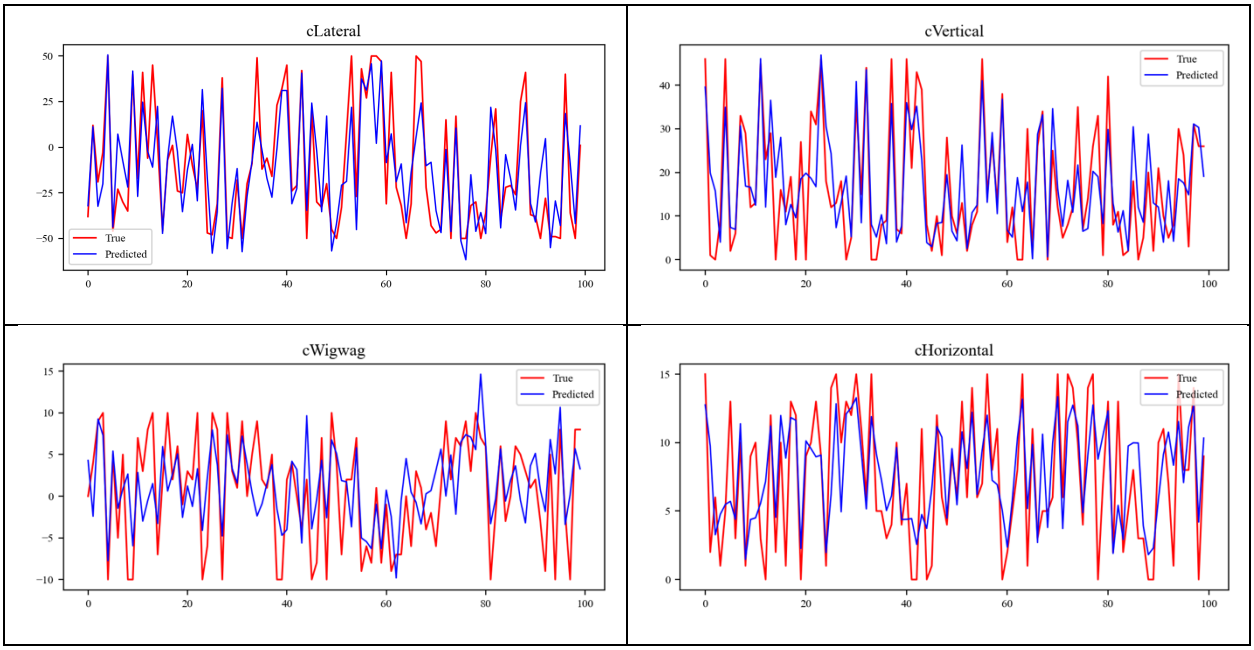

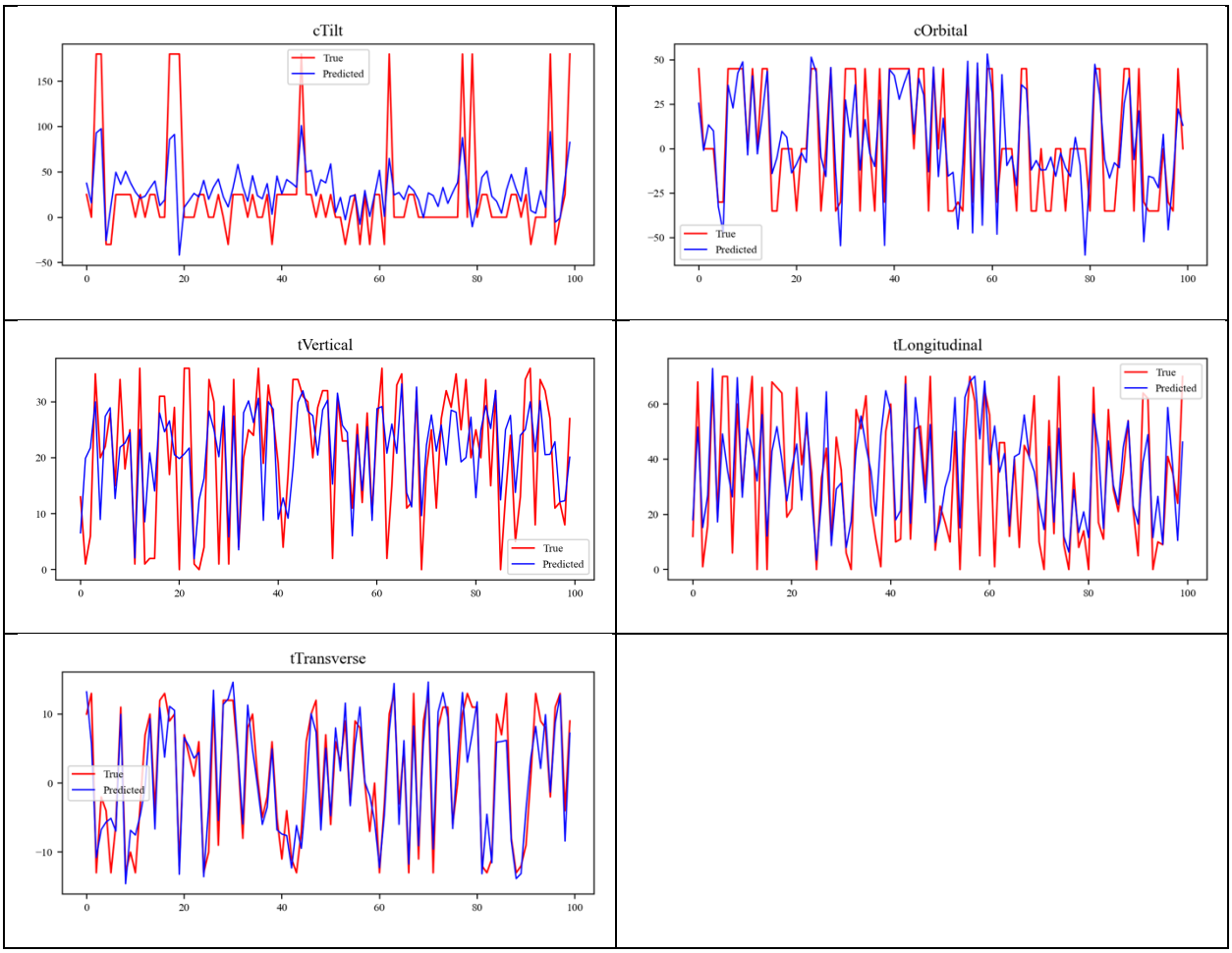

Figure 5.1: Prediction on the test set using Ridge Regression.

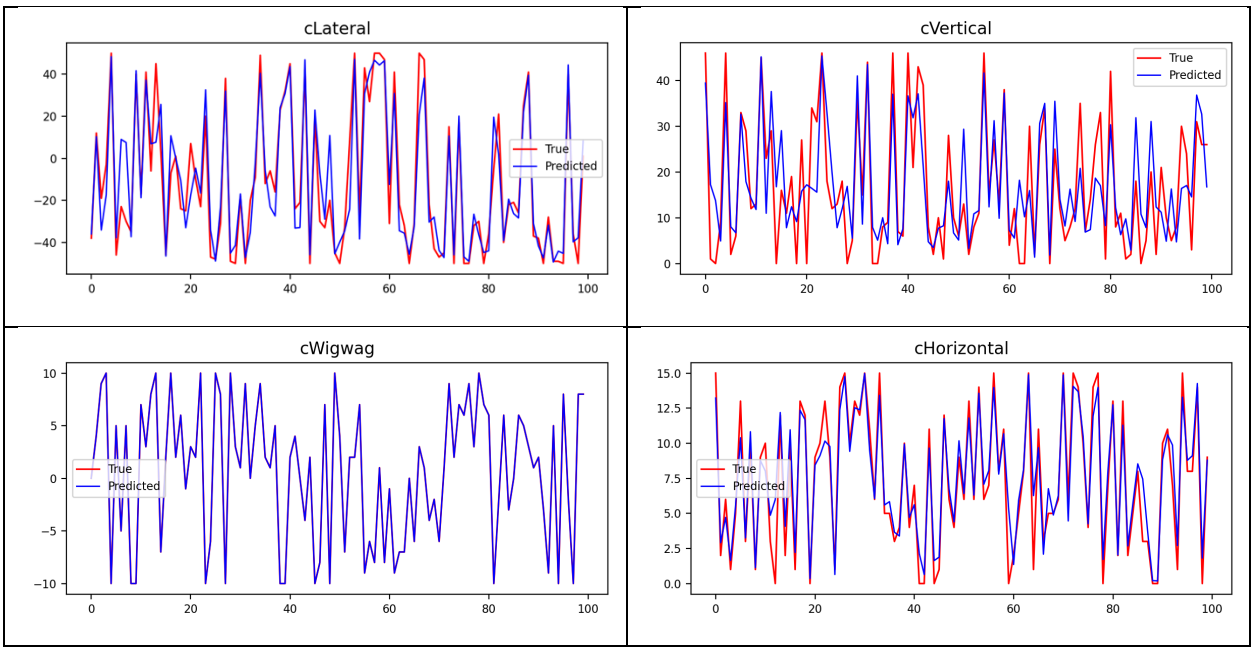

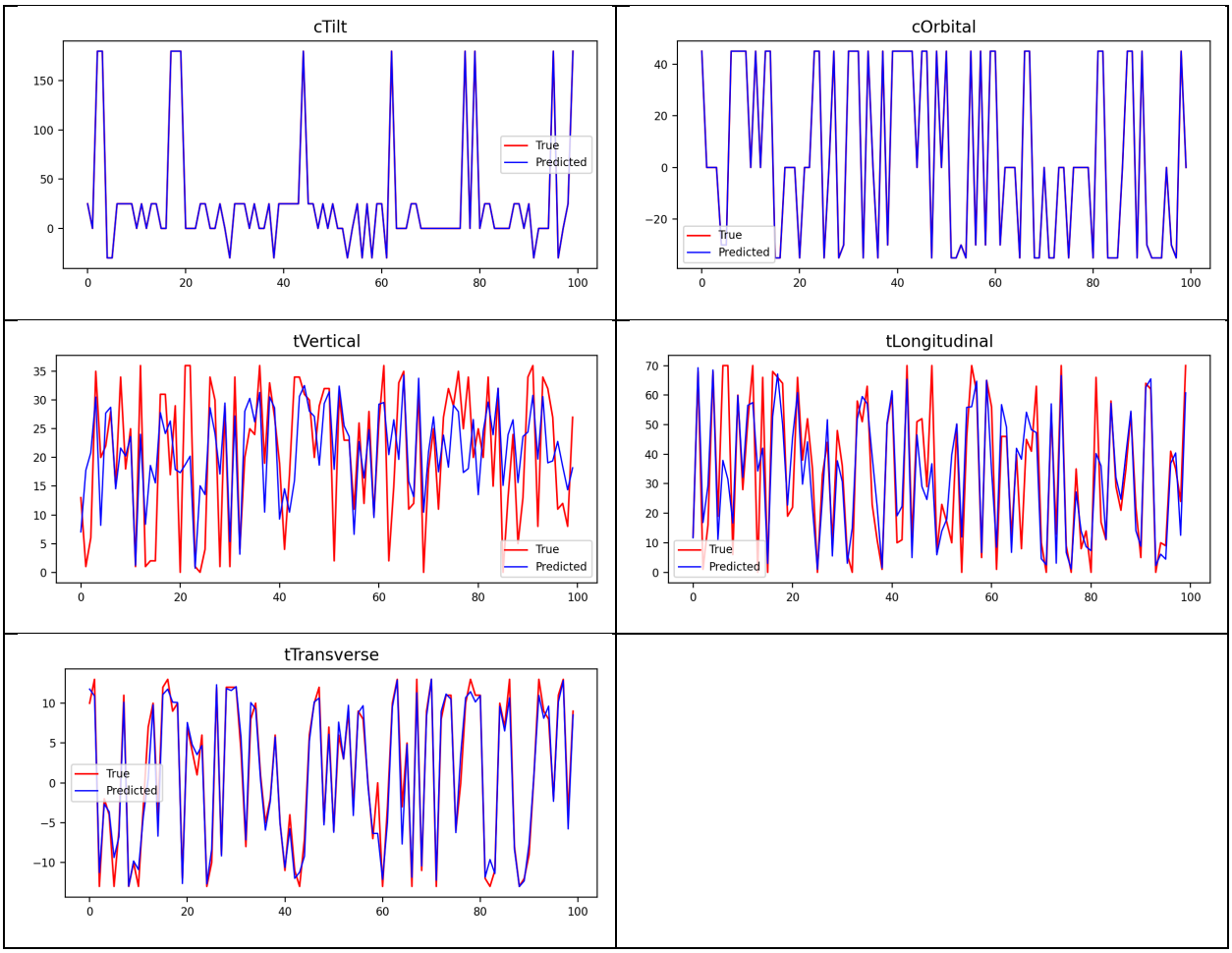

Figure 5.2: Prediction on the test set using Gradient Boosting Machine.

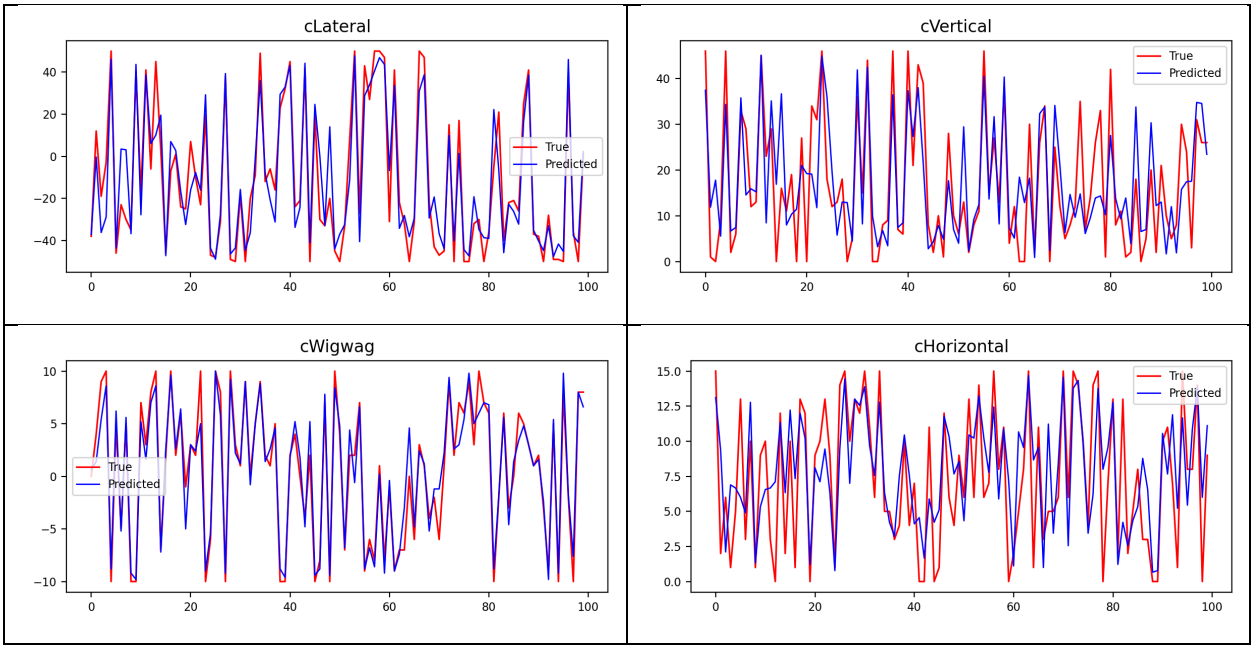

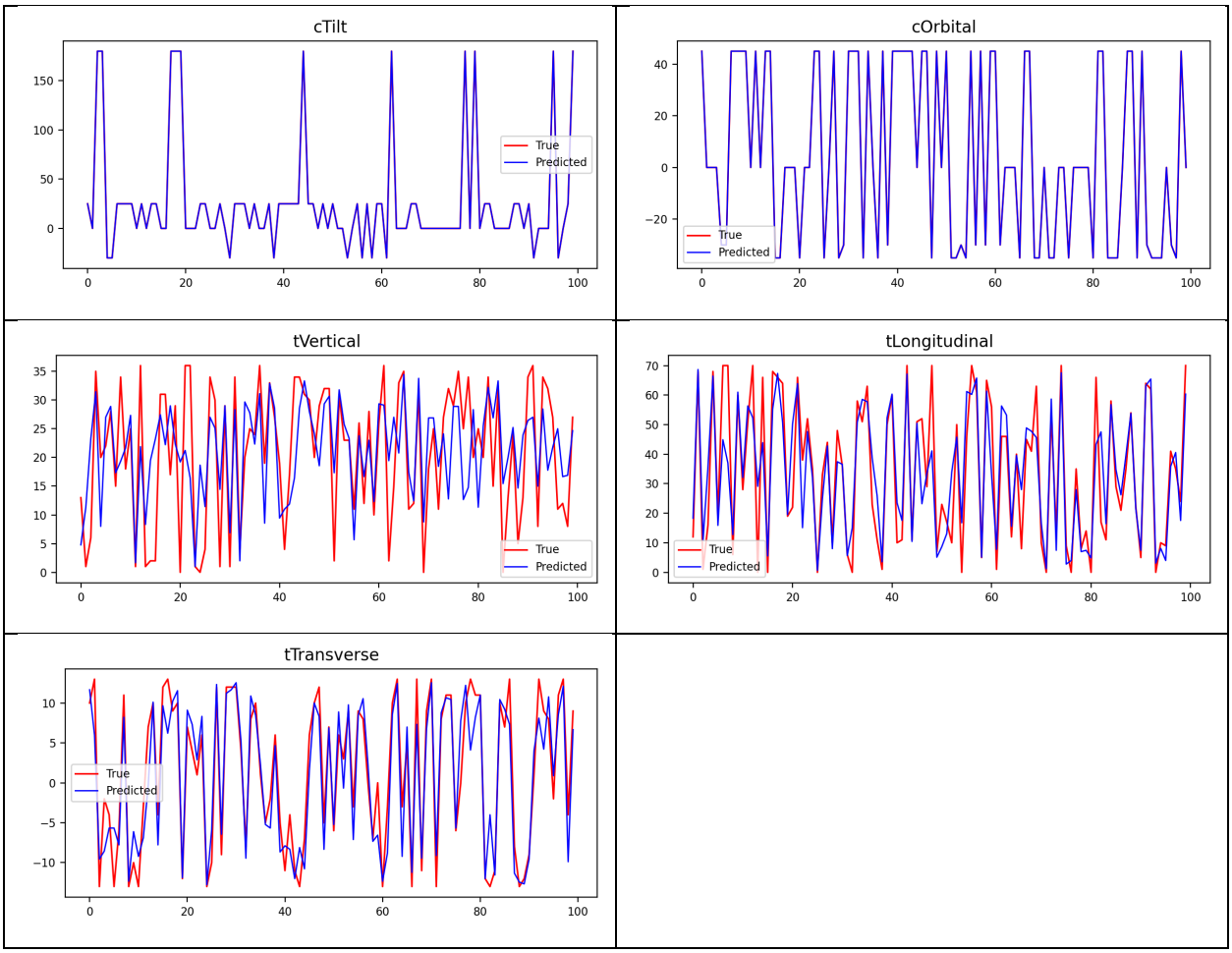

Figure 5.3: Prediction on the test set using K-Nearest Neighbors.

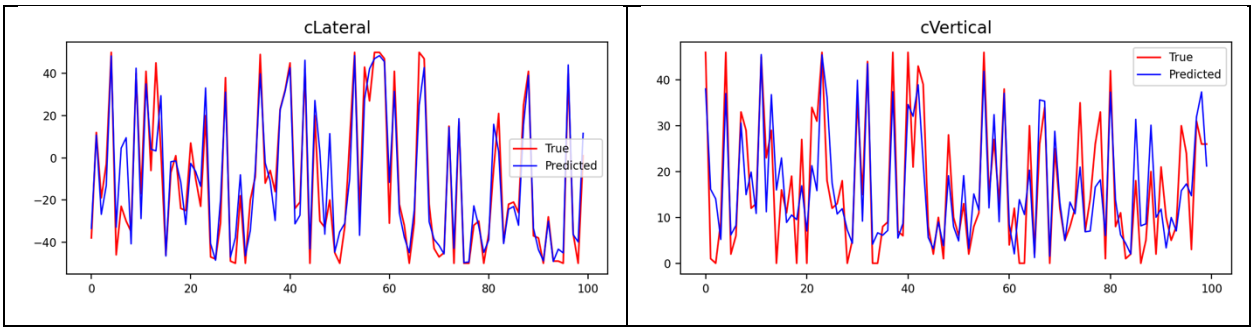

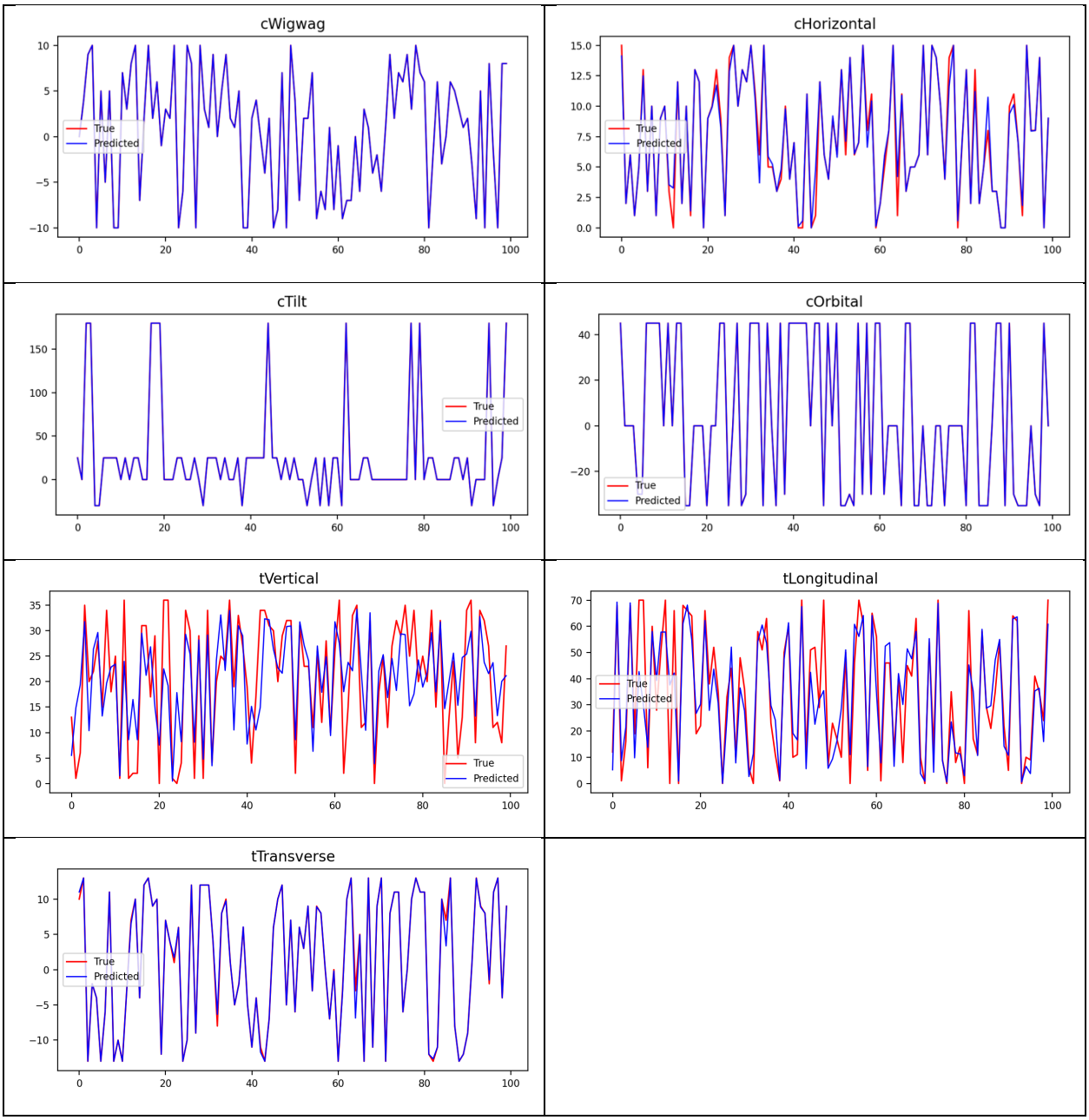

Figure 5.4: Prediction on the test set using Random Forest.

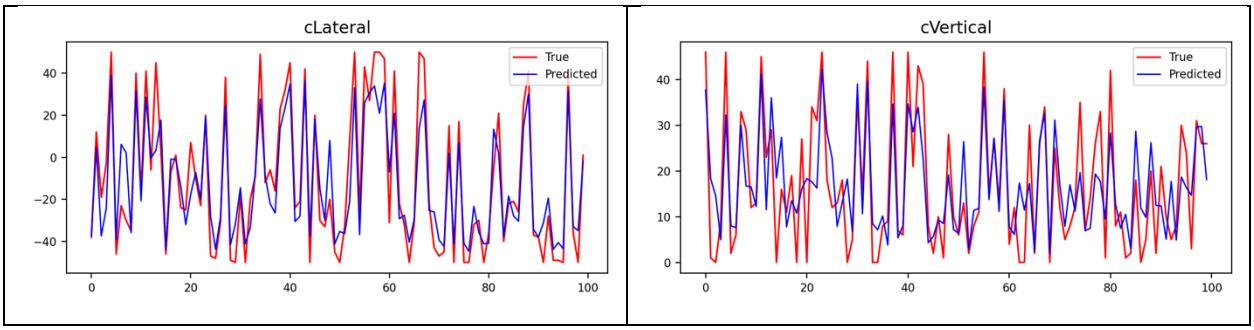

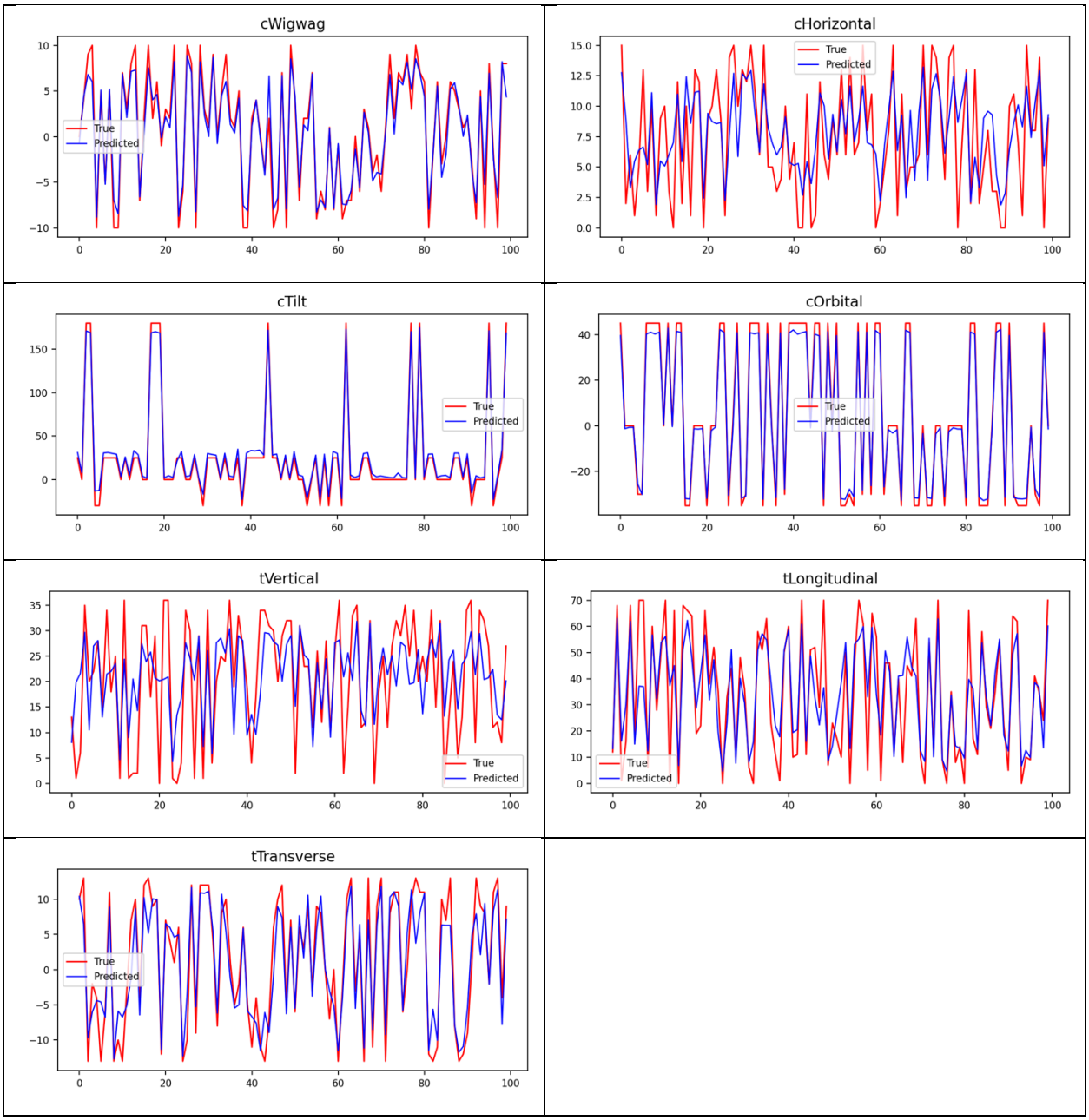

Figure 5.5: Prediction on the test set using Deep Neural Network (128–64-32).

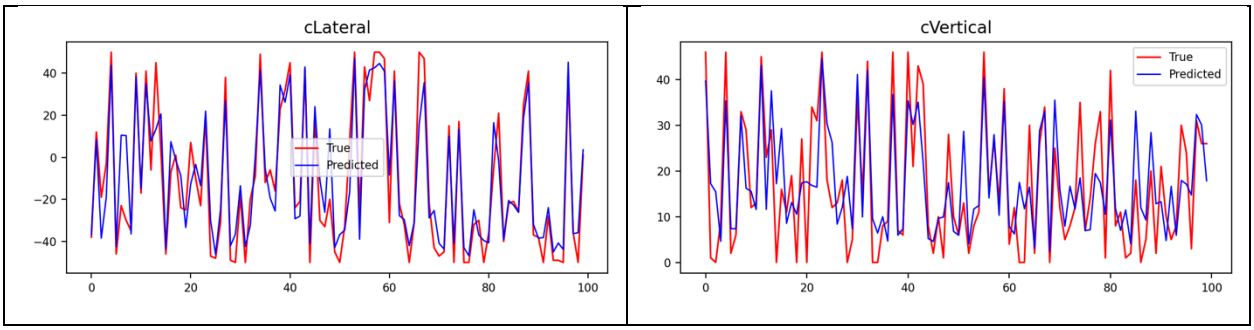

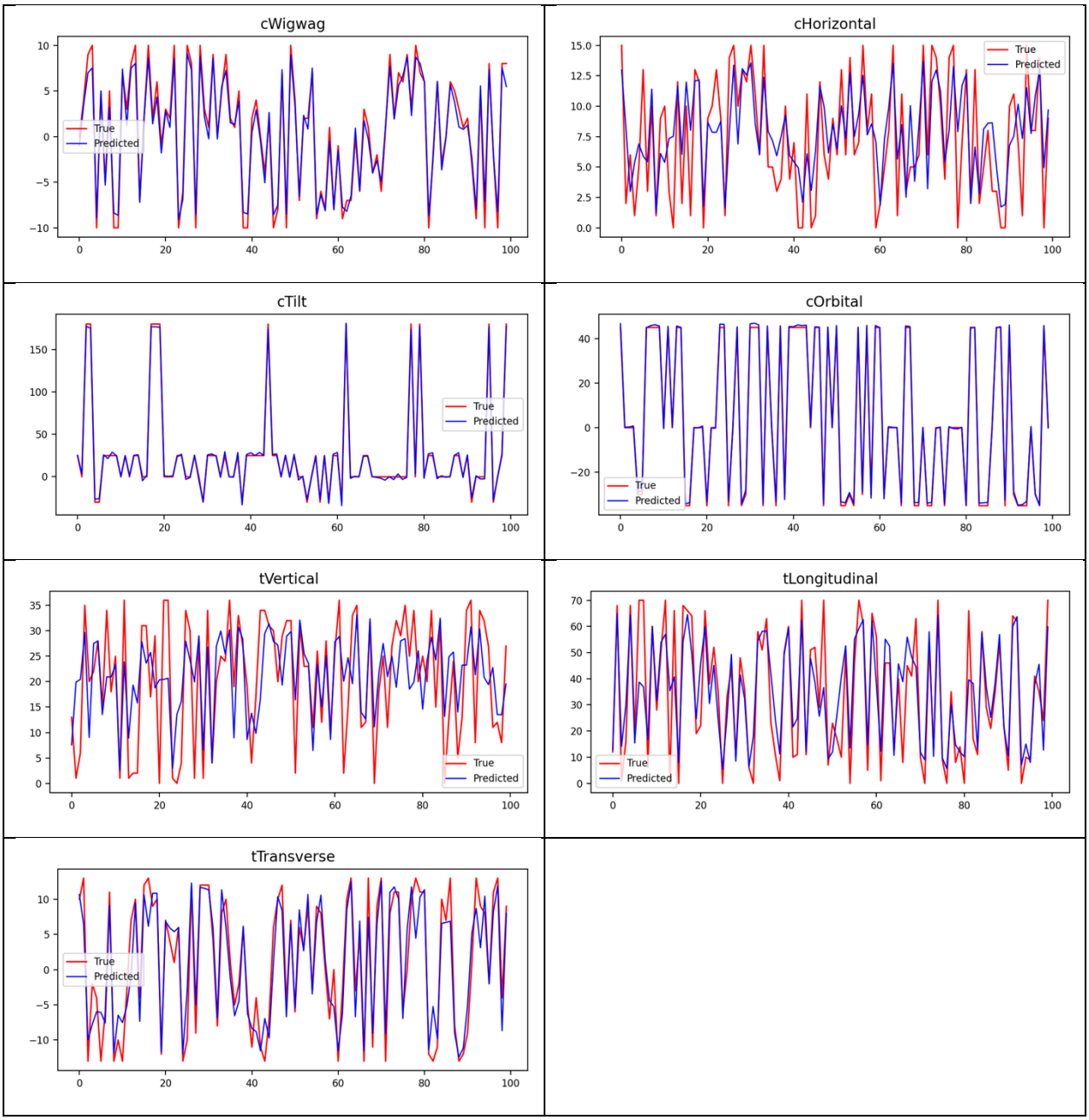

Figure 5.6: Prediction on the test set using Deep Neural Network with no PCA (256–128–64).

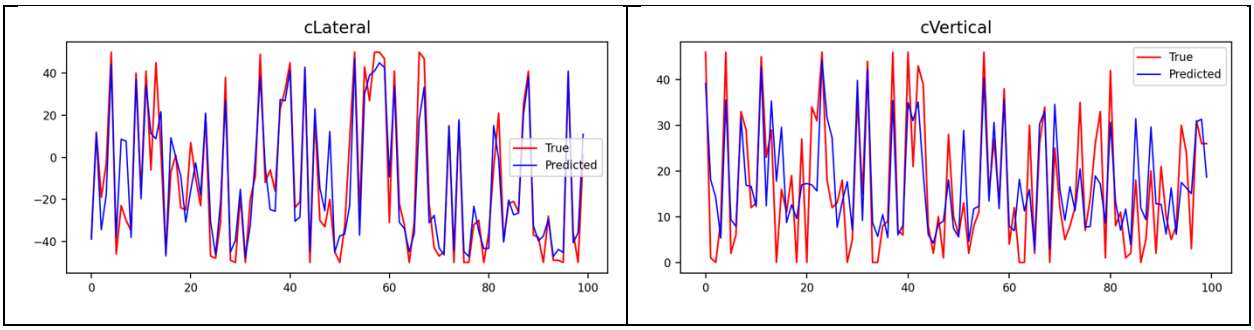

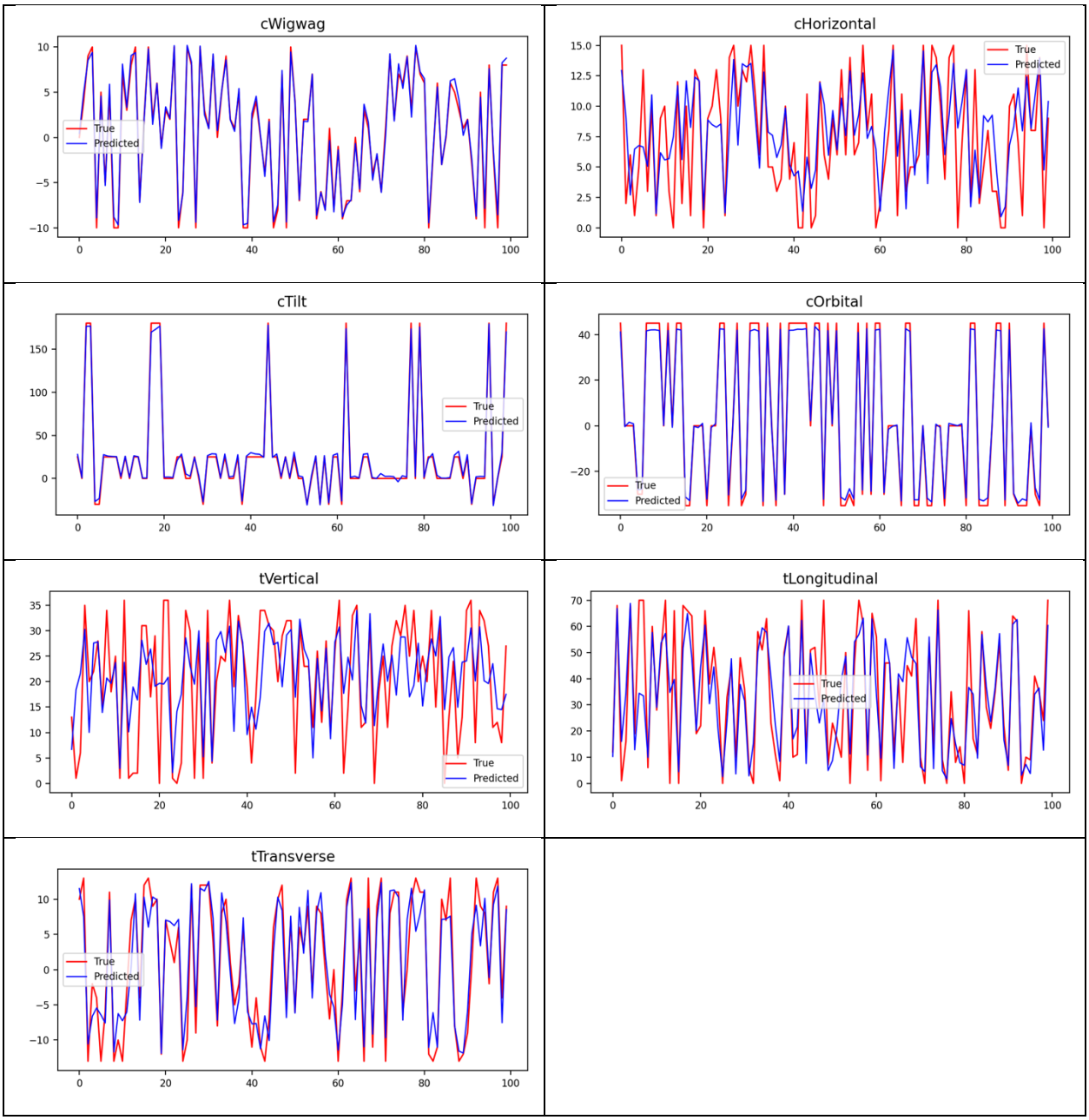

Figure 5.7: Prediction on the test set using Deep Neural Network (256–128–64) with PCA.

Appendix 4

The full set of machine learning results encompassing both forward and inverse kinematics across 5–9 DoF configurations is provided in the accompanying GitHub repository. Readers are encouraged to access the repository.